Lukas Johann Görtschacher, Dipl.-Ing., BSc

Novel UHF RFID Tracking and Sensing Systems

DOCTORAL THESIS

to achieve the university degree of

Doktor der technischen Wissenschaften

submitted to

Graz University of Technology

Supervisor

Univ.-Prof. Dipl.-Ing. Dr.techn. Wolfgang Bösch, MBA

Ass.-Prof Dipl.-Ing. Dr.techn. Jasmin Grosinger, BSc.

Institute of Microwave and Photonic Engineering

Evaluator

Prof. Alessandra Costanzo
University of Bologna

Graz, January 2019

AFFIDAVIT

I declare that I have authored this thesis independently, that I have not used other than the declared sources/resources, and that I have explicitly indicated all material which has been quoted either literally or by content from the sources used. The text document uploaded to TUGRAZonline is identical to the present doctoral thesis.

Date	Signature

Acknowledgments

This thesis has been conducted at the Institute of Microwave and Photonic Engineering at the Graz University of Technology. The work has been performed as part of the K-projects "Secure contactless sphere" and "Dependable, secure and time-aware sensor networks" that were funded by the Austrian Research Promotion Agency (FFG).

I would like to thank everyone who helped me to successfully write my dissertation. First of all, I am deeply grateful to my supervisor Professor Wolfgang Bösch for his guidance and support over the past four years. I would like to express my gratitude to Professor Alessandra Costanzo for reviewing my thesis and serving as examiner in my PhD thesis defense. Very special thanks to my co-supervisor Professor Jasmin Grosinger for the great guidance and support throughout my PhD studies and the excellent teamwork in the research projects. Moreover, I would like to thank my current and former colleagues from the RFID Technologies group for the friendly cooperation and the fruitful discussions. Especially, I would like to thank Bernhard Auinger, Hasan Noor Khan, Christof Glanzer and Lukas Zöscher. I would also like to thank my colleagues from the Institute of Microwave and Photonic Engineering who supported me in technical and administrative issues.

I would like to thank my friends who accompanied me throughout my studies and my girlfriend Elisabeth for the support. Special thanks to my longtime roommate Mario for the uncomplicated and great time. A heartfelt thanks also to Christoph and the "Graf-WG" for the warm welcome.

Finally, I owe my deepest gratitude to my parents for the ever-present love and support.

Abstract

This thesis presents two novel systems that are based on the ultra high frequency (UHF) radio frequency identification (RFID) technology. The introduced systems are, on the one hand, a robust and fast two dimensional tracking system and on the other hand, a stable, distance independent sensing system. The ultimate vision is the combination of both independent systems to a system that allows the tracking of low-cost UHF RFID based sensors with the novel features of both systems. Tracking of infusion bags in hospital rooms, while sensing the filling level of them, could be an application of the system. Such application environments suffer from multipath propagation, which impairs the power transfer to the sensors and distorts the detected sensor signals.
The thesis initially presents a rapid prototyping reader platform (RPRP) that has been developed in order to enable the rapid prototyping and testing of UHF RFID tracking and sensing systems. A high flexibility of the RPRP is introduced by the use of a software defined radio (SDR) as the basis unit. The performance requirements of the RPRP are deduced from channel measurements in a harsh multipath propagation environment, acting as a worst case scenario.
The tracking system is based on phase difference of arrival (PDoA) techniques in combination with a specific reader antenna arrangement. The robust position updates of the tracking system are achieved by minimizing the influence of errors introduced by multipath propagation. The tracking system is fast due to the fact that only one reader/tag communication cycle is needed for a position update, which is furthermore calculated analytically. Finally, the tracking system allows the tracking of UHF RFID tags on arbitrary two dimensional (2D) tracks, when knowing the starting position. These mentioned properties make the tracking system novel compared to related work.
The sensing system is based on a UHF RFID sensor transponder (tag) antenna that gives in combination with an off-the-shelf chip a low cost sensor. A stable

communication between the reader and the sensor is achieved by a purposeful consideration of UHF RFID tag performance parameters. The sensor tag antenna concept is furthermore based on the detection of defined tag signal patterns at the UHF RFID reader, which makes the sensing independent from the reader to tag distance. A stable and distance independent sensing system, using sensors that consist of a single sensor antenna and a single off-the-shelf chip, is novel compared to related work.

Contents

1 Introduction

The concept of backscatter communication has been proposed in 1948 as an extension to the already well-known radar technology [1]. Nowadays, this concept of backscatter communication is successfully applied and widely used in backscatter radio frequency identification (RFID) systems. While backscatter RFID systems are operated in ultra high frequency (UHF) and microwave bands, inductively coupled RFID systems are operated in the low frequency (LF) and high frequency (HF) bands [2].
In recent years, the potential for using backscatter RFID beyond the pure identification purpose has been recognized and extensively studied. In particular, passive backscatter RFID has been identified as an interesting technology for the realization of low-cost and low-maintenance localization and sensing applications (see Sec. 1.3). In passive backscatter RFID systems, batteryless or rather passive transponders (tags) communicate with a reader that acts as the control unit [3]. The power for the tag operation is drawn from the electromagnetic field radiated by the reader and the tag response is realized by a modulation of the backscattered signal. Beyond the digital tag identification number (ID), the amplitude and the phase of the backscattered tag signal may imply information about the location and/or the sensing state of the tag.
This thesis solves several problems that arise from using the narrowband backscatter UHF RFID technology for tracking and sensing in typical application environments. Typical application environments suffer from multipath propagation, which deteriorates the power supply of the passive tags and distorts the received tag signals. These effects cause outages in the communication and inaccuracies with respect to tracking and sensing. The main contributions of this thesis are a robust and fast two dimensional (2D) tracking system and a stable and distance independent sensing system.

1.1 UHF RFID System

A UHF RFID system consists of a reader and a tag that communicate via a wireless channel. The reader transmits data and power to the tag in the forward link, while a tag response is transmitted to the reader in the backward link. The tag does not have an own transmitter, but rather transmits its information by using modulated backscatter signals [3]. In the following, the reader, the communication channel and the tag are discussed in detail. These explanations consider the classical application of a UHF RFID system, which is the identification of objects. This basis knowledge is important for the explanation of the tracking and sensing system in later chapters.

1.1.1 Reader

A UHF RFID reader is a radio transceiver that operates in full-duplex mode [3]. The reader continuously generates a radio frequency (RF) signal at the operating frequency of the RFID system. The transmitted radio signal is either a command (modulated signal) or a continuous wave (CW) signal. During time periods, when the CW signal is transmitted, the reader listens for a potential tag response.
The reader can be set up with a monostatic or a bistatic antenna configuration, as depicted in Fig. 1.1. A monostatic reader uses a single antenna for signal transmission and reception (TX/RX antenna), in which the different signals are separated internally by, e.g., a circulator (see Fig. 1.1a). A bistatic reader uses different antennas for signal transmission (TX antenna) and reception (RX antenna) (see Fig. 1.1b) [4, 5].
The power of the received tag signal strongly depends on the distance between reader and tag and on the communication channel. Thus, the reader has to provide a high reader sensitivity T_{RX}, i.e., it should be able to detect very weak tag signals, and a high dynamic range, i.e., it should be able to detect a wide range (in terms of power) of signals [3].
Due to the nature of backscatter communication, the transmitted CW signal and the received tag signal appear at the same frequency. This means that while receiving the tag response, also the CW signal leaks into the receiver structure of the reader at the frequency of interest. The leaking CW signal

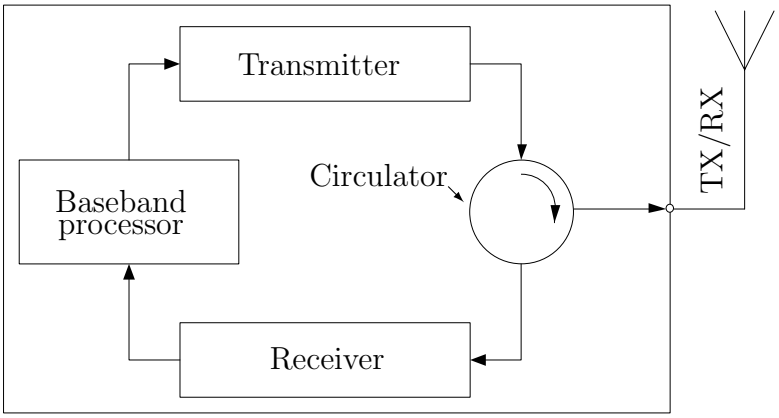

(a) Monostatic reader: A single antenna (TX/RX) is used for signal transmission and reception. The signals are separated by a circulator.

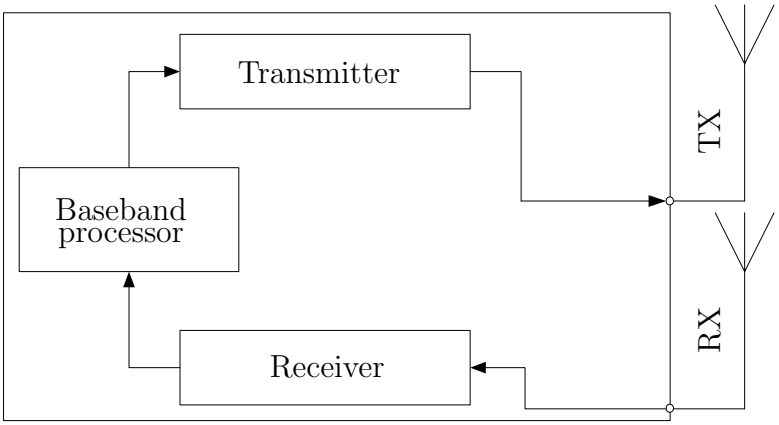

(b) Bistatic reader: Two separated antennas (TX, RX) are used for signal transmission and reception, respectively.

Figure 1.1: UHF RFID reader architectures: The transmitter modulates the RF carrier with the baseband signal and amplifies the generated RF signal. The receiver amplifies the received RF signal and demodulates it to a baseband signal. The baseband processor generates the commands for transmission and interprets the received tag signal [4, 5]. An LO provides a signal with constant amplitude and phase for frequency mixing in the modulation and demodulation process. A LNA amplifies the received signal for further processing [3].

power depends on several factors, but is typically very high in comparison to the received tag signal. For example, the leakage signal may be 65 dB larger in case of a monostatic reader and 40 dB larger in case of a bistatic reader, in which the isolation is typically higher [3]. Also, reflections of the CW signal from static objects in the environment of the reader and modulation independent reflections from the tag antenna contribute to the received leakage signal [5]. It can be recognized that a backscatter RFID reader has to deal with very strong signals, which can saturate the receiver structure and impair the sensitivity of the reader. Also the leaked phase noise of the local oscillator (LO) impairs the reader sensitivity. The performance of the reader receiver can be improved by canceling the leakage before it reaches the low noise amplifier (LNA) of the receiver structure. This can be done by adapting a small portion of the transmitted signal and subtract it from the received signal, leading in the optimum case to the sole tag signal at the LNA [5].

Baseband Signal Constellation

Figure 1.2 shows an exemplary baseband signal constellation at the reader without a perfect leakage cancellation [4]. The Inphase (I) and Quadrature (Q) diagram shows two voltage states $S^{(A)}$ and $S^{(B)}$. When the tag is in it absorbing state, only the leakage signal L is present and the state $S^{(A)}$ is detected. State $S^{(B)}$ is detected at the reader when the tag is in it reflecting state. The tag signal h can be extracted by subtracting $S^{(A)}$ from $S^{(B)}$, $h = S^{(B)} - S^{(A)}$, which is actually a leakage cancellation in the baseband. The tag signal can be expressed by an amplitude and phase: $h = |h|_{\underline{\angle \varphi_h}}$.

1.1.2 Communication Channel

The communication channel in UHF RFID systems can be divided into a forward link and a backward link, describing the reader-tag and tag-reader links, respectively. Within the forward link, data and power for chip operation is transmitted to the tag. The power available for chip operation, P_{chip}, is modeled by [6]

$$P_{\text{chip}} = P_{\text{TX}} G_{\text{TX}} L_{\text{fw}} p_{\text{fw}} G_{\text{Tag}} \tau, \tag{1.1}$$

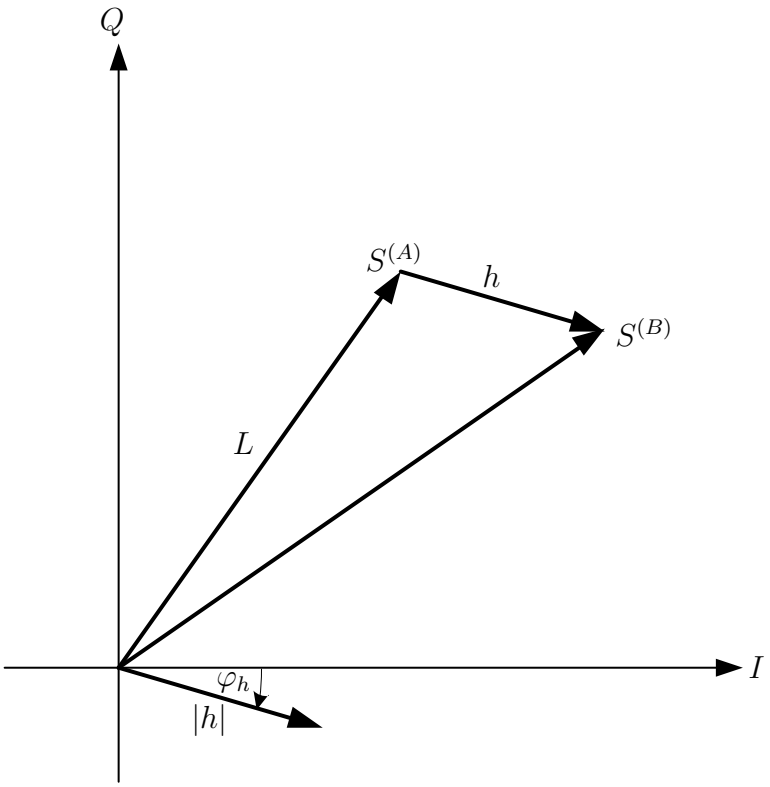

Figure 1.2: Baseband signal constellation: I versus Q component of the received baseband signal. Voltage state $S^{(A)}$ is detected when the tag is in the absorbing mode, while $S^{(B)}$ is detected when the tag is in the reflecting state. The baseband tag signal is defined by $h = S^{(B)} - S^{(A)}$ and can be presented by $h = |h|\underline{/\varphi_h}$ [4].

where P_{TX} and G_{TX} are the reader transmit power and TX antenna gain, respectively. L_{fw} describes the path loss between the reader TX and tag antenna and is determined by the line-of-sight link and/or several single reflections. Besides the tag antenna gain G_{Tag}, also the polarization mismatch p_{fw} between the reader TX and tag antenna influences P_{chip} and can vary between 0 and 1 [7]. The power transmission coefficient τ considers the influence of the matching between tag antenna and tag chip and will be explained in more detail in Sec. 1.1.3. The power available at the tag antenna terminals, P_{Tag}, can then be calculated as

$$P_{\mathrm{Tag}} = \frac{P_{\mathrm{chip}}}{\tau}. \tag{1.2}$$

The communication channel is forward link limited, if P_{chip} is smaller than the chip sensitivity T_{chip}, which is the minimum power necessary for chip operation [8].
Within the backward link, the modulated backscattered signal is transmitted to the reader. The power of the received tag signal, P_{RX}, is modeled by [6]

$$P_{\mathrm{RX}} = P_{\mathrm{Tag}}\eta G_{\mathrm{Tag}} L_{\mathrm{bw}} p_{\mathrm{bw}} G_{\mathrm{RX}}. \tag{1.3}$$

First, the available power at the tag antenna terminals, P_{Tag}, gets scaled by the tag modulation efficiency η, which is explained in more detail in Sec. 1.1.3. Then, similar to the forward channel, the remaining power is scaled by tag and reader RX antenna gains G_{Tag} and G_{RX}, the path loss of the backward link L_{bw} and the polarization mismatch p_{bw} between the tag and reader RX antenna. The communication channel is backward link limited, if P_{RX} is smaller than the reader sensitivity T_{RX}, which is the minimum tag signal power that can be detected at the reader [8].
The link budget of a UHF RFID system can also be presented by means of channel transfer functions as presented by [4]. There, antenna and propagation related characteristics like gain, polarization and path loss are incorporated within the channel transfer functions h_{fw} and h_{bw} for the forward link and backward link, respectively. With this, the power available for chip operation is defined by

$$P_{\mathrm{chip}} = P_{\mathrm{TX}}|h_{\mathrm{fw}}|^2\tau = P_{\mathrm{Tag}}\tau, \tag{1.4}$$

and the power of the received tag signal is defined by

$$P_{\mathrm{RX}} = P_{\mathrm{TX}}|h_{\mathrm{fw}}|^2\eta|h_{\mathrm{bw}}|^2 = P_{\mathrm{Tag}}\eta|h_{\mathrm{bw}}|^2. \tag{1.5}$$

These channel transfer functions h_{fw} and h_{bw} can be measured by measuring the transmission coefficients S_{21} and S_{12} with a vector network analyzer (VNA) for the forward link and backward link, respectively [9]. For this, the VNA has to be connected to the respective antenna inputs. $|h_{\mathrm{fw}}|^2$ and $|h_{\mathrm{bw}}|^2$ are defined as the channel gain of the forward link G_{fw} and the channel gain of the backward link G_{bw}, respectively.

1.1.3 Transponder

A passive UHF RFID tag is powered by the RF field of the reader and does not have an own transmitter. Thus, it is typically emphasized to reach a high power transfer to the tag chip to ensure a reliable operation. The tag behavior can be modeled by an equivalent circuit shown in Fig. 1.3, in which the antenna is represented by an open circuit voltage V_{oc} and the complex impedance Z_{Ant} [10, 4]. The tag modulates the backscatterd signal by switching between an absorbing mode and a reflecting mode, i.e., by switching between the absorbing impedance Z_{Abs} and the reflecting impedance Z_{Ref}. Depending

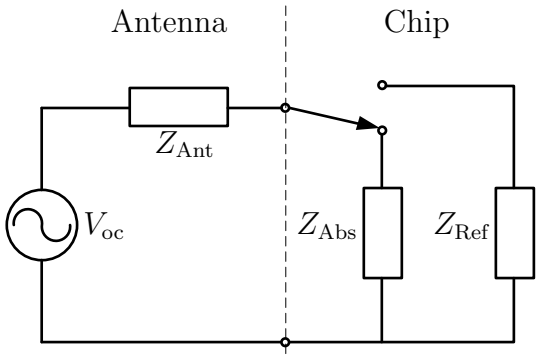

Figure 1.3: Tag equivalent circuit: The tag antenna is modeled by an open circuit voltage V_{oc} and a complex antenna impedance Z_{Ant}. The backscattered tag signal is modulated by switching between two chip impedances, the absorbing impedance Z_{Abs} and the reflecting impedance Z_{Ref}.

on the mode, two different reflection coefficients can be defined that determine the amplitude and phase of the reflected CW signal at the chip input [11]. The reflection coefficient in absorbing mode S_{Abs} and in reflecting mode S_{Ref} are

defined as

$$S_{\mathrm{Abs}} = \frac{Z_{\mathrm{Abs}} - Z_{\mathrm{Ant}}^*}{Z_{\mathrm{Abs}} + Z_{\mathrm{Ant}}} \text{ and} \tag{1.6}$$

$$S_{\mathrm{Ref}} = \frac{Z_{\mathrm{Ref}} - Z_{\mathrm{Ant}}^*}{Z_{\mathrm{Ref}} + Z_{\mathrm{Ant}}}, \tag{1.7}$$

where Z_{Ant}^* is the complex conjugate of Z_{Ant}. The power that is available at the chip input for chip operation is determined by the power transmission coefficient [4]

$$\tau = 1 - |S_{\mathrm{Abs}}|^2. \tag{1.8}$$

The maximum power for chip operation in the absorbing mode is available, if $\tau = 1$ and thus no power is reflected at the chip input. This is reached in case the antenna impedance is matched to the chip impedance, i.e., $Z_{\mathrm{Ant}} = Z_{\mathrm{Abs}}^*$ and thus $S_{\mathrm{Abs}} = 0$. In the reflecting state, typically all the power is reflected at the chip input, meaning that $|S_{\mathrm{Ref}}| = 1$ and $\tau = 0$. These mentioned conditions, where $S_{\mathrm{Abs}} = 0$ in the absorbing mode and $|S_{\mathrm{Ref}}| = 1$ in the reflecting mode, define an ideally amplitude modulated backscattered signal. Figure 1.4 shows a tag response diagram of an ideally amplitude modulated backscattered signal with the corresponding reflection coefficients $S_{\mathrm{Abs,am}}$ and S_{Ref}.
The modulation efficiency η is a measure of how much CW power, which is available at the tag antenna terminals, can be converted to the sideband power of the modulated backscattered signal. The modulated backscattered signal is a result of the two backscattered CW signals in the corresponding modes, i.e., absorbing mode and reflecting mode. As the modulation frequency is much lower than the operating frequency, the modulation signal can be approximated by a rectangular function [11]. The modulation efficiency η is defined as [6]

$$\eta = \alpha |S_{\mathrm{Abs}} - S_{\mathrm{Ref}}|^2, \tag{1.9}$$

where α depends on the modulation details. α accounts for the information relevant, time averaged, and direct current (DC) removed power of the signal, i.e., the power of the modulation signal $h'(t)$[1], as exemplarily depicted in Fig. 1.5. The value of α is ideally $\frac{1}{4}$ in case of a modulation with 50 % duty cycle, i.e.,

[1]The modulation signal $h'(t)$ becomes the baseband tag signal $h(t)$ that is detected at the reader receiver, due to the influence of the backward link.

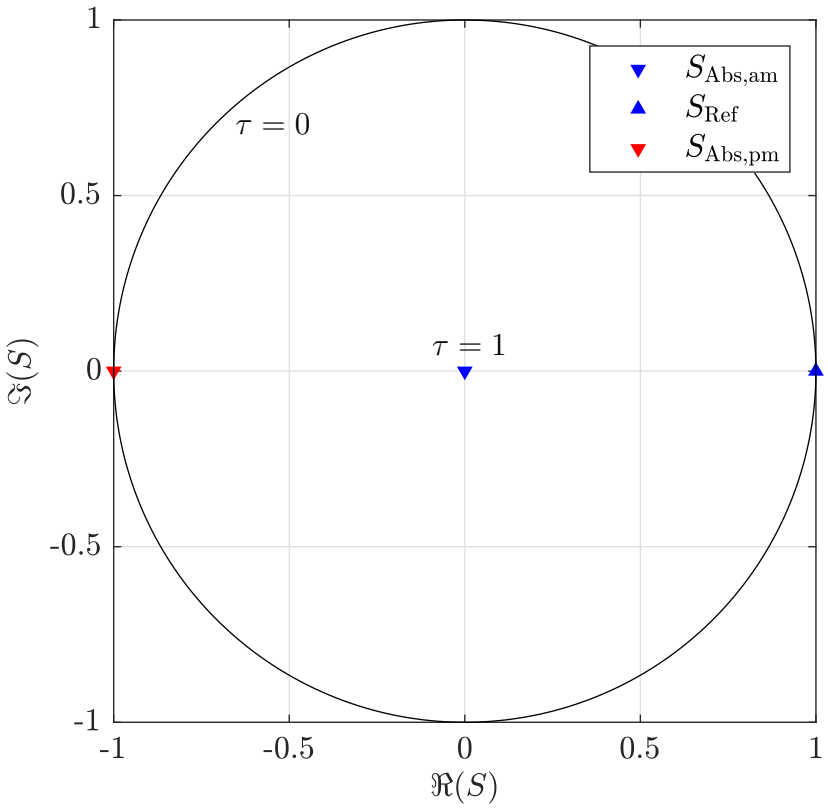

Figure 1.4: Ideal tag response diagram: An ideal amplitude modulated tag response is defined by $S_{\mathrm{Abs,am}} = 0$ and $|S_{\mathrm{Ref}}| = 1$, leading to a power transmission coefficient of $\tau = 1$. An ideal phase modulated tag response is defined by $|S_{\mathrm{Abs,pm}}| = |S_{\mathrm{Ref}}| = 1$ with contrary phases, leading to a maximization of the modulation efficiency of $\eta = 1$.

the tag is 50 % of the time in absorbing and reflecting mode, respectively [6]. Descriptively spoken, the time averaged power of the information relevant rectangular modulation signal is $\frac{1}{4}$ of the power of a DC signal (see Fig. 1.5) with the same peak to peak amplitude. In literature, also $\alpha = \frac{2}{\pi^2}$ is used, which is a value that considers only the power in the first sinusoidal oscillation ($h'_{1st}(t)$ in Fig. 1.5) of the rectangular modulation function [11]. The exact value for α might be between $\frac{2}{\pi^2}$ and $\frac{1}{4}$, but the latter definition is used in this thesis. η reaches its maximum of 1 in case of an ideally phase modulated backscattered signal, where S_{Abs} and S_{Ref} both have a magnitude of 1 and contrary phases, e.g. $\eta = \frac{1}{4}|1 - (-1)|^2 = 1$. Exemplary reflections coefficients $S_{\mathrm{Abs,pm}}$ and S_{Ref} of an ideally phase modulated backscattered signal are shown in Fig. 1.4. In case of an ideally amplitude modulated backscattered signal the modulation efficiency is $\eta = \frac{1}{4}$.

Lets assume a tag antenna that is matched by its complex conjugated impedance Z^*_{Abs} and an impinging field that causes a voltage with a power of P_{Tag} at the tag antenna terminals. Lets now replace the complex conjugated load by the chip with its two impedances and furthermore change the mode to a 50 % duty cycle. Now, the rectangular modulation function would have a power of ηP_{Tag}, or $\frac{1}{4}P_{\mathrm{Tag}}$, in case of an ideally amplitude modulated signal.

The complex expression $S_{\mathrm{Abs}} - S_{\mathrm{Ref}}$ does not only influence the power or magnitude of the modulated backscattered signal, as indicated by Eqn. 1.9, but also determines the phase of the signal [11]. If the phase $\varphi_{S_{\mathrm{Abs}}-S_{\mathrm{Ref}}}$ changes by $\Delta\varphi_{S_{\mathrm{Abs}}-S_{\mathrm{Ref}}}$, then also the phase of the modulated backscattered signal changes by $\Delta\varphi_{S_{\mathrm{Abs}}-S_{\mathrm{Ref}}}$. The modulated backscattered signal experiences additional changes in magnitude and phase when being received at the reader due to the communication channel and appears as the tag signal, e.g., depicted in Fig. 1.2.

1.1.4 Magnitude and Phase Relations

Despite the power considerations in a backscatter UHF RFID system, also the amplitude and phase relations are essential for the work presented in this thesis. In the following, the received baseband tag signal h will be derived from a complex valued RF tag signal in the frequency domain with a magnitude $|h|$

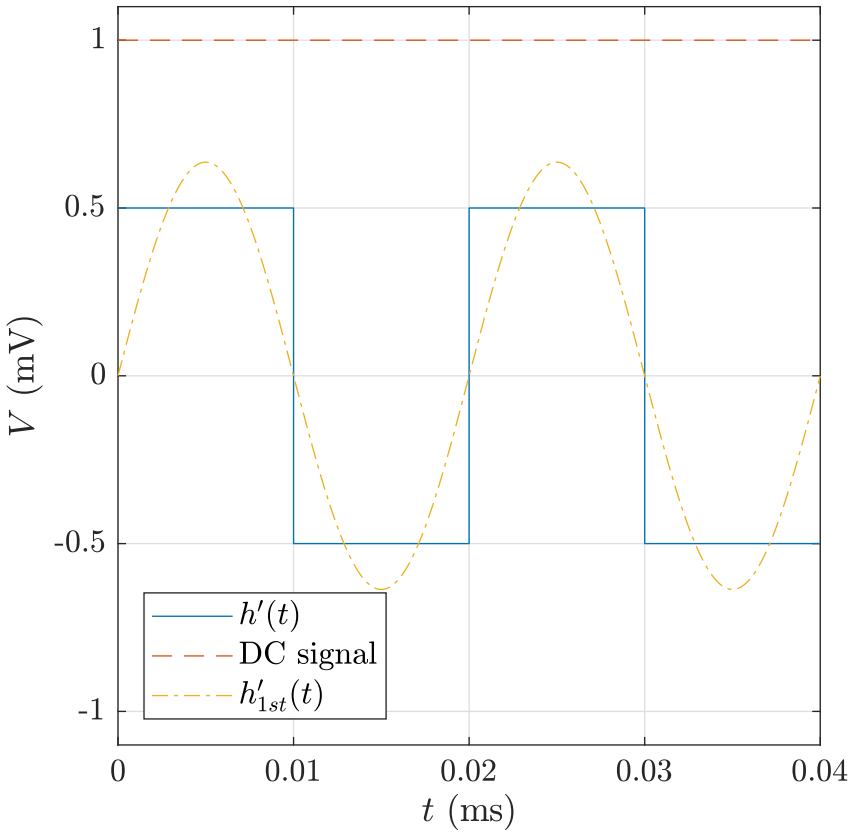

Figure 1.5: Visualization of coefficient α of modulation efficiency η: α accounts for the information relevant, time averaged, and DC removed power of the signal, i.e., the power of the modulation signal $h'(t)$. The power of $h'(t)$ is $\frac{1}{4}$ ($\alpha = \frac{1}{4}$) the power of the DC signal, which contains no information. The power of the first sinusoidal oscillation $h'_{1st}(t)$ of $h'(t)$ is $\frac{2}{\pi^2}$ the power of the DC signal.

and a phase φ_h:

$$h_\mathrm{RF} = |h|e^{j\varphi_h}. \tag{1.10}$$

Let $s_\mathrm{TX} = |s_\mathrm{TX}|e^{j\varphi_{s_\mathrm{TX}}}$ be a sinusoidal signal that is fed to the reader TX antenna with a magnitude of $|s_\mathrm{TX}| = \sqrt{2P_\mathrm{TX}}$, leading to an RF signal power of P_TX, assuming for simplicity a 1 Ω system. The RF tag signal received at the reader receiver is now modeled as [12, 13],

$$h_\mathrm{RF} = s_\mathrm{TX}h_\mathrm{fw}\sqrt{|S_\mathrm{Abs} - S_\mathrm{Ref}|^2}e^{j\varphi(S_\mathrm{Abs}-S_\mathrm{Ref})}h_\mathrm{bw}, \tag{1.11}$$

where $h_\mathrm{fw} = |h_\mathrm{fw}|e^{j\varphi_{h_\mathrm{fw}}}$ and $h_\mathrm{bw} = |h_\mathrm{bw}|e^{j\varphi_{h_\mathrm{bw}}}$ are the channel transfer functions of the forward link and backward link, respectively. As previously mentioned, these channel transfer functions can for example be measured by a VNA. Magnitude and phase of the tag signal can now be represented separately by,

$$|h_\mathrm{RF}| = |h| = |s_\mathrm{TX}||h_\mathrm{fw}||S_\mathrm{Abs} - S_\mathrm{Ref}||h_\mathrm{bw}|, \tag{1.12}$$

$$\varphi_{h_\mathrm{RF}} = \varphi_h = \varphi_{h_\mathrm{fw}} + \varphi_{(S_\mathrm{Abs}-S_\mathrm{Ref})} + \varphi_{h_\mathrm{bw}}. \tag{1.13}$$

It can be seen, that both, the magnitude and the phase of the tag signal depend on the complex difference between the reflection coefficients in absorbing mode and reflecting mode, $S_\mathrm{Abs} - S_\mathrm{Ref}$. Note that this representation of h_RF does not take any modulation into account, but can be interpreted as a CW signal at the reader receiver with an RF signal power of $\frac{|h|^2}{2}$. A direct conversion of this CW signal to the baseband leads to a DC voltage with a magnitude of $|h|$. However, assuming again a modulation duty cycle of 50 %, the DC voltage is zero during half of the time. A change of the voltage between $|h|$ and zero leads to a rectangular voltage function with a DC offset of $\frac{|h|}{2}$, where the DC component is typically ignored for power conciderations [6]. The remaining power of the rectangular function with a magnitude of $\frac{|h|}{2}$ is four times smaller than the power of the DC voltage with magnitude $|h|$, which is conform with a value of $\alpha = \frac{1}{4}$.
The power of the received tag signal P_RX can now be calculated as

$$P_\mathrm{RX} = \alpha|h|^2 = P_\mathrm{TX}|h_\mathrm{fw}|^2\alpha|S_\mathrm{Abs} - S_\mathrm{Ref}|^2|h_\mathrm{bw}|^2 = P_\mathrm{TX}|h_\mathrm{fw}|^2\eta|h_\mathrm{bw}|^2, \tag{1.14}$$

which is conform to the definition presented in Eqn. 1.5.
As shown by the baseband constellation of the tag signal in Fig. 1.2, magnitude

and phase can also be written by the subtraction of the states at the reader,

$$|h| = |S^{(B)} - S^{(A)}|, \tag{1.15}$$

$$\varphi_h = \varphi_{(S^{(B)} - S^{(A)})}. \tag{1.16}$$

1.2 Scope of Work

This thesis presents and examines a novel tracking system and a novel sensing system using the UHF RFID technology. These novel systems have been developed in order to mitigate limitations that arise from using this technology in typical application environments. Main limitations of the backscatter RFID technology are the limited frequency bandwidth and the limited available power in the communication channel that makes localization and sensing a big challenge.
A rapid prototyping platform has been developed at the beginning of the research in order to allow a fast prototyping and testing of tracking and sensing systems.
One main contribution is a novel 2D tracking system that works robustly in multipath propagation environments and provides fast position updates. The tracking system has been developed as a consequence of the poor performance of an initially developed 2D localization system in multipath propagation environments. A localization system provides absolute positions, while in contrast, a tracking system provides position updates.
The second main contribution is a novel sensing system that ensures a stable communication between the reader and the tag within the entire sensing range and furthermore a distance independent sensing. A possible application could be the tracking of sensor tags that sense the filling level of infusion bags in hospital rooms.

1.3 Related Work

A comparison to related work, including a brief summary of the main contributions of this thesis, is presented in the following.

1.3.1 Tracking System

Many different narrowband approaches for indoor tracking and localization by means of the UHF RFID technology are investigated in literature. In received signal strength indicator (RSSI) based approaches, the power of the received

tag signal is related to the distance between the reader and the tag [14, 15, 16, 17, 18, 19, 20]. Nowadays, these approaches are mainly combined with different kind of other approaches. These approaches include, e.g., the use reference tags [21, 22, 16, 23, 20] or the exploitation of the tag signal phase [20, 18, 16].
The tag signal phase based approaches can be divided into phase of arrival (PoA) and phase difference of arrival (PDoA) techniques. PoA as, e.g., used in [24, 25, 18] relies on the recording and computation of tag signal phases, while PDoA relies on the recording and computation of tag signal phase differences. Furthermore, the PDoA approaches can be split into spatial domain phase difference of arrival (SD-PDoA), frequency domain phase difference of arrival (FD-PDoA) and time domain phase difference of arrival (TD-PDoA), which are summarized in, e.g., [26]. SD-PDoA relates the phase difference of the tag signal received at more antennas at the same time to location parameters like the direction of arrival (DoA) as, e.g., presented in [27]. FD-PDoA relates the phase difference of the tag signal received at different frequencies to the distance between the reader and the tag as, e.g., presented in [28]. TD-PDoA relates the phase difference of the tag signal received at different time instances to, e.g., the velocity of the tag [26]. Furthermore, the TD-PDoA approach is used in synthetic aperture radar (SAR) [29] and inverse synthetic aperture radar (ISAR) [30, 31] systems.
Chapter 3 presents the novel 2D tracking system by means of passive backscatter UHF RFID tags. The system is based on the PDoA technique and on a specific bistatic reader antenna arrangement. The system is very robust to multipath propagation and can thus be used in real application environments. Furthermore, all required tag signal phase information for a position update is captured within one communication cycle and the current tag position is calculated analytically. These facts guarantee a very efficient and fast tracking of the tags. Finally, the position update is not restricted to be on a known path. The collectivity of the mentioned features is novel compared to related work.

1.3.2 Sensor System

Sensing based on the passive UHF RFID technology might be divided into two main categories, sensor tags with a dedicated sensing circuitry and sensor tags without a dedicated sensing circuitry. The latter provides less features (memory, processing ability, etc.) but can be used in a ubiquitous way and is cheaper to

implement [32]. The sensing capability can, e.g., be introduced by a modulation of the chip reflecting impedance as presented in [4]. A more common alternative in the literature is to incorporate the sensing ability in the antenna (sensor antenna) of the sensor tag, i.e., the antenna acts as a transducer. Sensor tags using sensor antennas have been prototyped for several sensing applications like filling level sensing [32, 33, 34], temperature sensing [35, 32, 34, 36, 37], humidity sensing [38, 39, 40, 41, 34], displacement and orientation sensing [32, 34, 42, 43, 44], strain and crack sensing [45, 34], gas sensing [46, 47], corrosion sensing [48], haptic sensing [49] and pH-value sensing [50].
Most of the mentioned applications relate their sensing information to the power within UHF RFID sensing systems. The sensing information is either extracted by measuring the transmitted power necessary to wake up the tag or by measuring the change of the backscattered tag signal power for a constant transmitted power [32]. By doing so, these approaches decrease the read range of the sensor tags for certain sensing states. Relating the sensing information to the phase of the backscattered tag signal can provide more control about the read range performance of the sensor tags [38, 33].
Another big challenge, if using UHF RFID sensor tags without a dedicated sensing circuitry, is the calibration. For example, the same sensor has to be calibrated for each reader to tag distance. One approach is presented in [51], where an analog identifier is used to provide distance independence in power (amplitude) related sensing systems. A distance independent approach for phase based sensing is presented in [52], in which closely coupled tags and reference tags are used. Another general approach for distance independent sensing is presented in [53], where a transfer impedance is introduced for the characterization of the channel. The transfer impedance is estimated by means of multiple (more than two) chip impedances, which requires custom-built chips.
Chapter 4 presents a novel system for a stable and distance independent sensing by means of passive backscatter UHF RFID tags. The sensing capability of the sensor tag is accomplished by using a sensor antenna. Thus, an off-the-shelf chip without any sensor interface can be used for the sensor tag. The system ensures a stable communication between the reader and the sensor tag within the entire sensing range. This is done by ensuring a high power transmission to the tag and a high backscattered tag signal power within the entire sensing range. The sensing system is based on a sensor antenna concept, presented for the first time, that allows the detection of defined tag signal patterns at the reader. The

detection of signal patterns makes the sensor system independent from the distance between the reader and the sensor tag and thus no system calibration is required. Stable and distance independent sensing by means of only a single sensor antenna combined with an off-the-shelf chip is novel compared to related work.

2 Rapid Prototyping Reader Platform

This chapter presents the rapid prototyping reader platform (RPRP) that has been developed in the early state of the thesis. The RPRP has been developed in order to allow a rapid prototyping of tracking and sensing systems to go towards the ultimate vision of a combined tracking and sensing system. The reader platform is assembled based on requirements that have been identified with respect to the prototyping of tracking and sensing systems. Based on the identified requirements in Sec. 2.1, the final setup of the RPRP is presented in Sec. 2.2.

Original Publications Related to this Chapter

L. Görtschacher, J. Grosinger, B. Auinger, D. Amschl, P. Priller, U. Muehlmann, and W. Bösch, "SIMO RFID System Performance in an Engine Test Bed." In: *Proc. IEEE International EURASIP Workshop on RFID Technology (EURFID)*, 2015.

L. Görtschacher, J. Grosinger, H.N. Khan, B. Auinger, D. Amschl, P. Priller, U. Muehlmann, and W. Bösch, "SIMO UHF RFID reader using sensor fusion for tag localization in a selected environment." In: *e & i Elektrotechnik und Informationstechnik*, 2016.

2.1 Requirements

The frequency range of the RPRP should cover at least the $865 - 868$ MHz band (ETSI[1]) for RFID in Europe and the $902 - 928$ MHz band (FCC[2]) for, e.g., the United States. A wider frequency range might be beneficial for future prototyping of systems operating in other frequency bands.
The maximum allowed UHF RFID signal transmit power in Europe is defined by a maximum effective radiated power (ERP) of 2 W (≈ 33.01 dBm) or an effective isotropic radiated power (EIRP) of 3.28 W (≈ 35.16 dBm) [3]. A maximum EIRP of 36 dBm is allowed in the United States. The maximum output power $P_{\mathrm{TX,max}}$ of a reader depends on the gain of the TX antenna and can be calculated by

$$P_{\mathrm{TX,max}} = \mathrm{EIRP} - G_{\mathrm{TX}}. \tag{2.1}$$

The output power of the RPRP should be adjustable within a meaningful range. At least, the maximum allowed EIRP should be reached for different antenna gains. A low as possible P_{TX} would be beneficial for measuring e.g., the minimum power to wake up a tag, as this figure of merit (FoM) can be related to the maximum communication distance between a reader and a tag [6].
The sensitivity T_{RX}, as well as the dynamic range of the RPRP should be as high as possible, in order to detect a wide range (in terms of power) of tag signals. The sensitivity in dBm of any receiver can be estimated by [9]

$$T_{\mathrm{RX}} = 10\log_{10}(kT_0 1000) + 10\log_{10}(BW) + NF + SNR, \tag{2.2}$$

where k is the Bolzmann constant, T_0 is the operating temperature in Kelvin, BW is the bandwidth and NF is the noise figure in dB of the receiver. The necessary signal to noise ratio (SNR) for a correct detection of received signals depends on the modulation scheme. FM0 modulation [54] is assumed for the considerations, which requires a minimum SNR of 10 dB [3]. The requirement on the reader sensitivity depends on the targeted application as well as on the system environment. The actual requirement on the sensitivity of the RPRP has been deduced from channel measurements in a harsh multipath

[1] European Telecommunications Standards Institute
[2] Federal Communications Commission

environment. Such environments allow the assessment of the behavior in worst case scenarios. The channel measurements and the required sensitivity of the RPRP are presented below.
Finally, the RPRP should be able to handle multiple input multiple output (MIMO) applications like DoA estimation as presented e.g., in [27]. The MIMO compatibility implies the prototyping of bistatic reader applications.

Channel Measurements

As mentioned above, channel measurements have been done in a room that represents a harsh multipath propagation environment by colleagues of the Institute of Microwave and Photonic Engineering (IHF). In this thesis, the measured S-parameters have been used to evaluate the possibility to perform localization and sensing with respect to available system power[3], i.e., if there is enough power for chip operation P_{chip} and enough received tag signal power P_{RX} for different tag positions within this exemplary environment. The measured transmission coefficients have been used as channel transfer functions for an assumed UHF RFID system (see Sec. 1.1.2) with state-of-the-art system parameters. Ultimately, the minimum required sensitivity of the RPRP has been derived based on these evaluations.

Measurement Setup

Figure 2.1 shows the floor plan of the room (room 1) and a neighboring room (room 2), where large metallic objects like a test bench and boxes are sketched. Three fixed antennas, TX, RX1 and RX2, have been used as the reader TX antenna and RX antennas. These Motorola AN480 [57] patch antennas have been mounted on a window at a height of 1.5 m, with a spacing of 60 cm and 90 cm between TX/RX1 and TX/RX2, respectively. The linear gain of the antennas has been measured to be about 5 dBi in an anechoic chamber at the IHF. The rectangles 1 to 34 represent the positions where the tag antenna has been positioned at the same height as the reader antennas. Two different

[3]The same channel measurements have been used by my colleagues H. N. Khan et al. for investigating the potential of DoA estimation [55], as well as for investigating power delay profiles [56] of this specific propagation environment.

types of tag antennas have been used, leading to two different scenarios. In the reference scenario, also a Motorola AN480 antenna has been used, while in the tag scenario, a custom built patch antenna with a simulated gain of −3.5 dBi has been used. The custom built antenna has been designed to emulate a realistic tag antenna with a much lower gain in comparison to the Motorola AN480 antenna. A patch design has been used to match the antenna to 50 Ω systems. By means of a 4-port VNA, the (Scattering-) S-parameters have been measured 20 times for each position in the frequency range of 700 MHz to 1200 MHz. The reader antennas TX, RX1 and RX2 have been connected to the VNA ports 1, 2 and 3, while the the tag antenna has been connected to port 4. The measurements have been evaluated at 890 MHz, as the custom built antenna shows the best matching at this frequency.
It has to be noticed, that positions 31 to 34 are not in room 1, but in room 2. These positions have been measured in order to investigate the system in case of interfering tags placed in neighboring rooms. This investigation is defined to be the interference scenario.

Evaluation Method

As presented in [8] and introduced in Sec. 1.1.2, the channel transfer functions h_{fw} and h_{bw} are determined by the transmission coefficients S_{ij}, where i and j depend on the VNA wiring. In case of a monostatic antenna configuration (TX antenna is also used as RX antenna), the channel gains G_{fw}= L_{fw} and G_{bw}= L_{bw} can then be calculated by $|S_{ij}|^2$ and $|S_{ji}|^2$. For the moment, the monostatic case is used for simplicity, but these definitions can easily be adjusted for the bistatic antenna configuration used in the room. Based on UHF RFID system parameters, two communication link thresholds have been defined. The forward link threshold T_{fw} defines the minimum required channel gain G_{fw} to ensure that the system is not forward link limited. The backward link threshold T_{bw} is defined as the minimum required combined channel gain $G_{\mathrm{fw}} + G_{\mathrm{bw}}$ (in dB) that ensures that the system is not backward link limited. T_{fw} (in dB) can be calculated by rearranging Eqn. 1.4 and exchanging P_{chip} with T_{chip} to

$$T_{\mathrm{fw}} = T_{\mathrm{chip}} - \tau - P_{\mathrm{TX}}. \tag{2.3}$$

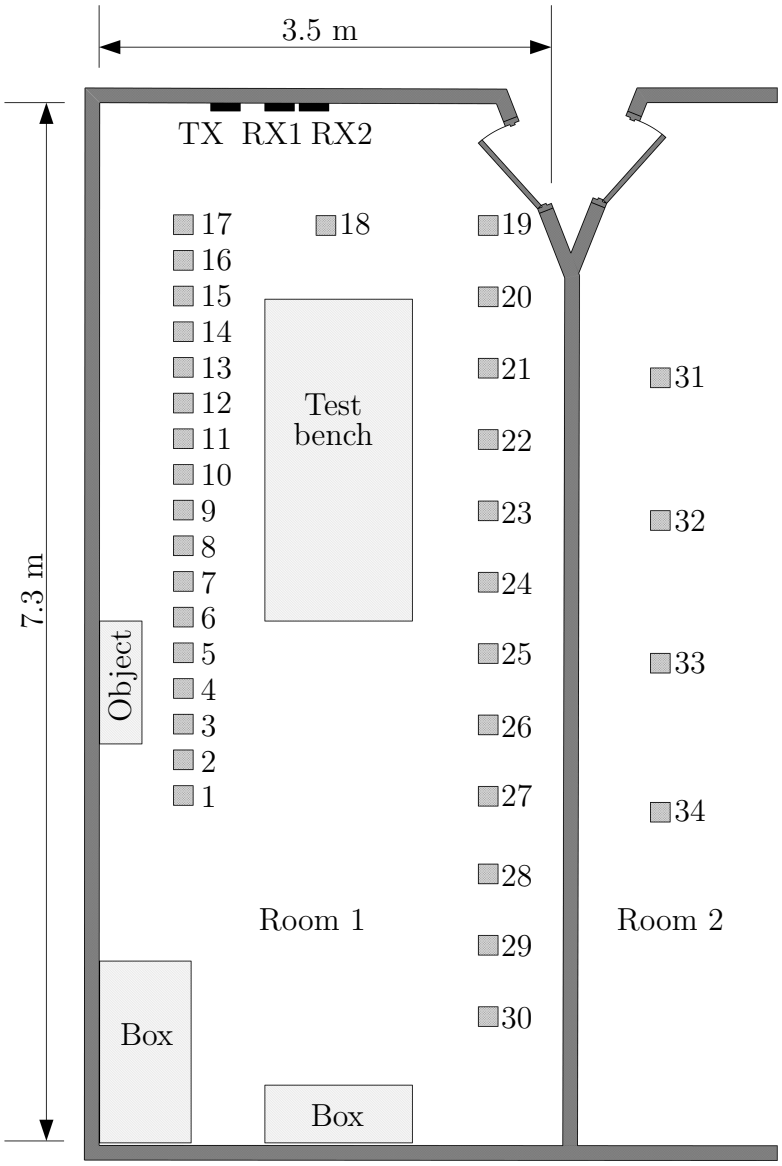

Figure 2.1: Exemplary multipath environment: Room 1 consists of metallic walls and several metallic objects like a test bench, boxes and objects. The reader antennas, TX, RX1 and RX2 (Motorola AN480) are mounted on a window at a height of 1.5 m with a defined horizontal spacing. For the measurements, the tag antenna has been positioned at several points in room 1 (positions 1 to 30). Also, interference measurements have been performed by positioning the tag antenna in the neighboring room 2 (positions 31 to 34).

T_{bw} (in dB) can be calculated by rearranging Eqn. 1.5 and exchanging P_{RX} with T_{RX} to

$$T_{\mathrm{bw}} = T_{\mathrm{RX}} - \eta - P_{\mathrm{TX}}. \tag{2.4}$$

Table 2.1 gives exemplary state-of-the-art UHF RFID system parameters that define the actual values of T_{fw} and T_{bw}. As a reference for a UHF RFID

Table 2.1: State-of-the-art UHF RFID system parameters: The system parameters are composed of parameters from a Zebra FX9500 reader and a NXP UCODE G2iL chip. The power transmission coefficient and the modulation efficiency are assumed to be ideal.

System parameter	Symbol	Value
Reader TX power	P_{TX}	30 dBm
Reader sensitivity	T_{RX}	-105 dBm
Chip sensitivity	T_{chip}	-18 dBm
Power transmission coefficient	τ	0 dB
Modulation efficiency	η	-6 dB (1/4)

reader, a Zebra FX9500 [58] has been chosen, which provides a sensitivity of $T_{\mathrm{RX}} = -105$ dBm in a bistatic mode. The output power of that reader is adjustable, but $P_{\mathrm{TX}} = 30$ dBm is assumed. This output power leads to an EIRP of about 35 dBm with the used reader antennas (5 dBi gain). A NXP UCODE G2iL chip [59] has been used as reference for a UHF RFID chip, which provides a sensitivity of $T_{\mathrm{chip}} = -18$ dBm. The power transmission coefficient τ and the modulation efficiency η are assumed to be ideal. The chosen system parameters lead to $T_{\mathrm{fw}} = -48$ dB and $T_{\mathrm{bw}} = -129$ dB. For the bistatic antenna configuration, two different backward channel gains $G_{\mathrm{bw},1}$ and $G_{\mathrm{bw},2}$ have to be considered.
The assumed UHF RFID system in the room is said to be 100% reliable, or the system outage probability is 0%, if all measured channel gains at all positions are above the corresponding thresholds. The outage probabilities of the forward link P_{fw} and the two backward links $P_{\mathrm{bw},1}$, $P_{\mathrm{bw},2}$ are defined as the probability that the corresponding channel gains are less or equal than T_{fw} and

T_{bw}, respectively [8]:

$$P_{\mathrm{fw}} = P\{G_{\mathrm{fw}} \leq T_{\mathrm{fw}}\}, \tag{2.5}$$

$$P_{\mathrm{bw},1} = P\{G_{\mathrm{fw}} + G_{\mathrm{bw},1} \leq T_{\mathrm{bw}}\}, \tag{2.6}$$

$$P_{\mathrm{bw},2} = P\{G_{\mathrm{fw}} + G_{\mathrm{bw},2} \leq T_{\mathrm{bw}}\}. \tag{2.7}$$

It has to be noted that an outage probability of $P_{\mathrm{bw},i} = 0\%$ does not exclude an outage probability of $P_{\mathrm{fw}} > 0\%$, i.e., that the system is forward link limited. The system outage probability can be visualized by means of cumulative distribution functions (CDFs) [8]. These CDFs are composed of the calculated channel gains of the measured transmission coefficients for the corresponding scenarios. The intersection point of the CDFs with the corresponding channel threshold can then be directly related to the outage probability of the different links. The evaluation of the system reliability is presented below.

Evaluation

The evaluation of the channel measurements now gives a statement about the UHF RFID system performance in the room with the chosen system parameters (see Tab. 2.1). Furthermore, the evaluation is used to find minimum requirements on the system parameters and thus the minimum requirements for the RPRP.
Figure 2.2 shows the system performance of the reference scenario. The intersection of the forward link CDF with the forward link threshold T_{fw} gives the outage probability of the forward link. It can be seen that the outage probability of the forward link is 0 % and that there is no limitation. Furthermore, the outage probability of both backward links is 0 % and thus, the UHF RFID system works reliable for this scenario.
Figure 2.3 shows the system performance of the interference scenario. It is desirable that there is no communication possible, i.e., that there are no interfering tags from the neighboring room. It can be seen that there is an outage probability of 75 % in the forward link and no limitations in the backward links. This means that in 25 % of the measurements a communication between the reader and a tag is possible. However, the use of the large patch antenna provides a worst case scenario and a reduction of the tag antenna gain would lead to an outage probability of 100 %, i.e., no interfering tags.

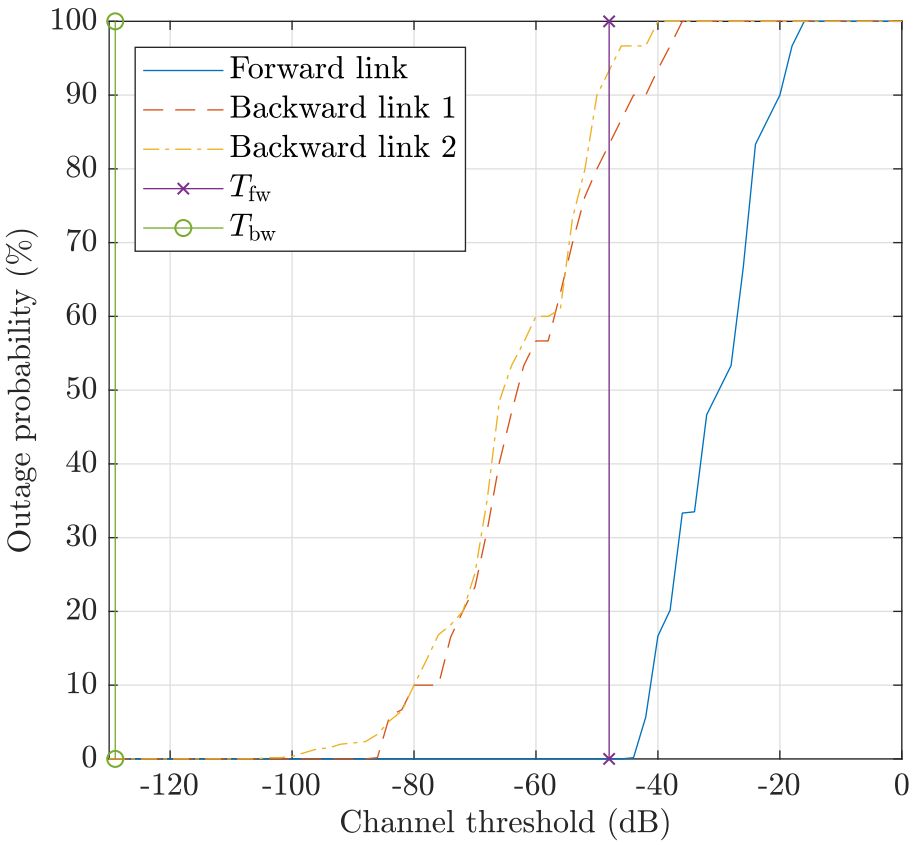

Figure 2.2: Reference scenario outage probability: A Motorola AN480 antenna is used as tag antenna. The outage probability in the forward link and the backward links is 0 % for the given system parameters.

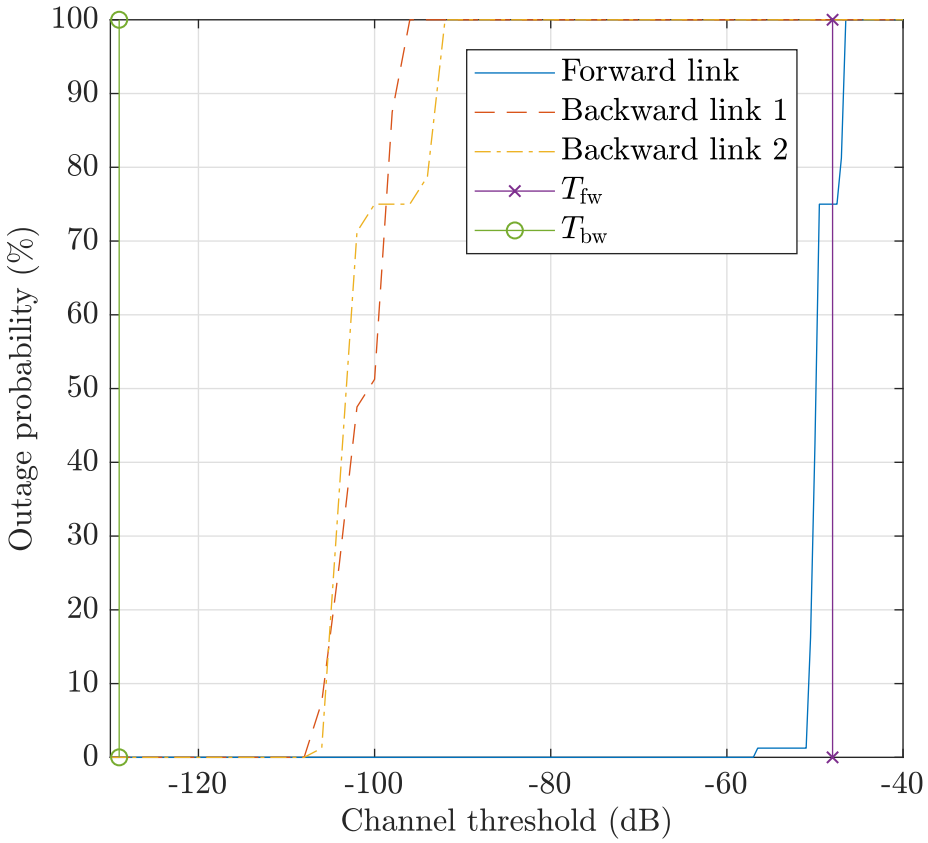

Figure 2.3: Interference scenario outage probability: A Motorola AN480 antenna is used as tag antenna, leading to a worst case scenario. The outage probability of the forward link is 75 % and 0 % for the two backward links. An interference occurs with a probability of 25 %.

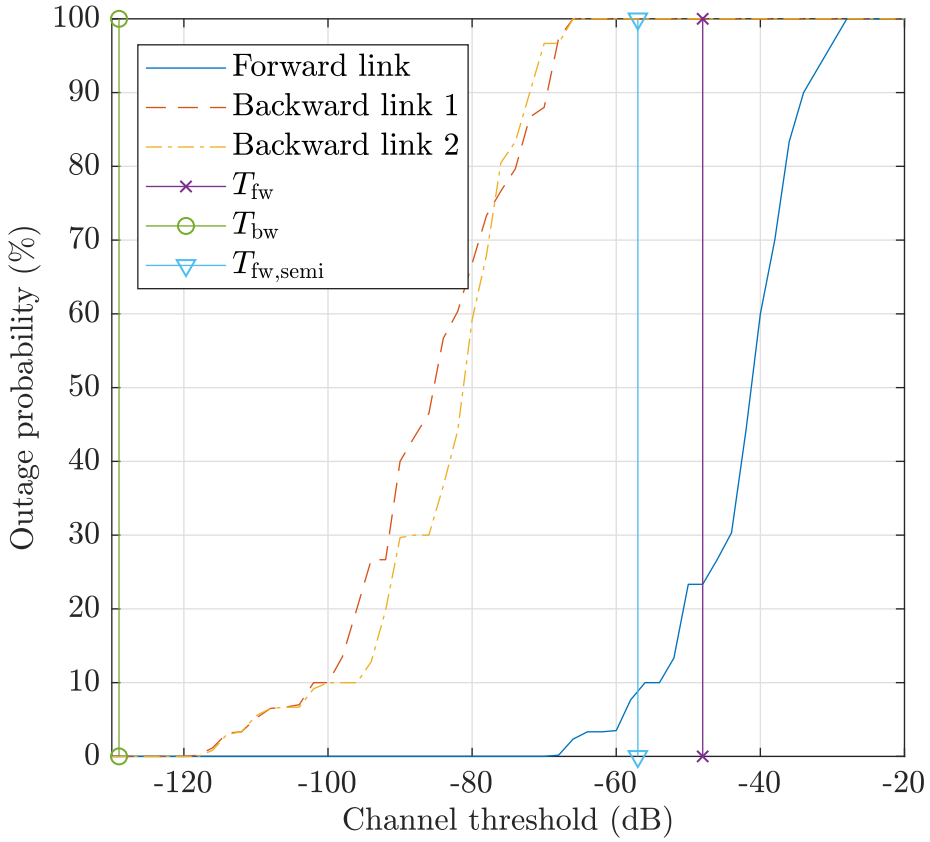

Figure 2.4: Tag scenario outage probability: A custom built patch antenna with a low gain of -3.5 dB is used as tag antenna. The outage probability of the forward link is about 23 %, when using a passive tag ($T_{\text{chip}} = -18$ dBm) and about 8 %, when using a semi-passive tag ($T_{\text{chip}} = -27$ dBm). The outage probability of the backward links is 0 %.

Figure 2.4 finally shows the system performance of the tag scenario. With the small custom built patch antenna, the outage probability of the forward link is about 23 %, while there is no limitation in the backward links. The tag would not receive enough power to operate its chip in 23 % of the measurements. This value can be decreased to about 8 %, when using a semi-passive tag. These tags are battery assisted and the sensitivity can be increased by −9 dB (NXP UCODE G2iL chip [59]), which leads to a forward link threshold of $T_{\mathrm{fw,semi}}$ of −57 dB.
The final step of the system performance evaluation is to find the minimum system requirements in order to assure a system outage probability of 0 % in the tag scenario. From Fig. 2.4 it can be seen that the backward link threshold and thus the minimum reader sensitivity can be reduced by 11 dB without getting a limitation in the backward links. Therefore, the minimum reader sensitivity is found to be $T_{\mathrm{RX}} = -94$ dBm. In order to prevent limitations in the forward link, the forward link threshold has to be reduced to −69 dB. The assumed output power of $P_{\mathrm{TX}} = 30$ dBm leads to an EIRP of 35 dBm and is thus already at the upper limit of the ETSI and FCC regulations. The second possibility is to increase the sensitivity of the chip to at least −39 dBm. There is one company that claims to achieve a chip sensitivity of −40 dBm (Intelleflex XC3 chip [60], semi-passive), which would fulfill that requirements.
With the findings above, also minimum requirements of the RPRP can be determined. Obviously, the minimum reader sensitivity of the RPRP in order to prevent limitations of the performance in the room is found to be $T_{\mathrm{RX}} = -94$ dBm, when assuming a chip sensitivity of −40 dBm. The requirements on the reader sensitivity are decreasing, when using tags with lower chip sensitivity, because the limitation might then already be in the forward link. When using the semi-passive NXP chip with a sensitivity of −27 dBm and removing the positions, where at least one measured channel gain is below the threshold (positions 19, 20 and 23), then the minimum required receiver sensitivity is reduced to $T_{\mathrm{RX}} = -78$ dBm. When neglecting the positions that are forward link limited when using the passive NXP tag with a sensitivity of −18 dBm, the minimum required receiver sensitivity is $T_{\mathrm{RX}} = -72$ dBm. Table 2.2 summarizes the minimum required receiver sensitivity of the RPRP – and in general of an UHF RFID reader – in the room depending on the chip sensitivity of the tags. The table also shows the corresponding forward link outage probabilities.

Table 2.2: Minimum required RPRP receiver sensitivity: The minimum required reader sensitivity T_{RX} depends also depends on the chip sensitivity T_{chip}. A higher chip sensitivity decreases the outage probability of the forward link P_{fw}, but increases the required T_{RX}.

T_{chip}	Minimum required T_{RX}	P_{fw}
-40 dBm	-94 dBm	0 %
-27 dBm	-78 dBm	8 %
-18 dBm	-72 dBm	23 %

2.2 Setup and Performance

Figure 2.5 shows the setup of the RPRP. The heart of the RPRP is a SDR (USRP[4] 2942R) from National Instruments that is controlled by a notebook. The SDR is a 2x2 MIMO system providing two independent receive and transmit chains. The SDR provides a frequency range from 400 MHz to 4.4 GHz, but the frequency range of the RPRP is further defined by the used PAs and antennas. However, both, the ETSI and FCC bands are covered by the RPRP.
Two PAs [61] are used to increase the transmit signal to a sufficient level at the TX1/2 antenna inputs. The use of the TX2 antenna is optional and might be used for increasing the interrogation range. A switch matrix can be used for an initial system calibration that is necessary e.g., for DoA estimation. For the calibration purpose, the matrix directly switches one SDR output to both SDR inputs, which will be discussed later. During the normal operation, the two SDR outputs are switched to the two power amplifiers and the two receive antennas (RX1/2) are switched to the two SDR inputs. The RPRP uses the same Motorola AN480 antennas that have been used for the measurements in the exemplary room.
The maximum measured output power of the SDR is 17 dBm, while the minimum measured output power is about 2.5 dBm. This leads to an adjustable output power range of 14.5 dB. The actual output power of the RPRP is determined by the gain of the PAs (45 dB) and an additional attenuation between the SDR and the PAs. With an attenuation of 26 dB, P_{TX} can be

[4] universal software radio peripheral

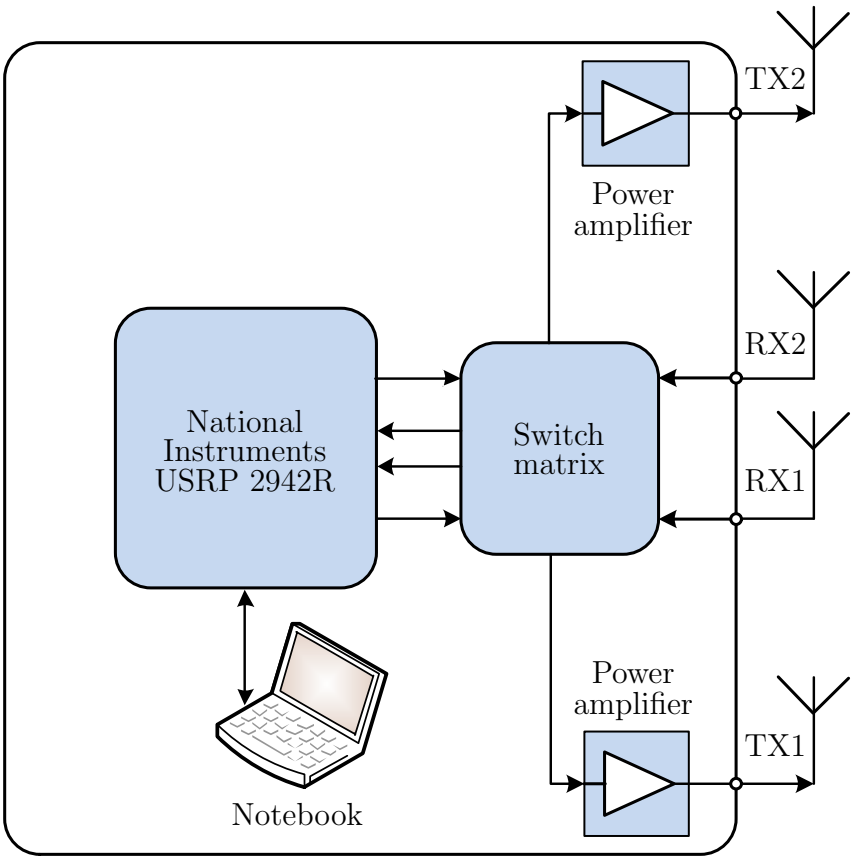

Figure 2.5: Rapid prototyping platform: The RPRP consists of a USRP 2942R from National Instruments, a switch matrix, two power amplifiers (PAs), two receiving antennas RX1, RX2 and two transmitting antennas TX1 and TX2. The software defined radio (SDR) provides a frequency range from 400 MHz to 4.4 GHz, while the frequency range of the RPRP is restricted by the used PAs and antennas. The sensitivity of the RPRP is about $T_{\mathrm{RX}} = -80$ dBm and a detection of the tag signal amplitude and phase is possible.

adjusted between 21.5 dBm and 36 dBm.
According to the specifications, the SDR provides an instantaneous BW of 40 MHz and a NF of 5−7 dB. Assuming an operating temperature of $T_0 = 300$ K and applying Eqn. 2.2, the SDR provides a sensitivity of $T_{\mathrm{RX}} = -80.8$ dBm ($NF = 7$ dB) for FM0 modulation. The sensitivity of the whole RPRP has been measured in the anechoic chamber. For this measurement, a tag has been positioned in the middle of the chamber about 1.65 m away from the reader antennas. The attenuation between the RX antenna and the RPRP input has been increased until no tag signal could be detected anymore.
Figure 2.6 shows the received baseband signals $r_{\mathrm{I}}(t)$ (I component), $r_{\mathrm{Q}}(t)$ (Q component) and $r(t) = \sqrt{r_{\mathrm{I}}(t)^2 + r_{\mathrm{Q}}(t)^2}$, where a detection of the tag signal was just possible. Between about 0.15 ms and 1.05 ms, a transmitted query command of the reader is received. The tag response, which is a 16 bit random number with a header, is detected between about 1.2 ms and 1.6 ms. The tag signal can easily be found in $r_{\mathrm{I}}(t)$, while it is hardly visible in $r_{\mathrm{Q}}(t)$. The noise content of the corresponding I/Q component strongly depends on the phase difference between the strong leakage signal and the receiver LO signal [3]. As the noise is high for a small leakage component, in this case the Q component, the source for this noise is found by phase noise of the transmitted signal [3].
Figure 2.7 shows the tag signal $h(t)$, which is an extract of $r(t)$ from 1.2 ms to 1.57 ms, but with a removed DC component. Note that $h(t)$, compared to h (see Fig. 2.8), does not contain a tag signal phase information or a DC component. $h_{\mathrm{recon}}(t)$ denotes the reconstructed tag signal that is used for the calculation of the reader receiver sensitivity T_{RX}. Considering the 50 Ω system, the tag signal power and thus T_{RX} has been estimated to:

$$T_{\mathrm{RX}} = 10\log(\mathrm{RMS}(h(t))^2/50) = -79.8 \text{ dBm}, \tag{2.8}$$

where RMS is the root mean square function of Matlab. This value is quite near to the theoretical calculated SDR sensitivity of $T_{\mathrm{RX}} = -80.8$ dBm. The SNR of the received tag signal has been estimated to about 13.3 dB, where the noise signal was assumed to be $h_{\mathrm{recon}}(t) - h(t)$.
Figure 2.8 shows the baseband signal constellation of the tag signal $h = S^{(B)} - S^{(A)}$. $S^{(B)}$ (reflecting state) and $S^{(A)}$ (absorbing state) are also estimated by means of the time signals $r_{\mathrm{I}}(t)$ and $r_{\mathrm{Q}}(t)$. The corresponding samples again show that the Q component of the tag signal is much noisier. With this signal representation, the received tag signal power P_{RX}, which is in this case equal to T_{RX}, can be calculated with Eqn. 1.14 and $\alpha = -6$ dB to

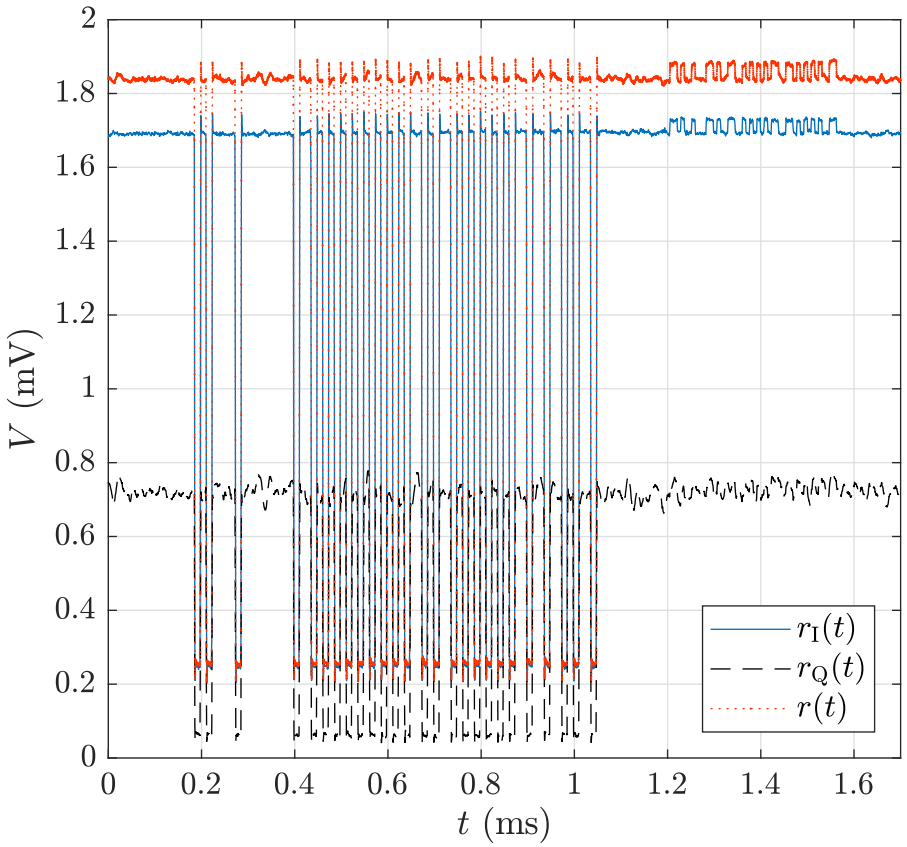

Figure 2.6: Received baseband signal over time: The measured received baseband signal $r(t)$ is composed of an I component $r_I(t)$ and a Q component $r_Q(t)$, where $r(t) = \sqrt{r_I(t)^2 + r_Q(t)^2}$. A reader query command can be seen between 0.15 ms and 1.05 ms, while the tag response (16 bit random number) is visible between 1.2 ms and 1.6 ms. The amplitude noise of $r_Q(t)$ can be traced back to the phase noise of the transmitted signal [3]. This received baseband signal is used for the determination of the receive sensitivity of the RPRP.

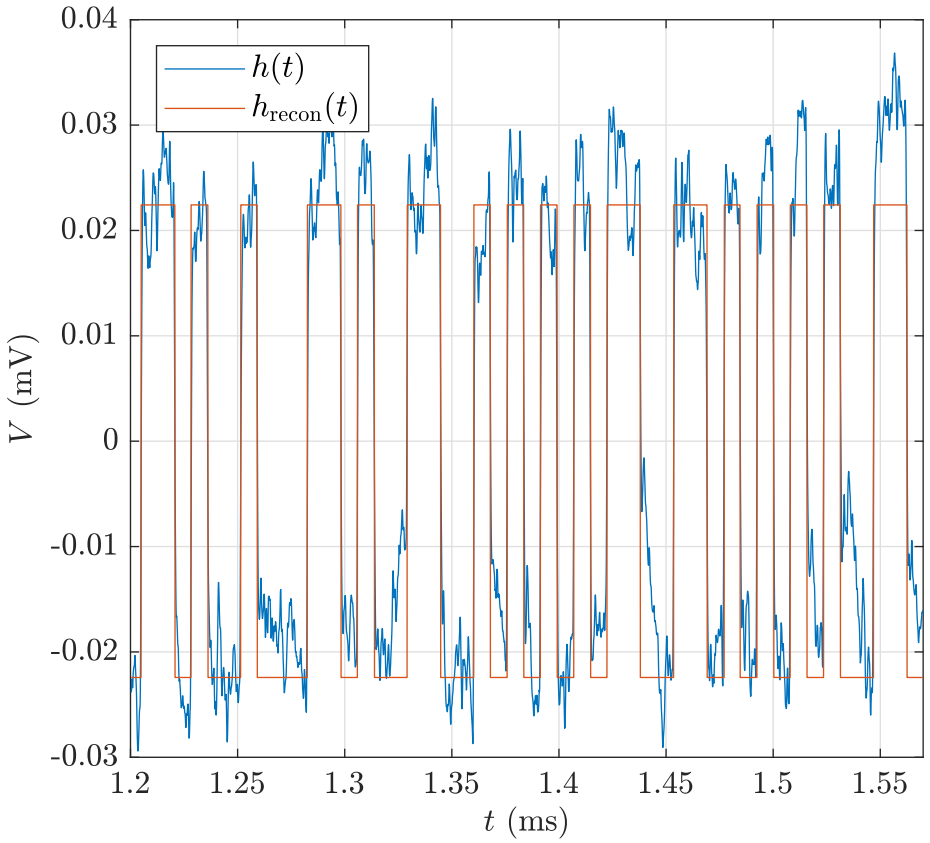

Figure 2.7: Received baseband tag signal over time: The tag signal $h(t)$ is obtained from $r(t)$ by removing the DC component and is reconstructed to $h_{\mathrm{recon}}(t)$. The receiver sensitivity is estimated to $T_{\mathrm{RX}} = -79.8$ dBm with a SNR of about 13.3 dB.

$P_{\mathrm{RX}} = T_{\mathrm{RX}} = -80.3$ dBm. Note that the reference impedance (system input impedance) of h in Fig. 2.8 is 50 Ω, which has to be considered for the power calculations.
The sensitivity considerations above are based on a single time signal and might therefore slightly change for different cases, e.g. a different random number. However, a RPRP receive sensitivity of around $T_{\mathrm{RX}} = -80$ dBm can be assumed. As can be seen in Tab. 2.2, this sensitivity is sufficient when using passive or semi-passive tags with a chip sensitivity of −18 dBm and −27 dBm, respectively, but not for semi-passive tags with $T_{\mathrm{chip}} = -40$ dBm.
The input power of the two receiver chains of the SDR is limited to −15 dBm. This upper power limit has to be considered, especially when the RPRP is operated in multipath environments, where the leakage into the RX antennas can be large. In such situations, additional attenuators can be connected between the RX antennas and the switch matrix.

2.3 Summary

This chapter presents a RPRP that has been developed initially in order to allow a rapid prototyping and testing of UHF RFID tracking and sensing systems. The requirements on the RPRP have been identified with respect to the targeted applications and channel measurements within an exemplary multipath propagation environment. This harsh environment can be seen as a worst case scenario for a system implementation. All identified requirements can be covered with the RPRP, when using passive ($T_{\mathrm{chip}} = -18$ dBm) or semi-passive ($T_{\mathrm{chip}} = -27$ dBm) state-of-the-art tags.

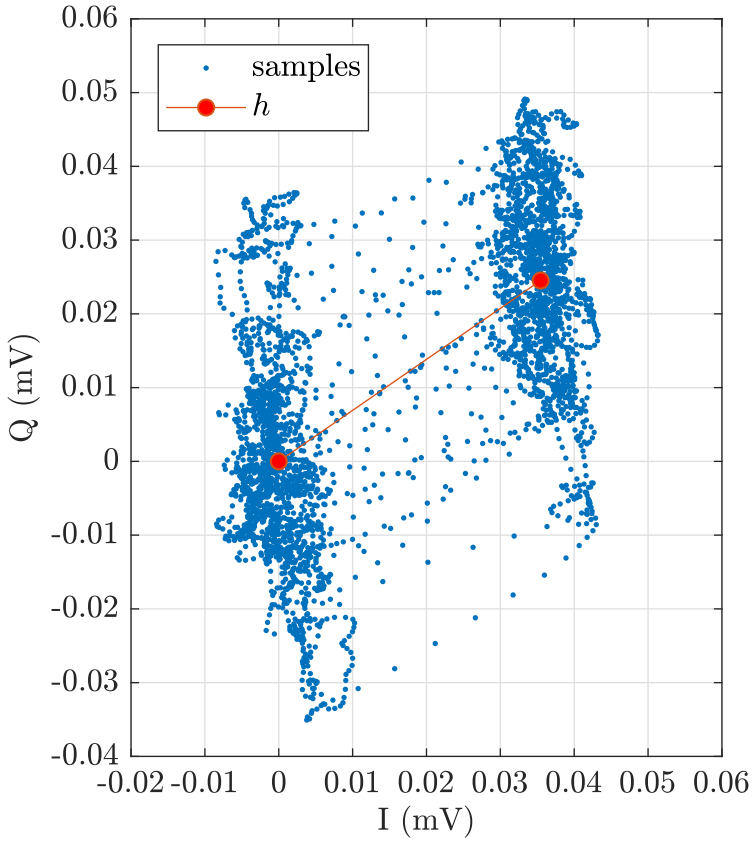

Figure 2.8: Baseband tag signal constellation: The tag signal h is estimated from the leakage compensated I and Q time samples. Amplitude and phase of the tag signal can be observed from this signal representation (see Fig. 1.2). The reader sensitivity is estimated by Eqn. 1.14 to $T_{\mathrm{RX}} = -80.3$ dBm, with the reference impedance (system input impedance) of 50 Ω.

3 Tracking System

This chapter presents a novel tag tracking system that provides robust and fast 2D tag position updates. The tracking system uses a single input multiple output (SIMO) antenna configuration, where the TX and RX antennas are horizontally separated at the same height. Such an antenna configuration only occupies one side of a room and is thus very compact.
Known PDoA techniques, which are summarized and theoretically investigated in [26], have been used as a starting point for the investigations. For the first time, a 2D localization system has been implemented by combining the SD-PDoA and an adapted FD-PDoA techniques. The adapted FD-PDoA technique allows the use of this technique in systems with SIMO antenna configurations. The performance of this novel 2D PDoA localization system is investigated in Sec. 3.1. Measurements show that this system is not very robust to multipath propagation and is thus only useful in a limited way in typical application environments. The most promising PDoA technique in multipath propagation environments according to [26] is the TD-PDoA technique. This technique, however, only provides the projected velocity or distance of a tag towards the reader, which is not sufficient for tag tracking.
Finally, however, I managed to implement a 2D tag tracking system that is based on the TD-PDoA technique, which is thus very robust in multipath environments. In this system, antenna diversity and simultaneous tag signal phase measurements allow to extend the measuring of projected distances to 2D position updates. Sec. 3.2 shows the tracking algorithm and the measurements of the implemented algorithm in an anechoic chamber as well as in a laboratory environment.

Original Publications Related to this Chapter

L. Görtschacher, J. Grosinger, H.N. Khan, D. Amschl, P. Priller, U. Muehlmann, and W. Bösch, "SDR Based RFID Reader for Passive Tag Localization Using Phase Difference of Arrival Techniques." In: *Proc. IEEE MTT-S International Microwave Symposium (IMS)*, 2016.

L. Görtschacher, J. Grosinger, H.N. Khan, and W. Bösch, "Fast Two Dimensional Position Update System for UHF RFID Tag Tracking." In: *Proc. IEEE MTT-S International Microwave Symposium (IMS)*, 2017.

3.1 Localization System

The 2D localization system is based on the combination of two PDoA techniques, the SD-PDoA and the FD-PDoA technique. In literature, the SD-PDoA technique is used to perform DoA (Θ) estimation, while the FD-PDoA technique is used for range (R) estimation. A combination of these two techniques needs an adaption, as both are based on a bistatic and a monostatic antenna configuration, respectively. In the following, the DoA and the range estimation are presented and analyzed separately, before the combined performance is shown.
Figure 3.1 shows a sketch of the 2D localization system in top view with a tag to be localized, by estimating Θ and R. The origin of the Cartesian coordinate system lies between the two receiving antennas RX1 and RX2. The antennas of the RPRP are horizontally separated by $d_{\mathrm{TX,RX1}}$ and $d_{\mathrm{TX,RX2}}$. The localization system operates with three different frequencies, $f_0 = 869$ MHz, $f_1 = 866$ MHz and $f_2 = 872$ MHz, which are transmitted consecutively.
The PDoA techniques require some previous knowledge about the signal phase relations within the system. Thus an initial system calibration is necessary, which is presented in the following.

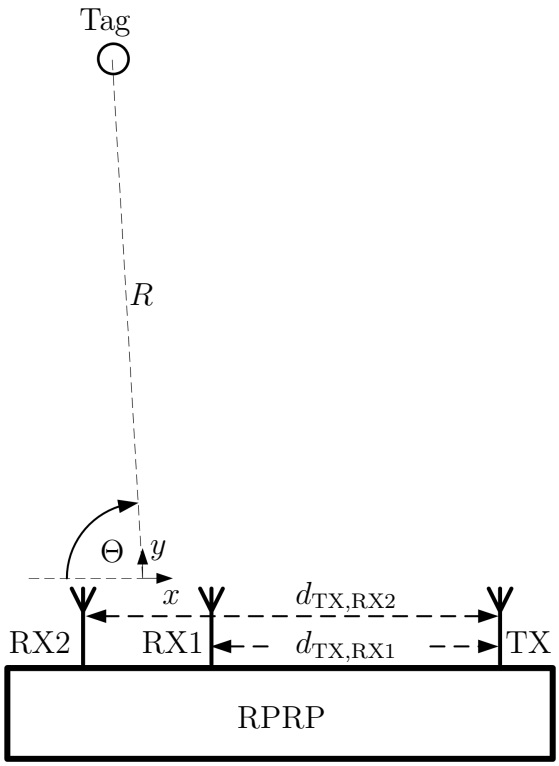

Figure 3.1: 2D localization system: The origin of the Cartesian coordinate system is between RX1 and RX2. The bistatic system consists of one TX and two RX antennas that are horizontally separated by $d_{\mathrm{TX,RX1}}$ and $d_{\mathrm{TX,RX2}}$, respectively. Reader antennas and tag are at the same height.

System Calibration

The use of PDoA techniques for tag localization requires an initial system calibration. This calibration is needed for a correct tag signal phase detection and is performed once[1]. The initial calibration process is done with a wired connection between RPRP output and inputs in the calibration mode, as depicted in Fig. 3.2a. DoA and range estimation use the same calibration setup, although the calibration process is different. Details about the calibration for DoA and range estimation are discussed in the following.
DoA estimation requires the knowledge of the phase difference of the receiver chains of the RPRP inputs. This phase difference is measured by feeding both receiver chains with the same sinusoidal signal. For this, the RPRP switches the output of the SDR to the two inputs of the SDR (see Fig. 3.2a). Finally, the DoA estimation considers this measured phase misalignment in the calculations.
For range estimation, the phase relations between all three operating frequencies f_0, f_1 and f_2 have to be known at a specific reference plane. For this, again, the output of the SDR is switched to the two inputs (see Fig. 3.2a) and the signal phase for all three frequencies is measured. This measurement shifts the range reference planes to both inputs of the SDR and considers the length offset introduced by devices (cables, switch matrix, etc.) incorporated in the calibration path. A total range calibration can be achieved, if the length offset of the calibration path is the same length offset introduced in the normal mode when performing range measurements. The RPRP in the normal mode is shown in Fig. 3.2b. The length offset in this mode is introduced by the devices incorporated in the transmitting and receiving chain, like e.g., the antennas, the power amplifier, the cables and the switch matrix. For a total range calibration, the cable length in the calibration path has to be adjusted.

3.1.1 DoA Estimation

The DoA estimation is based on the spatial separated reception of the backscattered tag signal at two receiving antennas RX1 and RX2 [26]. Let $\varphi_{h,\mathrm{RX1}}$ and $\varphi_{h,\mathrm{RX2}}$ be the phases of the tag signal when received at RX1 and RX2, respectively and $\Delta\varphi_{\mathrm{D}} = \varphi_{h,\mathrm{RX2}} - \varphi_{h,\mathrm{RX1}}$ the difference, then the DoA can be

[1] A further calibration has to be done after a system reset.

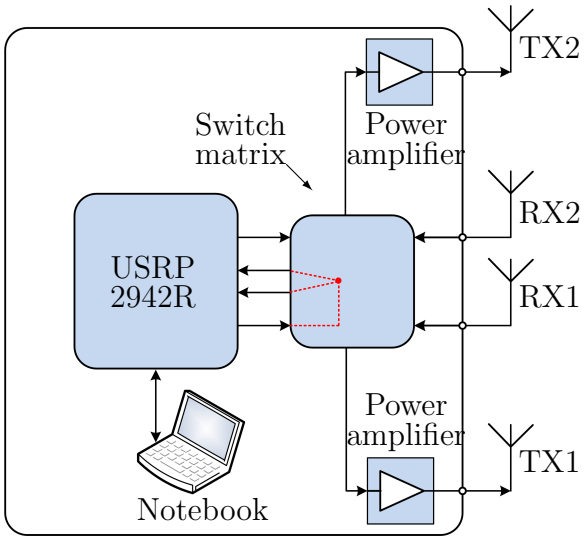

(a) RPRP calibration mode: The same signal is fed to the two inputs of the SDR by the switch matrix and the signal phases are measured.

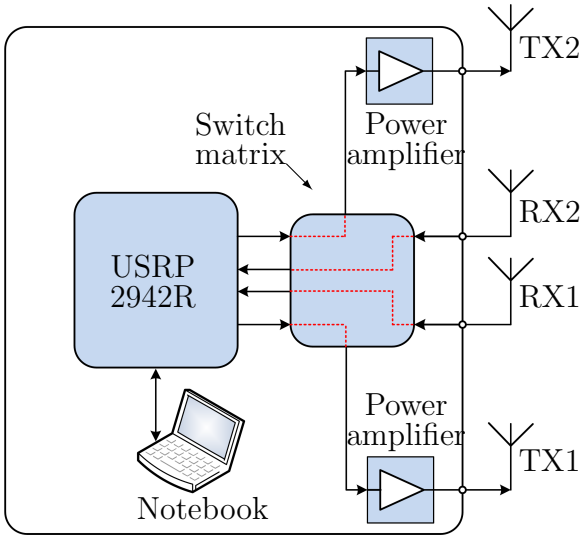

(b) RPRP normal mode: The antennas are switched to the corresponding SDR ports.

Figure 3.2: System calibration: For an initial calibration, the RPRP is set to calibration mode, where phase relations of the system at all frequencies are measured. These phase measurements are then considered in the normal mode when localization is performed.

calculated as

$$\Theta = \cos^{-1}\left(\frac{c}{2\pi f}\frac{\Delta\varphi_{\mathrm{D}}}{d}\right), \tag{3.1}$$

where c is the speed of light, f the operating frequency and $d = d_{\mathrm{TX,RX2}} - d_{\mathrm{TX,RX1}}$ the distance between RX1 and RX2. The equation assumes that the tag is far away from the RX antennas [26]. The $\cos^{-1}(x)$ function is defined for $-1 < x < 1$, meaning that $\left|\frac{c}{2\pi f}\frac{\Delta\varphi_{\mathrm{D}}}{d}\right|$ has to be lower than 1. Due to the 2π-periodicity of the tag signal phase, only values of $\Delta\varphi_{\mathrm{D}}$ between $-\pi$ and π are possible. When allowing the full span of $\Delta\varphi_{\mathrm{D}}$, d has to be chosen larger than $\lambda/2$ to fulfill the requirements of the $\cos^{-1}(x)$ function. For an antenna spacing d close to $\lambda/2$, the DoA can be determined almost between 0° and 180°. For larger values of d, the span of the DoA gets restricted and thus also a large antenna spacing has to be avoided.

Measurements

The DoA algorithm has been implemented on the RPRP in order to test the performance of the algorithm. The DoA measurements have then been conducted in an anechoic chamber as shown in Fig. 3.3. A styrofoam carrier has been placed parallel (see Fig. 3.3a) and orthogonal (see Fig. 3.3b) to the receiver antennas RX1 and RX2. RX1 and RX2 are separated by $d = 0.3$ m, while the used transmit antenna TX1 is mounted with $d = 0.6$ m on the right side of RX1. As already mentioned above, the used antenna setup allows a DoA detection for a horizontal area spanned by x and y and thus a 2D DoA detection. Vertical tag directions cannot be detected without a third RX antenna.
The tag (Sokymat Inline UHF tag [62]) has now been positioned in 0.2 m steps on the styrofoam carrier. For the parallel placement, the tag has been positioned between $x = -1$ m and $x = 1$ m for a fixed distance of $y = 1.75$ m, while for the orthogonal placement, the tag has been positioned between $y = 0.75$ m and $y = 2.75$ m for $x = 0$ m. Figures 3.4 and 3.5 show the measurements of the DoA for the parallel and orthogonal placement, respectively. The communication with the tag at the two most left positions was limited in the forward link and these positions are thus not considered.
The DoA has been measured at all three operating frequencies f_0, f_1 and f_2. The

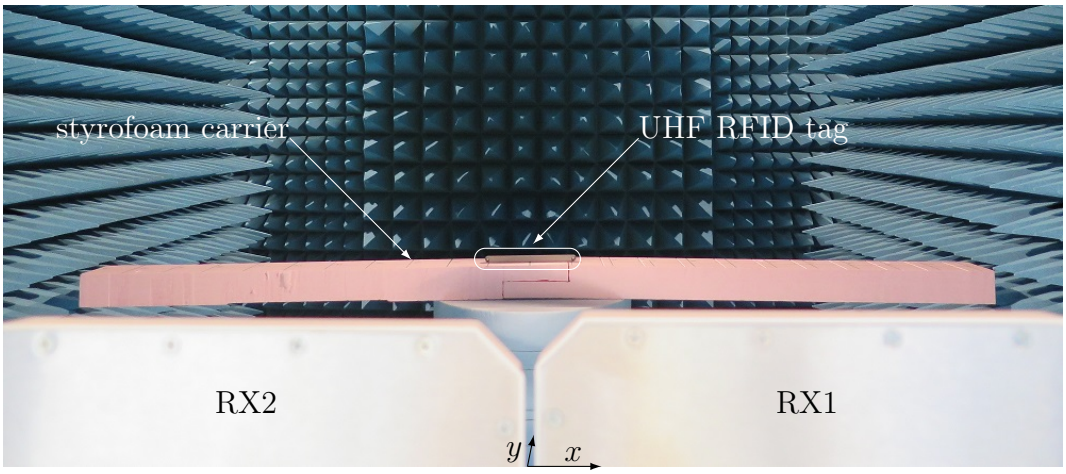

(a) Parallel positions: The x coordinate has been stepped from -1 m to 1 m at a fixed y coordinate of 1.75 m.

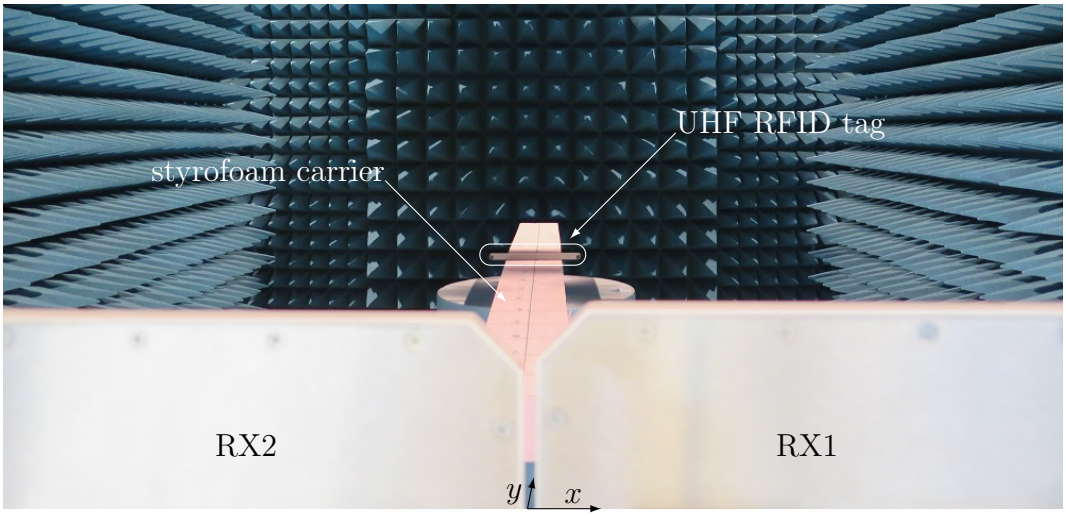

(b) Orthogonal positions: The y coordinate has been stepped from 0.75 m to 2.75 m at a fixed x coordinate of 0 m.

Figure 3.3: Position measurement in anechoic chamber: The reader antennas are separated by $d_{\mathrm{TX,RX1}} = 0.6$ m and $d_{\mathrm{TX,RX1}} = 0.9$ m. The tag has been moved in 0.2 m steps on the styrofoam carrier for DoA and range measurements.

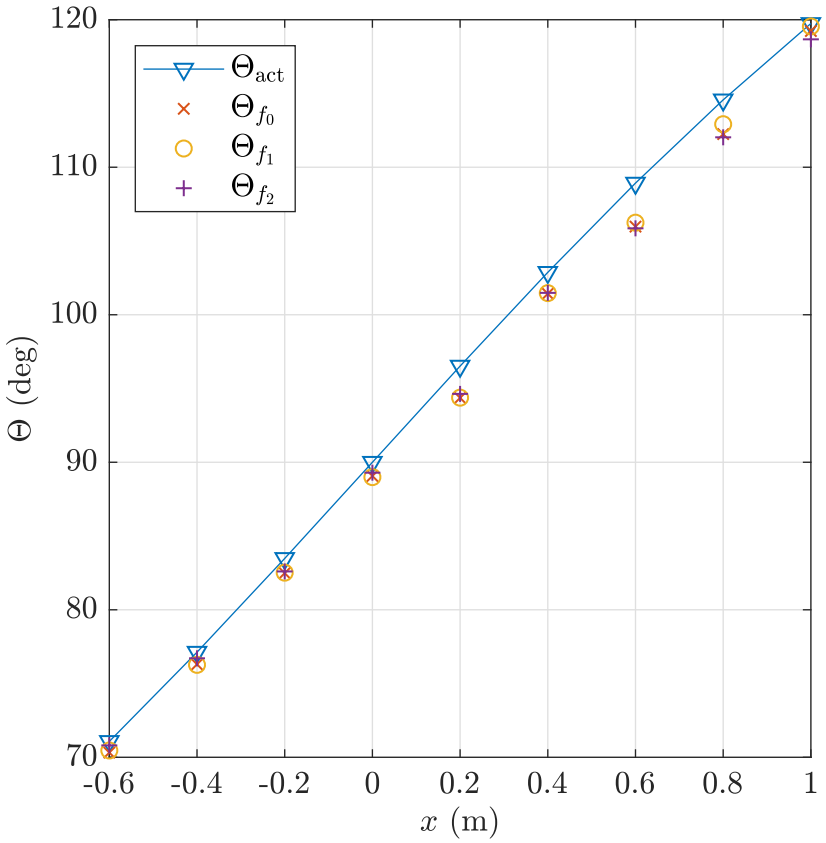

Figure 3.4: DoA measurement in anechoic chamber 1: DoA measurements of the parallel positions. Actual values are compared to the estimated values at all three frequencies.

corresponding DoAs Θ_{f_0}, Θ_{f_1} and Θ_{f_2} are compared to the actual value Θ_{act}. It can be observed that Θ_{f_0}, Θ_{f_1} and Θ_{f_2} follow Θ_{act} very well. The maximum absolute DoA error of about 3° can be observed for the position $(0.8, 1.75)$. However, it can be seen that the measured DoAs are by trend lower than the actual value. The most likely reason for it is a small misalignment between reader antennas and tag positions. By considering the orthogonal positions only, a maximum absolute DoA error of lower than 1.2° can be observed.

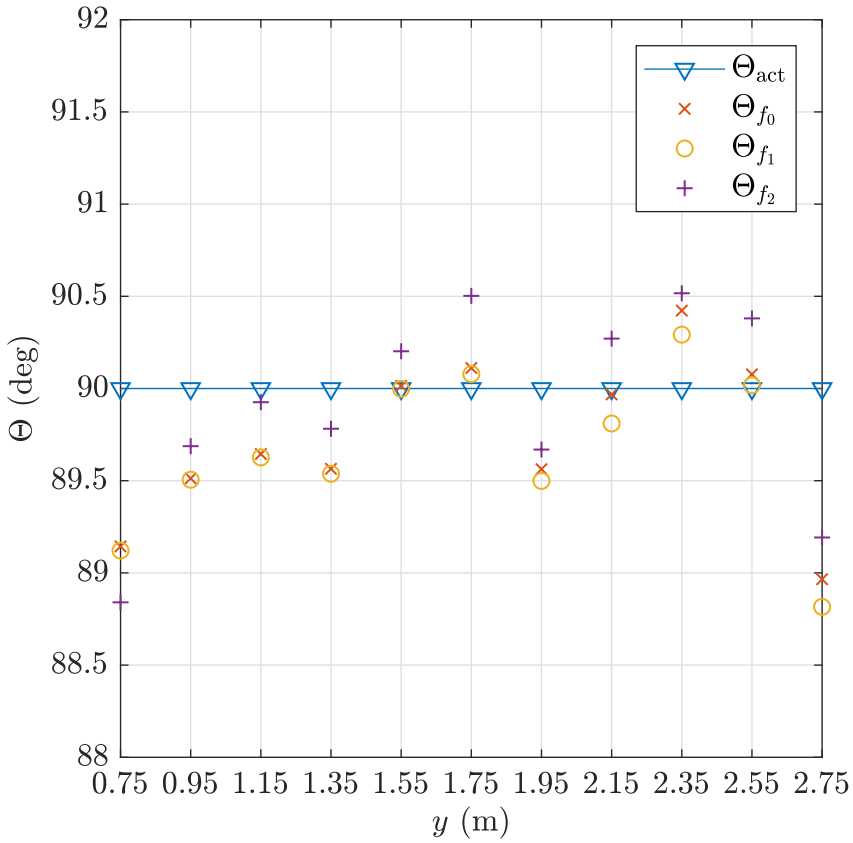

Figure 3.5: DoA measurement in anechoic chamber 2: DoA measurements of the orthogonal positions. Actual values are compared to the estimated values at all three frequencies.

3.1.2 Range Estimation

The range (distance) estimation is based on the reception of the backscattered tag signal at two different operating frequencies at a monostatic reader [26]. Let φ_{h,f_1} and φ_{h,f_2} be the phases of the tag signal when received at f_1 and f_2, respectively and $\Delta\varphi_{\mathrm{R}} = \varphi_{h,f_2} - \varphi_{h,f_1}$ the difference, then the range R can be calculated as

$$R = \frac{c}{4\pi}\frac{\Delta\varphi_{\mathrm{R}}}{\Delta f}, \tag{3.2}$$

where $\Delta f = f_2 - f_1$. The equation assumes that the tag has not moved between the consecutive communication cycles and that all other phase offsets (cable, antennas, etc.) can be calibrated out [26]. It can be seen that the maximum range is strongly influenced by the term $\frac{\Delta\varphi_{\mathrm{R}}}{\Delta f}$. Again, $\Delta\varphi_{\mathrm{R}}$ can only have values between $-\pi$ and π, or by adding π, between 0 and 2π. It follows, that the maximum range is found by $\frac{c}{2\Delta f}$.

Bistatic Range Estimation

The previously presented range estimation is only valid for monostatic readers, i.e., the distance from the TX antenna to the tag and the distance from the tag to the RX antenna are equal. However, in a bistatic system, the concept of range estimation has to be adapted. The concept of range estimation with a bistatic reader combines the monostatic range estimation and the DoA estimation. The adaptation can be explained by means of Fig. 3.6, where a monostatic reader (Fig. 3.6a) and a bistatic reader (Fig. 3.6b), the RPRP, are sketched.
The estimation of R in Eqn. 3.2 is based on the bisection of the distance from the TX antenna to the tag and back to the RX antenna. As can be seen in Fig. 3.6a, where TX antenna and RX antenna is the same, this assumption is true. Applying the same equation for the bistatic reader in Fig. 3.6b, the range would be estimated to $R = \frac{d_{\mathrm{TX}}+d_{\mathrm{RX1}}}{2}$, which is not the actual bistatic range R_{b}. When using the relation that $2R = d_{\mathrm{TX}} + d_{\mathrm{RX1}}$ and the knowledge of Θ, $d_{\mathrm{TX,RX1}}$ and d, the actual range R_{b} can be calculated by means of the law of cosines. Depending on the considered RX antenna, R_{b} is written as R_{RX1} or

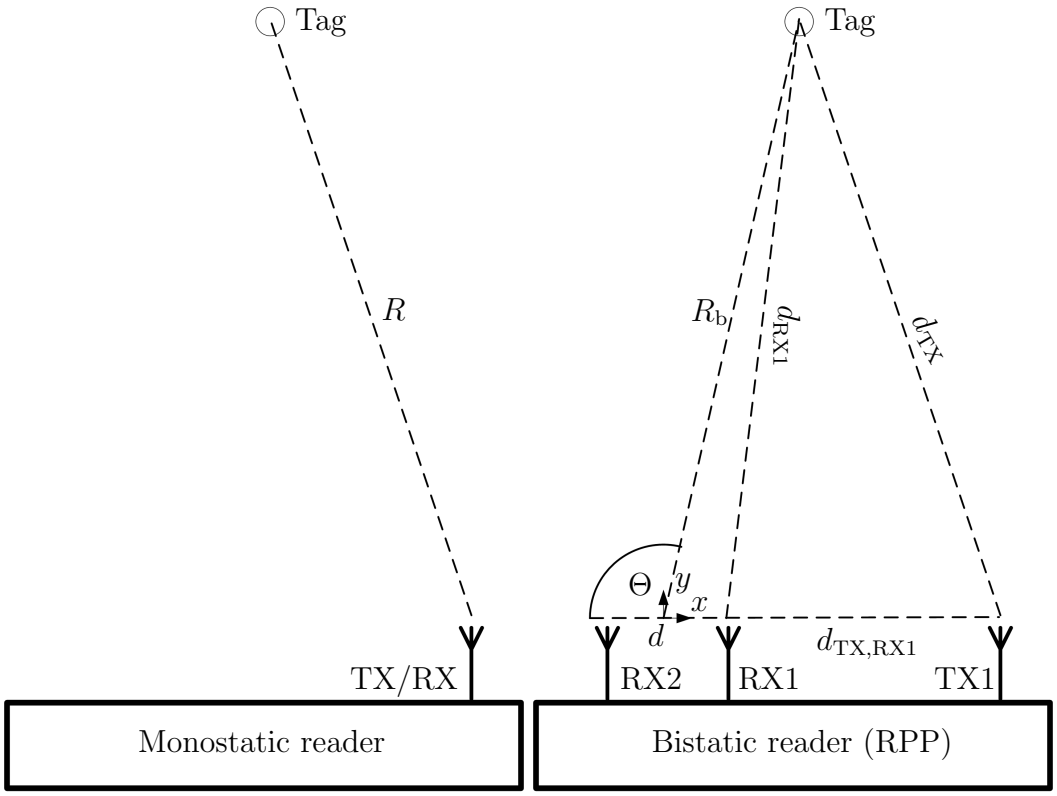

(a) Monostatic range estimation: R is the bisection of the distance TX-Tag-RX.

(b) Bistatic range estimation: R_b is distance between the origin and the tag.

Figure 3.6: Adaption for bistatic range estimation: The range R of a monostatic reader is estimated by the bisection of the distance TX-Tag-RX. The range R_b of a bistatic reader has to be adapted by considering the antenna configuration. R_b is calculated as a function of Θ and the monostatic range R.

R_{RX2}, respectively. The set of equations for the calculation of R_{RX1} is given by

$$d_{\mathrm{RX1}}^2 = R_{\mathrm{RX1}}^2 + \left(\frac{d}{2}\right)^2 - 2R_{\mathrm{RX1}}\frac{d}{2}\cos(\pi - \Theta), \tag{3.3}$$

$$d_{\mathrm{TX}}^2 = R_{\mathrm{RX1}}^2 + \left(d_{\mathrm{TX,RX1}} + \frac{d}{2}\right)^2 - 2R_{\mathrm{RX1}}\left(d_{\mathrm{TX,RX1}} + \frac{d}{2}\right)\cos(\pi - \Theta), \tag{3.4}$$

$$2R = d_{\mathrm{TX}} + d_{\mathrm{RX1}}, \tag{3.5}$$

where Θ is in Radians. The set of equations for the calculation of R_{RX2} is very similar and thus not explicitly stated. Also, the solution for R_{RX1} and R_{RX2} is very long and thus not stated.

Measurements

The range algorithm has also been implemented on the RPRP in order to test the performance of the algorithm. The measurement setup and measured positions are the same as for the DoA measurements, presented above. Moreover, the measurement data for the DoA and range estimation is the same. The range has been measured for both receiving antennas, RX1 and RX2 and is in the following again compared to the actual range values R_{act}, as can be seen in Fig. 3.7 and 3.8. R_{RX1} and R_{RX2} are calculated from the tag response at f_1 and f_2, giving a frequency difference of $\Delta f = f_2 - f_1 = 6$ MHz.
The maximum absolute range error of about 0.44 m can be observed for the position $(0, 0.75)$. The measurement point for R_{RX1} at the position $(-0.2, 1.75)$ has been excluded from Fig. 3.7. R_{RX1} has been estimated to about 7 m, which can clearly be excluded due the knowledge of the chamber dimensions.
The current setup of the RPRP does not allow a total calibration, because the range offset is not fully compensated by the calibration path, as explained above. Thus, the unknown range offset introduced by the RPRP has been calibrated out by means of the orthogonal measurement points. The offset has been chosen in a way that mean value of the respective eleven R_{RX1} and R_{RX2} values is the same as the mean value of the R_{act} values.
Ultimately, the adaptation towards the bistatic range estimation improved the performance by about 30%.

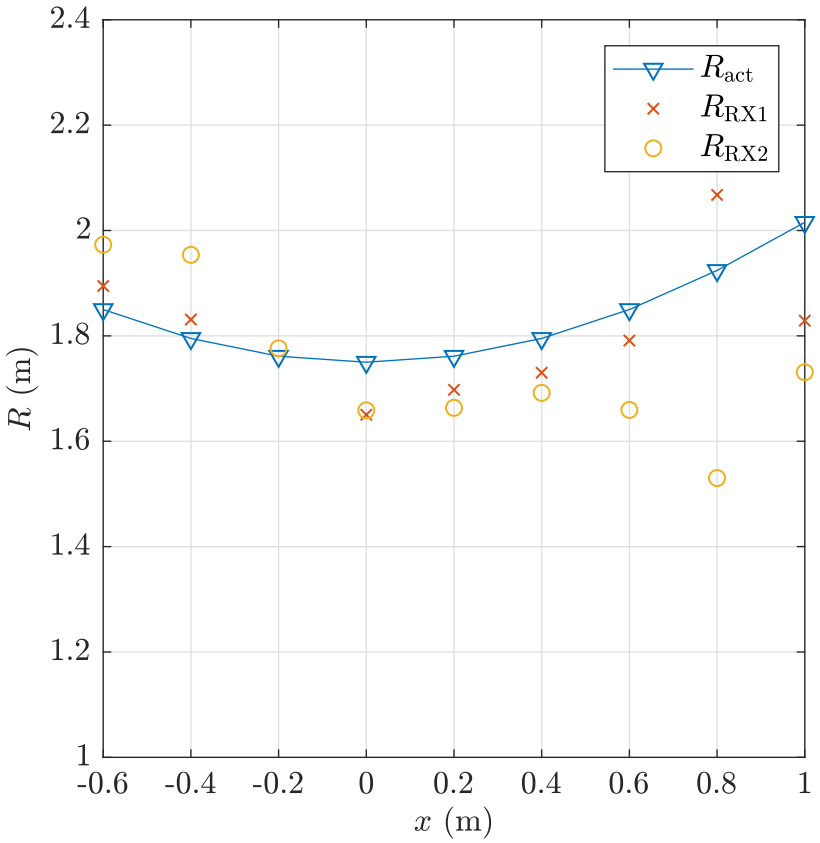

Figure 3.7: Range measurement in anechoic chamber 1: Range measurements of the parallel positions. Actual values are compared to the estimated values for both receive antennas RX1 and RX2. The frequency difference for the range estimation is $\Delta f = 6$ MHz. An outlier of R_{RX1} at the position $(-0.2, 1.75)$ has been excluded.

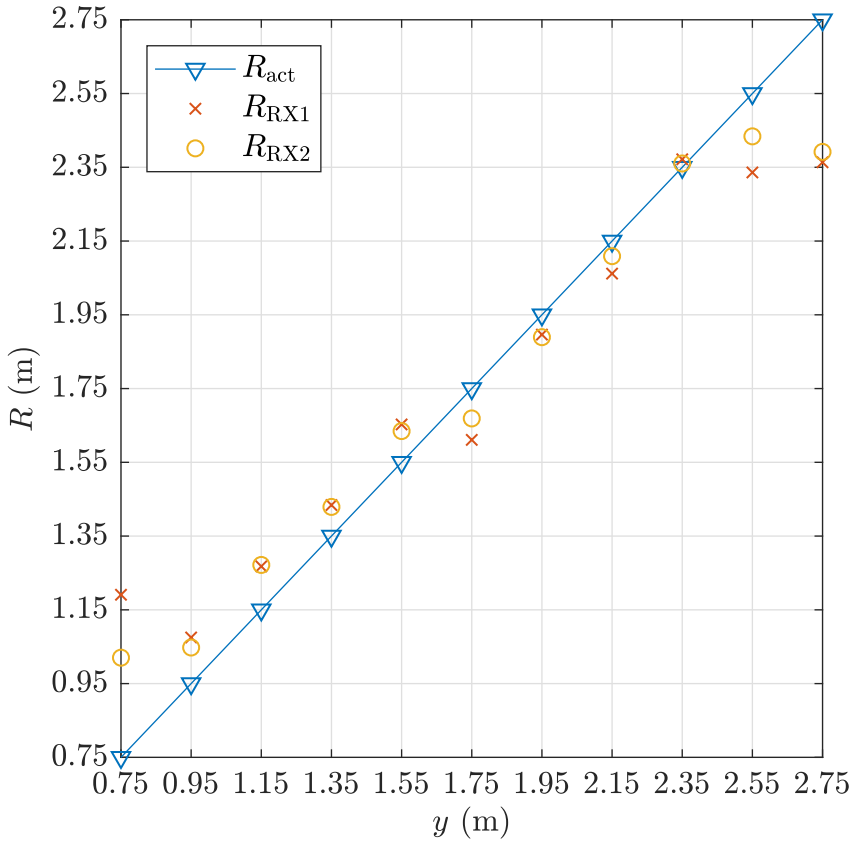

Figure 3.8: Range measurement in anechoic chamber 2: Range measurements of the orthogonal positions. Actual values are compared to the estimated values for both receive antennas RX1 and RX2. The frequency difference for the range estimation is $\Delta f = 6$ MHz. These measurements are used for the final system calibration.

3.1.3 2D Localization

As DoA and the range estimation could be implemented for the same bistatic reader setup, a combination to a 2D localization can be achieved. The x and y coordinates can be calculated with R_b and Θ in Radians to

$$x = R_b \cos(\pi - \Theta), \tag{3.6}$$
$$y = R_b \sin(\pi - \Theta). \tag{3.7}$$

Figure 3.9 compares the estimated positions P_{RX2} with the actual positions P_{act}. P_{RX1} is omitted in Fig. 3.9 due to visibility reasons. It can be seen that

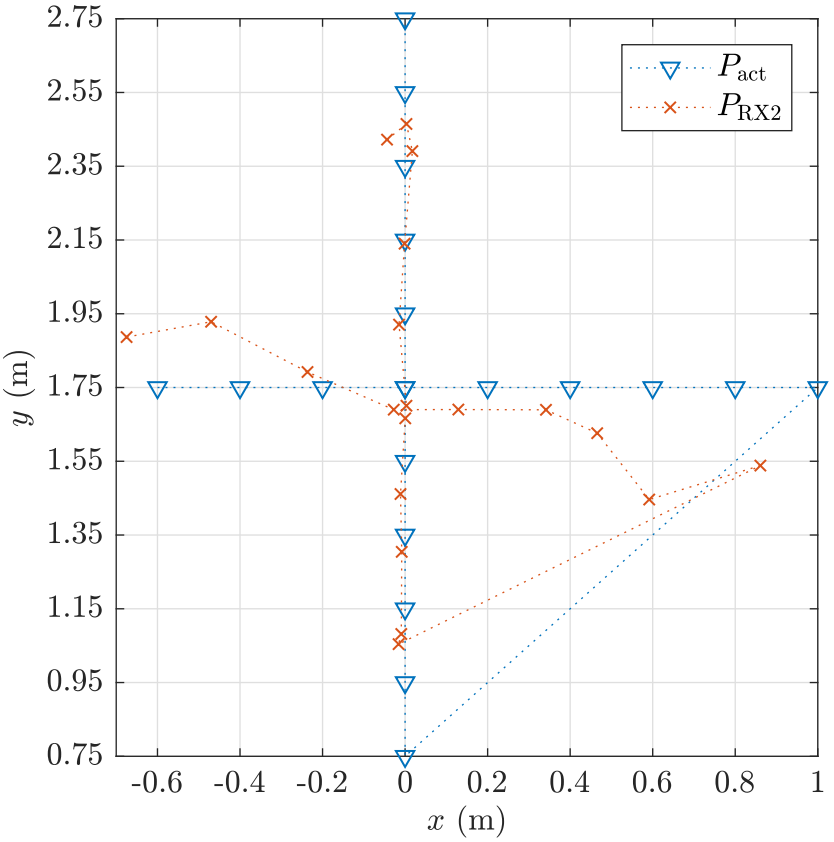

Figure 3.9: 2D position measurement in anechoic chamber: The positions P_{RX2} are calculated as a function of Θ and R_{RX2} and compared to the actual positions. The positions P_{RX1} are omitted due to visibility reasons.

the position errors are very high and that a large part is introduced by the range estimation.
It can be concluded that the 2D PDoA localization system might only be used in a meaningful way in environments with low multipath propagation. The deviation of the estimated positions to the actual positions are caused by several reasons. The anechoic chamber used for the measurements is not totally free of reflections, because of two fixed horn antennas within the chamber. Some errors are probably introduced by nonlinear effects of the used tag with respect to power and frequency [4]. Other errors might be introduced by the phase estimation of the reader receiver and by slightly misplaced tag positions. Finally, the effect of the mentioned errors on the range estimation is higher than on the DoA for room level localization. However, the influence of a deviation of the DoA on the absolute position increases with the distance between reader and tag (see Sec. 3.3).

3.2 Tracking System

The tracking system has been invented as a consequence of the moderate 2D PDoA localization system performance and is based on the TD-PDoA technique, as e.g., presented in [26]. Furthermore, the tracking system uses the same bistatic reader configuration as the localization system, providing the possibility to apply both systems simultaneously. In the following, the tracking algorithm is presented and the performance is shown by means of measurements in the anechoic chamber and a laboratory multipath environment.

3.2.1 Algorithm

The tracking algorithm is in the following explained by means of Fig. 3.10. Figure 3.10a shows the top view of the tracking system in Cartesian coordinates with a tag at tag position 1 (black circle). The x and y coordinates of tag position 1 are assumed to be known. This starting position might either be estimated or be defined by the application. A z coordinate cannot be estimated by the 2D tracking system. The distances between the reader antennas are $d_{\mathrm{TX,RX1}}$ and $d_{\mathrm{TX,RX2}}$, respectively.

As can be seen in Fig. 3.10b, with the knowledge of tag position 1, a circumference $C_{\mathrm{RX1,prior}}$ can be calculated that consist of the side lengths $d_{\mathrm{TX,RX1}}$, $d_{\mathrm{RX1,prior}}$ and $d_{\mathrm{TX,prior}}$. If the backscattered tag signal is received at RX1 and RX2, the phases of the tag signal $\varphi_{h,\mathrm{RX1,prior}}$ and $\varphi_{h,\mathrm{RX2,prior}}$ are stored at the reader (RPRP).
Figure 3.10c shows the scenario when the tag position has changed to tag position 2. The circumference of the new conducted triangle is C_{RX1} that consist of $d_{\mathrm{TX,RX1}}$, d_{RX1} and d_{TX}. C_{RX1} can be calculated from the old circumference $C_{\mathrm{RX1,prior}}$ by

$$C_{\mathrm{RX1}} = C_{\mathrm{RX1,prior}} + \Delta d_{\mathrm{RX1}} + \Delta d_{\mathrm{TX}}, \tag{3.8}$$

where Δd_{RX1} and Δd_{TX} are the changes of the side lengths from RX1 to the tag and TX to the tag, respectively. At position 2, the tag signal phases $\varphi_{h,\mathrm{RX1}}$ and $\varphi_{h,\mathrm{RX2}}$ are recorded and the phase difference at RX1 is calculated to $\Delta\varphi_{h,\mathrm{RX1}} = \varphi_{h,\mathrm{RX1}} - \varphi_{h,\mathrm{RX1,prior}}$. By means of the TD-PDoA technique, $\Delta\varphi_{h,\mathrm{RX1}}$ can be related to the sum of Δd_{RX1} and Δd_{TX} by

$$\Delta d_{\mathrm{RX1}} + \Delta d_{\mathrm{TX}} = -\frac{c}{2\pi f}\Delta\varphi_{h,\mathrm{RX1}}. \tag{3.9}$$

The position change is again restricted by the periodicity of the signal phase and only changes of $|\Delta d_{\mathrm{RX1}} + \Delta d_{\mathrm{TX}}| < \frac{c}{2f}$ are allowed.
The same procedure can be examined for RX2, as shown in Fig 3.10d, with the phase difference $\Delta\varphi_{h,\mathrm{RX2}} = \varphi_{h,\mathrm{RX2}} - \varphi_{h,\mathrm{RX2,prior}}$ and the circumference can be calculated to

$$C_{\mathrm{RX2}} = C_{\mathrm{RX2,prior}} + \Delta d_{\mathrm{RX2}} + \Delta d_{\mathrm{TX}}. \tag{3.10}$$

So far, the circumferences C_{RX1} and C_{RX2} of the triangles conducted by TX, tag position 2, RX1 and TX, tag position 2, RX2 can be estimated, respectively. Additionally, it can be seen in Fig. 3.10e that the triangles share the side length d_{TX} and the angle β. With the mentioned knowledge, the following set of three equations can be set up:

$$\cos\beta = \frac{d_{\mathrm{RX1}}^2 - d_{\mathrm{TX,RX1}}^2 - d_{\mathrm{TX}}^2}{2d_{\mathrm{TX,RX1}}d_{\mathrm{TX}}} = \frac{d_{\mathrm{RX2}}^2 - d_{\mathrm{TX,RX2}}^2 - d_{\mathrm{TX}}^2}{2d_{\mathrm{TX,RX2}}d_{\mathrm{TX}}}, \tag{3.11}$$

$$d_{\mathrm{RX1}} = d_{\mathrm{RX2}} + C_{\mathrm{RX1}} - C_{\mathrm{RX2}} + d_{\mathrm{TX,RX2}} - d_{\mathrm{TX,RX1}}, \tag{3.12}$$

$$d_{\mathrm{TX}} = C_{\mathrm{RX2}} - d_{\mathrm{RX2}} - d_{\mathrm{TX,RX2}}, \tag{3.13}$$

with three remaining unknown variables d_{RX1}, d_{RX2} and d_{TX}. From this set of equations the side length d_{RX2} can be calculated to

$$d_{\mathrm{RX2}} = \frac{1}{2}\Bigg(\frac{d_{\mathrm{TX,RX1}}C_{\mathrm{RX2}}^2 + d_{\mathrm{TX,RX2}}C_{\mathrm{RX1}}^2 - 2d_{\mathrm{TX,RX2}}C_{\mathrm{RX1}}C_{\mathrm{RX2}}}{d_{\mathrm{TX,RX1}}C_{\mathrm{RX2}} - d_{\mathrm{TX,RX2}}C_{\mathrm{RX1}}}$$

$$+ \frac{2d_{\mathrm{TX,RX2}}^2 C_{\mathrm{RX1}} - 2d_{\mathrm{TX,RX1}}d_{\mathrm{TX,RX2}}C_{\mathrm{RX1}}}{d_{\mathrm{TX,RX1}}C_{\mathrm{RX2}} - d_{\mathrm{TX,RX2}}C_{\mathrm{RX1}}}\Bigg). \tag{3.14}$$

The remaining two variables d_{RX1} and d_{TX} can be calculated by Eqs. 3.12 and 3.13, respectively. Finally, the 2D coordinates of the current tag position can be calculated by

$$x = \frac{d_{\mathrm{TX,RX1}} + d_{\mathrm{TX,RX2}}}{2} - d_{\mathrm{TX}}\cos\beta, \tag{3.15}$$

$$y = d_{\mathrm{TX}}\sin\beta. \tag{3.16}$$

It can also be seen that a position update is provided within only one communication cycle, which allows the tracking of fast moving tags.

3.2.2 Measurements

The tag tracking algorithm has been implemented on the RPRP to evaluate the performance of the tag tracking system. A first measurement campaign has been conducted in the anechoic chamber, where the setup can be seen in Fig. 3.11. The horizontal reader antenna spacing is $d_{\mathrm{TX,RX1}} = 0.52$ m and $d_{\mathrm{TX,RX2}} = 0.8$ m and the tag has been positioned in 50 mm steps clockwise on a rectangular styrofoam carrier. Figure 3.12 compares the actual tag positions P_{act} with the estimated tag positions P_{track}. The starting position of the algorithm has been set to the actual starting position in the right down corner $(0.65\ \mathrm{m}, 1.42\ \mathrm{m})$. The maximum absolute position error reached in the chamber is about 0.08 m at $(0.65\ \mathrm{m}, 1.77\ \mathrm{m})$, which is much less compared to the 2D localization system. It can also be seen that the bulk of the absolute position error is introduced by the x-component, while the y-component stays very close to the actual value. This behavior can be explained by the geometry of the system and the calculation of the coordinates according to Eqs. 3.15 and 3.16. The reached

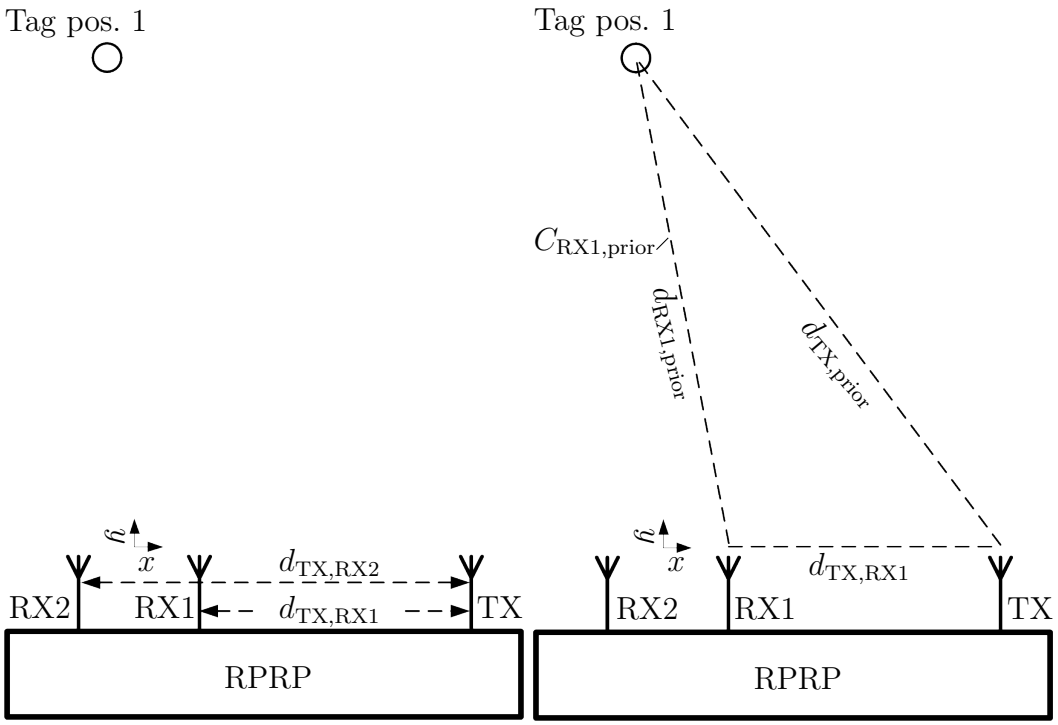
Tag pos. 1
y
x
RX2
RX1
TX
$d_{\mathrm{TX,RX2}}$
$d_{\mathrm{TX,RX1}}$
RPRP
(a)
Tag pos. 1
$C_{\mathrm{RX1,prior}}$
$d_{\mathrm{RX1,prior}}$
$d_{\mathrm{TX,prior}}$
y
x
$d_{\mathrm{TX,RX1}}$
RX2
RX1
TX
RPRP
(b)

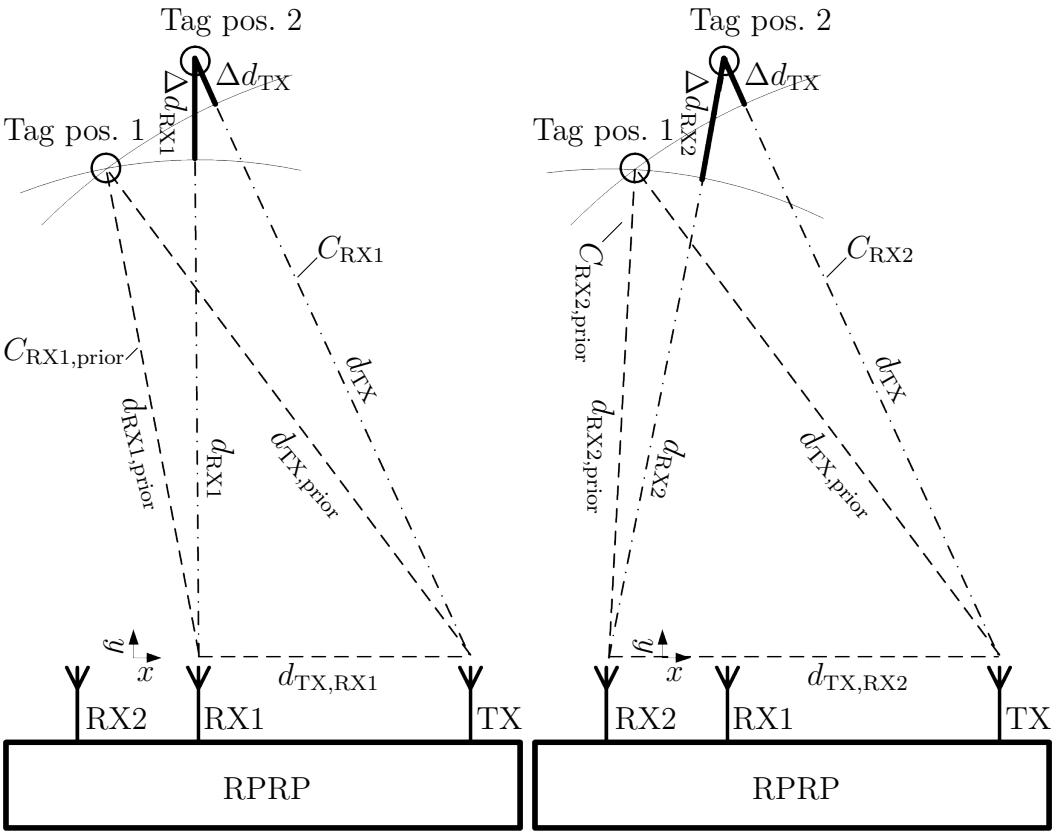
Tag pos. 2
Tag pos. 1
Δd_{RX1}
Δd_{TX}
C_{RX1}
$C_{\mathrm{RX1,prior}}$
d_{TX}
$d_{\mathrm{RX1,prior}}$
d_{RX1}
$d_{\mathrm{TX,prior}}$
y
x
$d_{\mathrm{TX,RX1}}$
RX2
RX1
TX
RPRP
(c)
Tag pos. 2
Tag pos. 1
Δd_{RX2}
Δd_{TX}
C_{RX2}
$C_{\mathrm{RX2,prior}}$
d_{TX}
$d_{\mathrm{RX2,prior}}$
d_{RX2}
$d_{\mathrm{TX,prior}}$
y
x
$d_{\mathrm{TX,RX2}}$
RX2
RX1
TX
RPRP
(d)

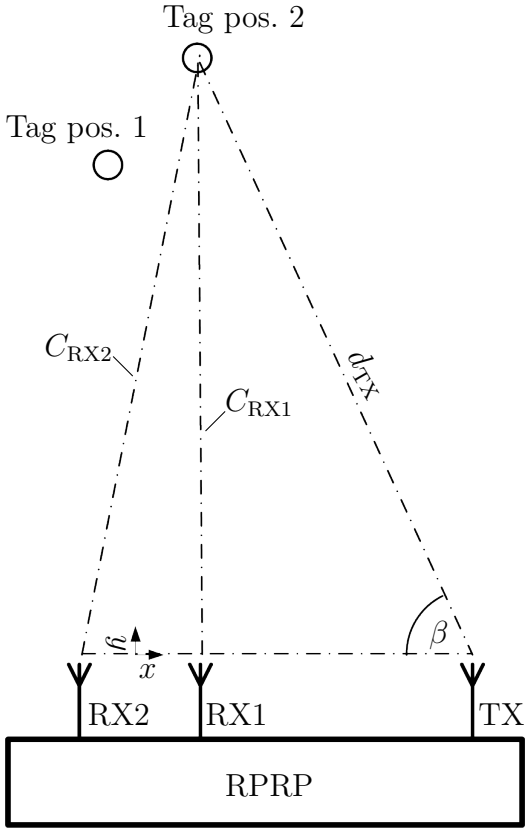

(e)

Figure 3.10: Tracking algorithm: The tracking algorithm is explained by means of figures (a) to (e).

values of β in this measurement setup are between about 65° and 90°. In this region, errors of β influence the cos-function more than the sin-function and thus the x coordinate more than the y coordinate. Also, the influence of errors on the estimated position increases with increasing distance between reader and tag, which is again caused by the triangular geometry.
Three more observations can be made when looking at Fig. 3.12. First, the estimated rectangle seems to be slightly tilted compared to the actual rectangle. This can be explained by slight deviations of the assumed geometry to the actual geometry of the measurement setup, as e.g., slight deviations of the distance between reader antennas or the deviations of the assumed actual positions from the true ones, etc. Second, the trend of the deviation of P_{track} to P_{act} in regions with constant x coordinates (right and left side of the rectangle), might conclude the presence of multipath components in this regions. This multipath components are most probably introduced by the horn antenna that can be seen in Fig. 3.11 at the ceiling of the anechoic chamber. Third, the track does not end at the starting position, but is extended to the former first 5 positions. The first 5 positions and the last 5 positions cover each other very well, which shows that the introduced errors are not accumulated from position to position.
As already mentioned above, the setup for the 2D tracking system and the 2D localization system is the same. Furthermore, the tag direction calculated from the current position of the tracking system is closely related to the DoA estimated by the localization system, which arises from the system geometry. Without a further explanation, both algorithms incorporate the current tag signal phases $\varphi_{h,\text{RX1}}$ and $\varphi_{h,\text{RX2}}$. For a correct chosen starting position of the tracking algorithm, the current position lies very close to the DoA line. Only very close is due to the fact that the DoA is only an approximation for finite distances between reader and tag. However, this relation relaxes the problem of finding the starting position, as the latter is at least limited to be on the DoA line. Furthermore, the DoA can recognize possible tracking errors, if the directions of the estimates diverge.
The full 2D localization system, including DoA and range estimation might also be used as a rough estimation for the starting position of the tracking system. Additional knowledge about the application, e.g. impossible positions within a room, might then be used to recalculate the former starting position and thus to enhance the accuracy of the current position, i.e., learning over time.

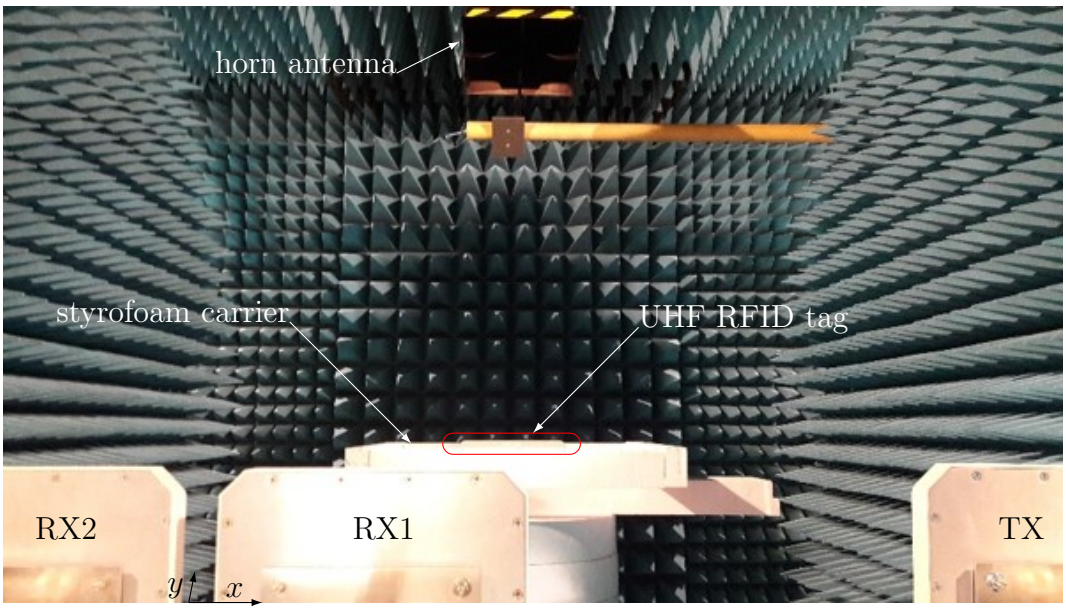

Figure 3.11: Tag tracking in anechoic chamber: The reader antenna spacing is $d_{\mathrm{TX,RX1}} = 0.52$ m and $d_{\mathrm{TX,RX2}} = 0.8$ m. The tag has been positioned in 50 mm steps clockwise on a rectangular styrofoam carrier. The horn antenna is a reflector and causes multipath propagation in the chamber.

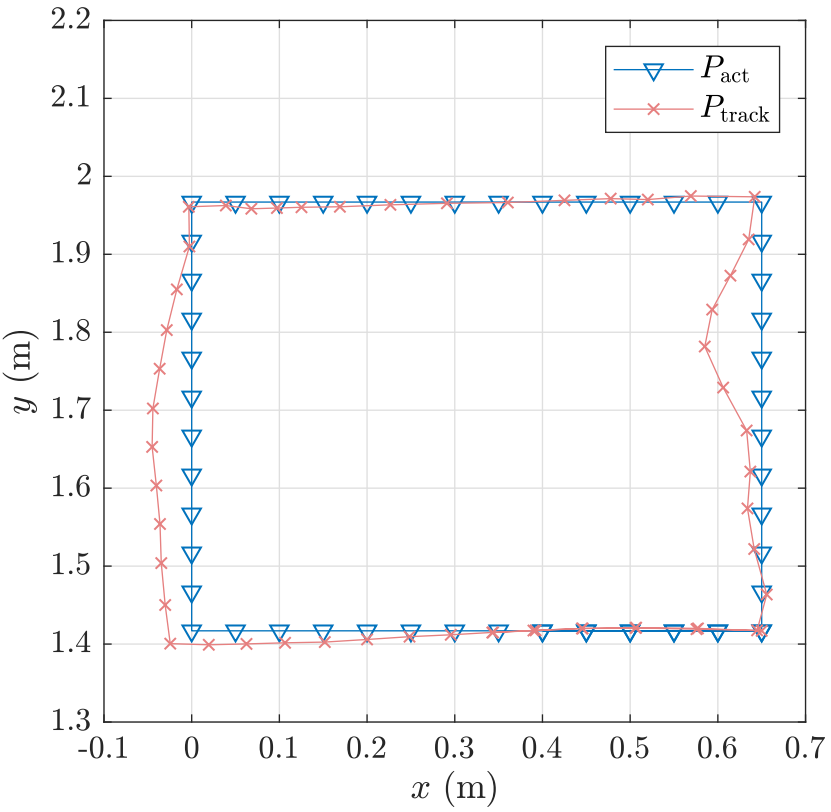

Figure 3.12: 2D tracking in anechoic chamber: The estimated tag positions P_{track} are compared to the actual tag positions P_{act}. The starting position of the algorithm has been set to the actual starting position in the right down corner at $(0.65\text{ m}, 1.42\text{ m})$.

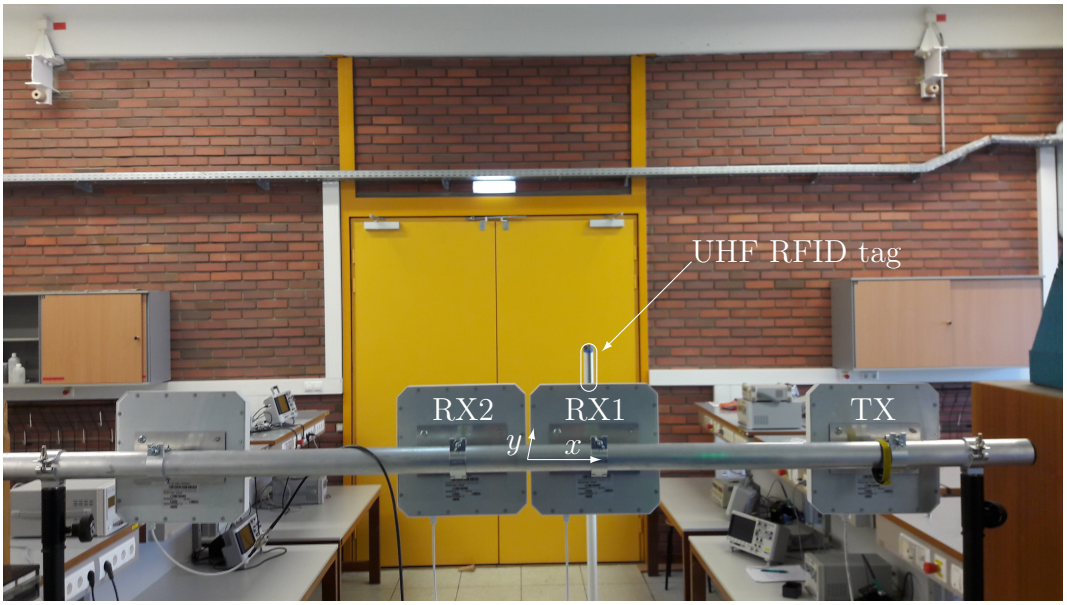

Figure 3.13: Tag tracking in the laboratory: The reader antenna spacing is $d_{\mathrm{TX,RX1}} = 0.52$ m and $d_{\mathrm{TX,RX2}} = 0.8$ m. The tag has been positioned in 100 mm steps clockwise on a rectangular path. Many reflections can be expected by the bottom, the ceiling, the door in the back and other smaller reflectors.

The second measurement campaign has been conducted in a laboratory environment as can be seen in Fig. 3.13. Strong multipath components can be expected in such an environment, e.g. from reflections at the ground, the ceiling and the door at the back of the environment. The tag has been moved on a rectangular track as can be seen in Fig 3.14 with the actual positions P_{act}. The starting position of the algorithm has been set to the actual starting position in the right down corner $(0.5\ \mathrm{m}, 1\ \mathrm{m})$. The maximum absolute position error reached in the laboratory is about 0.33 m at $(0.5\ \mathrm{m}, 2.20\ \mathrm{m})$, which is still less than the absolute position error of the 2D localization system in the anechoic chamber. As already observed for the anechoic chamber measurements, the deviation of the x coordinate is dominant. At larger distances, the error is larger than for lower distances. This can be explained by the geometry mentioned above and by the lower tag signal power, which makes the detection more difficult. Furthermore, the multipath components seem to be lower until a distance of about $y = 1.5$ m.

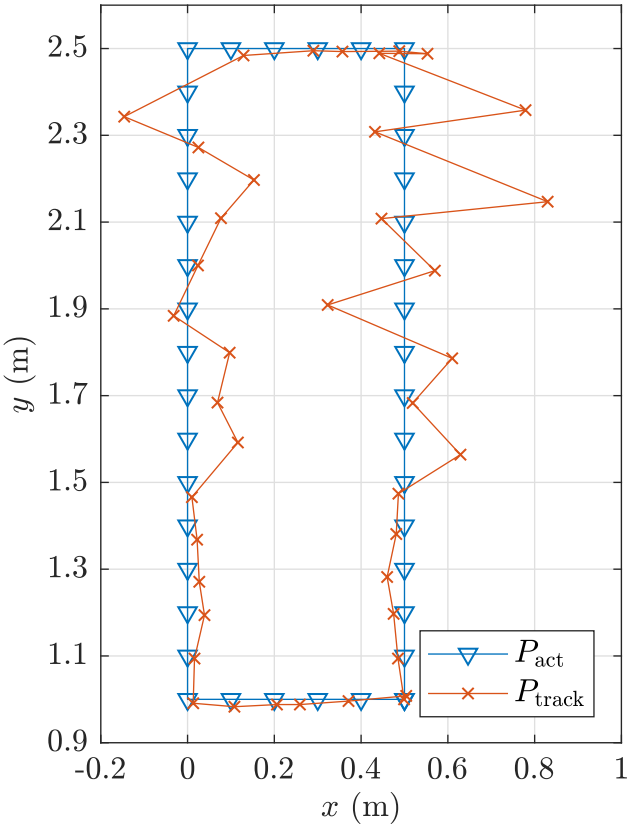

Figure 3.14: 2D tracking in the laboratory: The estimated tag positions P_{track} are compared to the actual tag positions P_{act}. The starting position of the algorithm has been set to the actual starting position in the right down corner at $(0.5\ \text{m}, 1\ \text{m})$. The errors become larger with increasing distance. The errors in x direction dominate.

3.3 Performance Analysis

This section theoretically investigates the performance of the tracking system in the presence of multipath propagation with a simple thought experiment. For this investigation, a room with dimensions comparable to the room presented in Fig. 2.1 is assumed. For the antenna setup, $d_{\mathrm{TX,RX1}} = 0.6$ m and $d_{\mathrm{TX,RX2}} = 0.9$ m is assumed. In general, the presence of multipath components leads to an error in the detected tag signal phase. This error is assumed to be 1° in this experiment. A faulty position is simply calculated from the actual one by using the tracking algorithm and $\Delta\varphi_{h,\mathrm{RX1}} = 1°$ and $\Delta\varphi_{h,\mathrm{RX2}} = -1°$ as error. For example, the error in case of $\Delta\varphi_{h,\mathrm{RX1}} = \Delta\varphi_{h,\mathrm{RX2}} = 1°$ would be much lower.
Figure 3.15 shows a contour plot that indicates the absolute deviation between the actual and the faulty positions within the room. It can be seen that the influence of the tag phase error on the position increases with the distance between the tag and the reader, which is caused by the geometry of the tracking system. It can be seen that at a distance of about 7 m, the error is about 45 mm. In case of $\Delta\varphi_{h,\mathrm{RX1}} = 10°$ and $\Delta\varphi_{h,\mathrm{RX2}} = -10°$, the error at 7 m would be about 0.45 m, which may still be acceptable for some applications.
Similar investigations are presented for the 2D localization system, in order to make a theoretical comparison between the two systems. The faulty DoA has been calculated based on the actual one by an phase offset of 1° with contrary sign for both phases detected at RX1 and RX2, respectively. This gives an error of the estimated $\Delta\varphi_{\mathrm{D}}$ of 2°. Figure 3.16 shows the deviation of the actual to the estimated DoA within the room. As the $\cos(x)$-function is a nonlinear function, the deviation of the DoA depends on the tag position and gets larger towards the sides of the room. It can also be observed that a deviation of the DoA has more impact on the absolute tag position with increasing distance. Imagine two tags with the same x-coordinate but a different y-coordinate, e.g., $(0, 2)$ and $(0, 7)$. If the error of the DoA was the same for both positions, then the deviation of the x-coordinate at $y = 7$ m would be much larger than at $y = 2$ m.
For simplicity, the investigations about the range estimation are performed assuming a monostatic system. Assuming again a frequency difference of $\Delta f =$ 6 MHz, and a error of $\Delta\varphi_{\mathrm{R}}$ of 2°, then the error of the range would be about 139 mm, independent of the tag position. As can be seen in Eqn. 3.2, the error influences the range in a linear way.

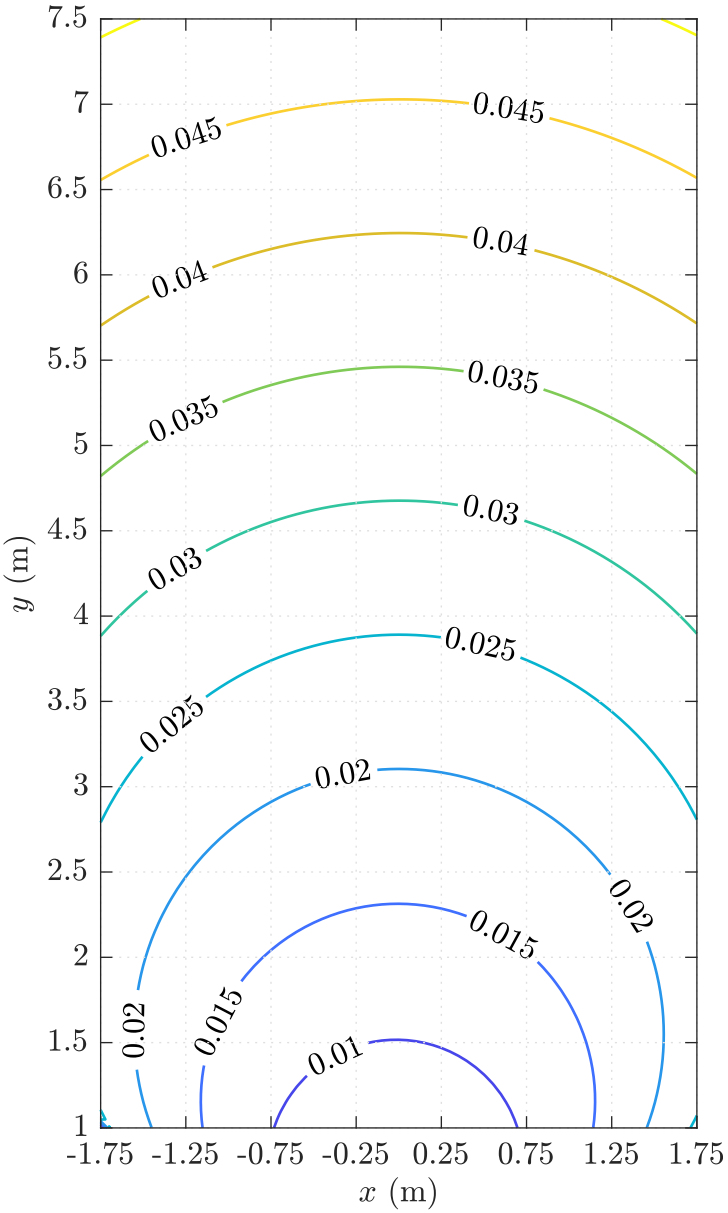

Figure 3.15: Influence of multipath on tag tracking: The theoretical deviation in meters of the estimated absolute position from the actual position is indicated by contour lines. Phase errors of $\Delta\varphi_{h,\mathrm{RX1}} = 1°$ and $\Delta\varphi_{h,\mathrm{RX2}} = -1°$ are introduced. The errors increase with the distance of the tag.

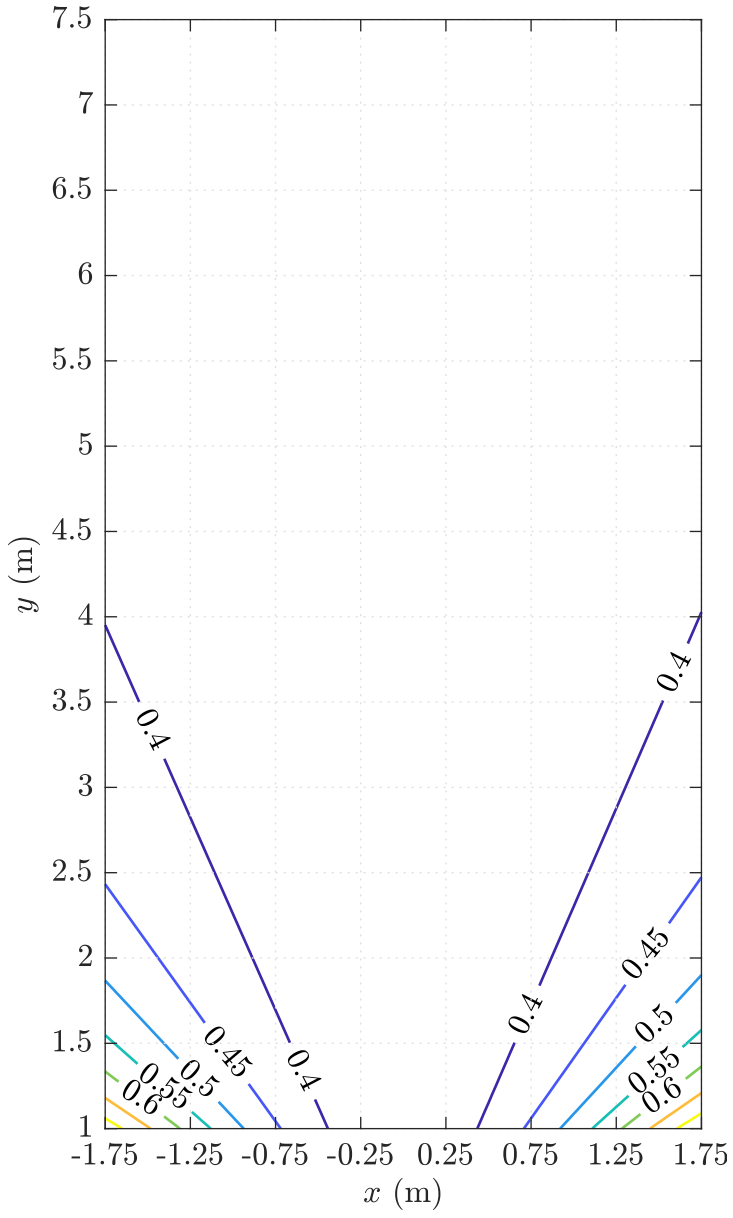

Figure 3.16: Influence of multipath on DoA estimation: Influence of multipath propagation on tag tracking: The theoretical deviation in degrees of the estimated DoA from the actual DoA is indicated by contour lines. Phase errors of 1° and −1° are introduced for RX1 and RX2, respectively. DoA errors get larger towards the sides of the room and have more impact on the absolute position error at higher distances.

Figure 3.17 now show the overall theoretical performance of the 2D localization system in this exemplary room. It can be seen that the deviation of the estimated position to the actual one is mainly caused by the error of the range. It can also be seen that the deviation does not change much with the tag position within the room and is around 143 mm.
The maximum absolute theoretical position error of the tracking system within the room is about three times lower compared to the localization system. For lower distances, the performance difference gets more significant and increases to a factor of about 10 for distances around 2 m.
Finally, I also investigated the influence of a z offset, i.e., a difference of reader antenna height and tag height on the 2D tracking and localization systems, which results in a position error. Figure 3.18 shows the introduced position error in the room in meters in case of an exemplary 200 mm z offset. As can be seen in Fig. 3.18a, the error on tag tracking positions increases with increasing tag to reader distances and reaches a maximum of about 35 mm at $x = 1.75$ m and $y = 7.5$ m. Figure 3.18b shows the error introduced by a z offset on DoA estimation, which is mostly negligible and slightly increases towards the right and left sides of the room. Figure 3.18c shows that the introduced error on range estimation decreases with increasing tag to reader distances. In summary it can be said, that the highest influence of z offsets can be seen in case of tag tracking. However, a z offset in the range of about 200 mm can almost be neglected in multipath environments, where typically phase deviations above 2° can be expected. The introduced errors increase with increasing z offsets, which has to be considered in the application.

3.4 Summary

This chapter presents a novel 2D tracking system based on a SIMO antenna configuration. One TX and two RX antennas are horizontally separated with certain distances to each other at the same height, facing in the same direction. The specific antenna setup allows an estimation of a position update based on geometrical system properties and tag signal phase measurements.
The chapter shows that a localization system based on SD-PDoA and FD-PDoA is only limited useful in typical application environments due to multipath

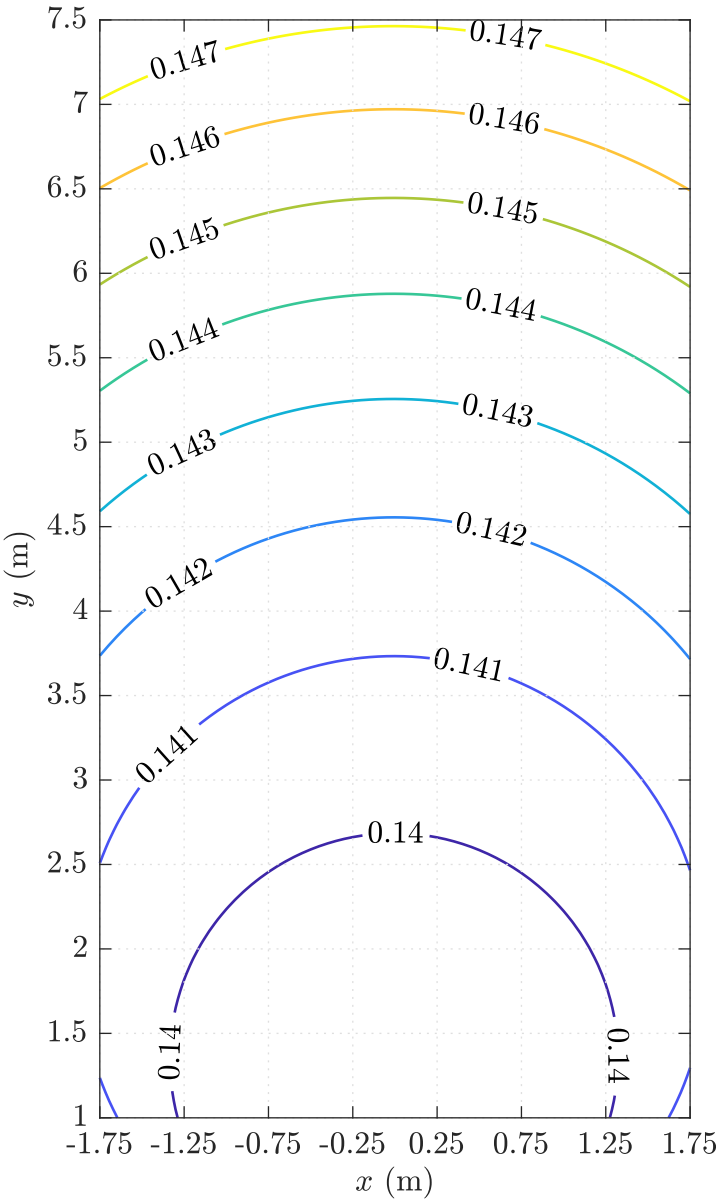

Figure 3.17: Influence of multipath on the localization system: The theoretical deviation in meters of the estimated absolute position from the actual position is indicated by contour lines. An additional error of $\Delta\varphi_{\mathrm{R}} = 2°$ is introduced for the range estimation. The deviations of the estimated absolute positions are mainly introduced by the faulty range estimation. Compared to the tracking algorithm, the maximum absolute position error is about three times higher.

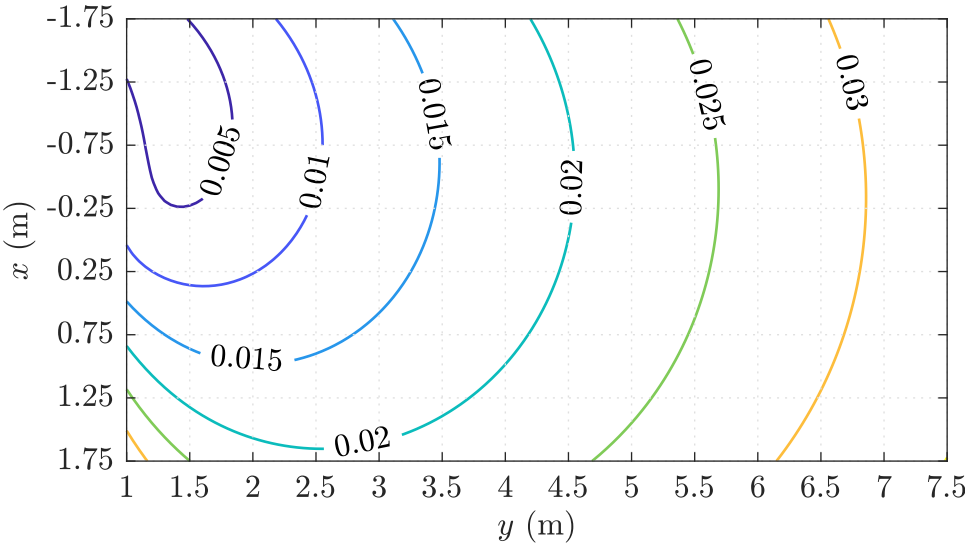

(a) Influence of z offset on tag tracking: The error increases with increasing tag to reader distance. The maximum error of about 35 mm can be seen at $x = 1.75$ m and $y = 7.5$ m. The starting position is at $x = -1.75$ m and $y = 1$ m.

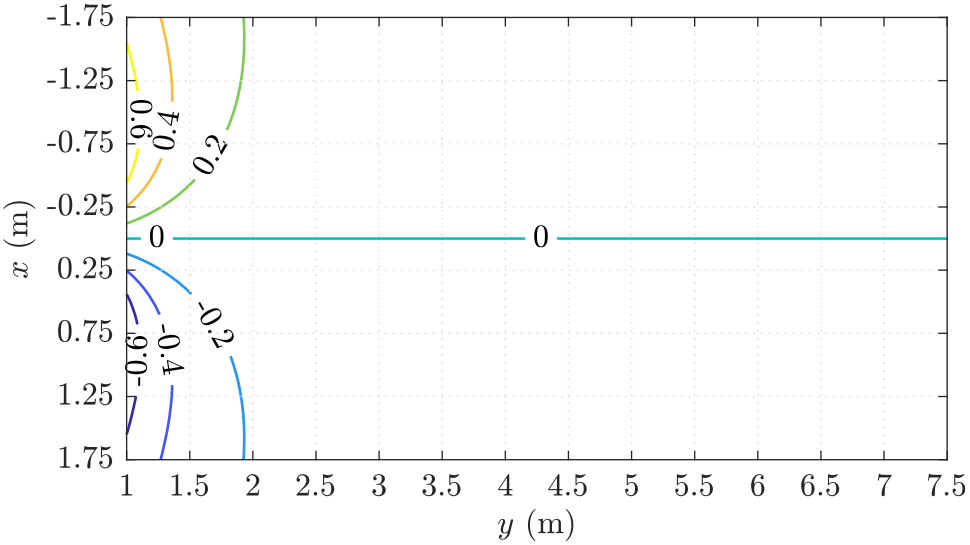

(b) Influence of z offset on DoA estimation: The error increases towards the left and right sides of the room and is below 0.75°. A z offset does not have an influence on the DoA for $x = 0$ m regions.

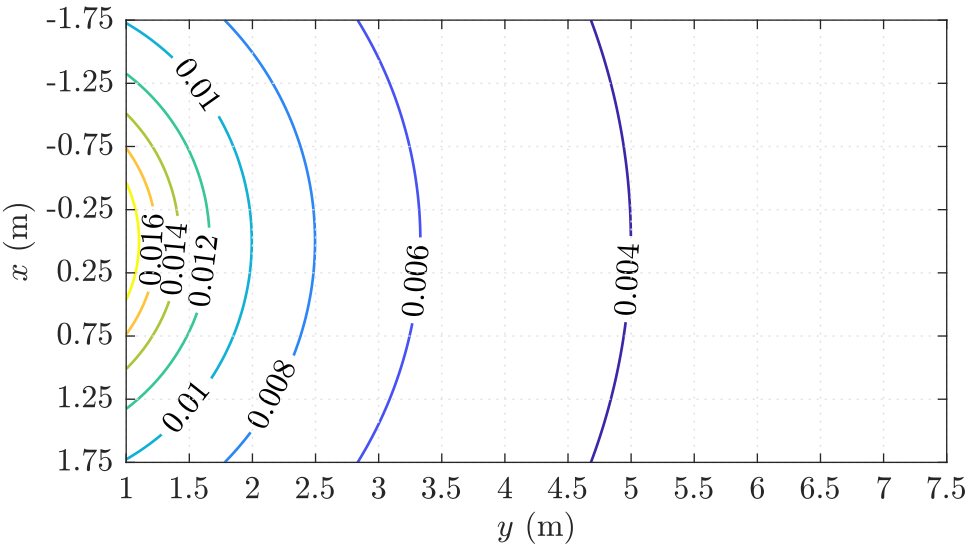

(c) Influence of z offset on range estimation: The error decreases with increasing tag to reader distance and is below 20 mm.

Figure 3.18: Influence of z offset on the 2D tracking and localization systems: The tag is assumed to be 200 mm higher (z offset) than the reader antennas. The introduced errors on tag tracking (3.18a) and range estimation (3.18c) are plotted in meters, while the introduced errors on DoA estimation (3.18b) are plotted in degrees.

propagation. The presented tracking system is based on the more robust TD-PDoA technique, making the system applicable for the use in harsh application environments. Measurements and theoretical investigations show that the tracking system is robust in multipath propagation environments for room level dimensions. Furthermore, the tracking system provides the position update within only one communication cycle between the reader and the tag and is thus suitable for the tracking of fast changing tag positions. Another feature of the novel system is the possibility to follow tags on arbitrary 2D tracks.

4 Sensor System

This chapter presents a novel sensor system that is based on the detection of defined tag signal patterns at the reader receiver. Due to the detection of defined patterns, there is no need for a system calibration and thus a distance[1] independent remote monitoring is possible. The UHF RFID sensor tag consists of a state-of-the-art chip and a sensor antenna, where special attention is paid to ensure a stable communication between the reader and the sensor tag.
Section 4.1 presents the sensing concept of the sensing system, while starting with a general description of a sensor antenna. Section 4.2 presents the design, simulations and measurements of a sensor tag prototype for water filling level sensing.

Original Publications Related to this Chapter

J. Grosinger, L. Görtschacher, and W. Bösch, "Sensor Add-On for Batteryless UHF RFID Tags Enabling a Low Cost IoT Infrastructure." In: *Proc. IEEE MTT-S International Microwave Symposium (IMS)*, 2016.

J. Grosinger, L. Görtschacher, and W. Bösch, "Passive RFID Sensor Tag Concept and Prototype Exploiting a Full Control of Amplitude and Phase of the Tag Signal." In: *IEEE Transactions on Microwave Theory and Techniques*, 2016.

F. Berra, A. Costanzo, J. Grosinger, and L. Görtschacher "Space mapping design method for an antenna transducer of a bend sensor RFID tag." In: *Proc. IEEE 47th European Microwave Conference (EuMC)*, 2017.

[1] distance between reader and tag

L. Görtschacher, W. Bösch, and J. Grosinger, "UHF RFID Sensor Tag Antenna Concept for Stable and Distance Independent Remote Monitoring." In: *Proc. IEEE International Microwave Biomedical Conference (IMBioC)*, 2018.

4.1 Sensing Concept

This section presents the sensing concept that overcomes two main problems in case of sensing based on sensor antennas. The first problem is that a sensor system might require an individual calibration for each system setup as, e.g., for different distances between reader and sensor tag. The second problem is that the sensing state can influence the power transfer to the passive chip and the power of the backscattered tag signal and thus decrease communication stability. The presented concept does not need an individual calibration for different reader/tag distances and ensures a stable communication during the whole sensing process. These two ideas are not independent to each other, which has to be considered in the design process.
The following subsection presents a general description of sensor antennas and an application example, while the two basic ideas of the concept are presented in the two subsequent subsections.

4.1.1 Sensor Antenna

The idea of a sensor antenna is to exploit the interaction of an antenna with its environment in order to extract parameters of the latter. One application example could be the sensing of the filling level ψ of infusion bags in hospital rooms. Fig. 4.1 depicts the mentioned application example, where the sensor tag, consisting of the sensor antenna, the chip and the substrate, is attached at the outside of an infusion bag. The reader communicates by means of the reader antenna with the sensor tag during the whole sensing cycle. A sensing cycle is defined as a successive change of the sensing state ψ, within the whole sensing range from ψ_{Start} (infusion bag is full) to ψ_{Stop} (infusion bag is empty). The hospital staff might then be informed, when the infusion bag is almost empty.
During the sensing process, the tag signal gets modulated in amplitude and

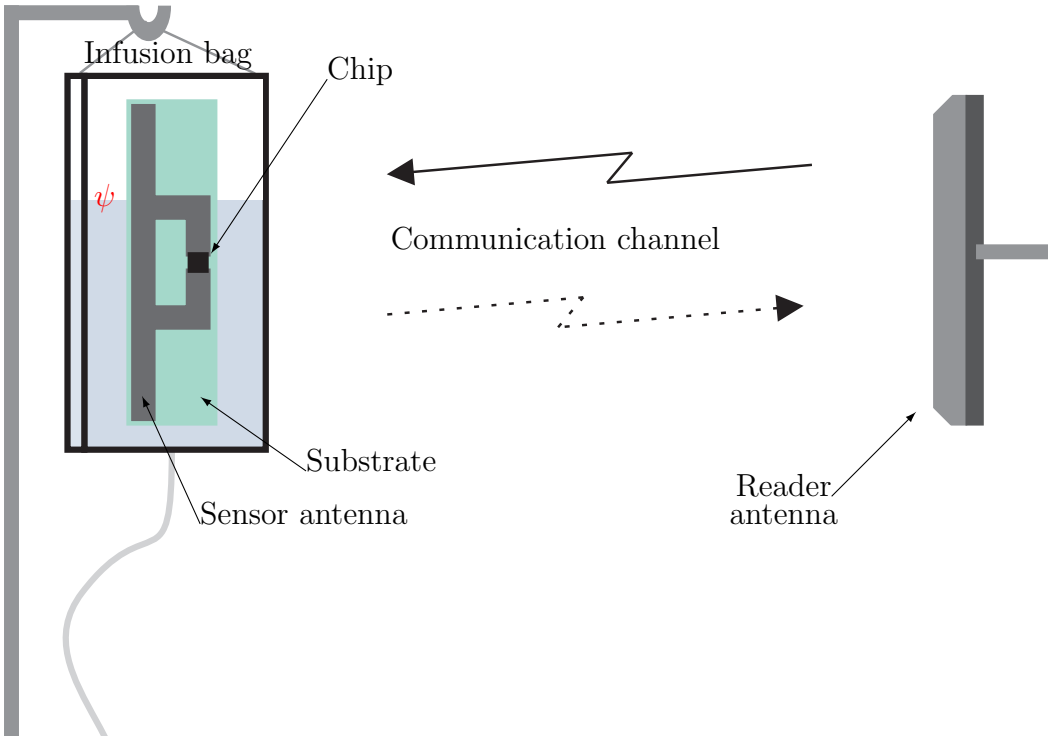

Figure 4.1: Sensing application example: The sensor tag, consisting of the sensor antenna, the chip and the substrate, is mounted vertically on an infusion bag. The reader communicates with sensor tag via the reader antenna. Amplitude and phase of the backscattered tag signal can be related to the filling level ψ, allowing a remote monitoring.

phase, additionally to the classical modulation (tag ID transfer), as described in Sec. 1.1. The next challenge of a sensor system is to correctly relate the received tag signal $h(\psi)$ to the sensing state ψ. One reason for the mentioned additional amplitude and phase modulation is that the antenna input impedance depends on the sensing state. This means that Z_{Ant} gets to $Z_{\mathrm{Ant}}(\psi)$, referring to the classical tag equivalent circuit in Fig. 1.3. Subsequently, also the reflection

coefficients in the corresponding modes depend on ψ and can be written as

$$S_{\mathrm{Abs}}(\psi) = \frac{Z_{\mathrm{Abs}} - Z_{\mathrm{Ant}}(\psi)^*}{Z_{\mathrm{Abs}} + Z_{\mathrm{Ant}}(\psi)} \text{ and} \tag{4.1}$$

$$S_{\mathrm{Ref}}(\psi) = \frac{Z_{\mathrm{Ref}} - Z_{\mathrm{Ant}}(\psi)^*}{Z_{\mathrm{Ref}} + Z_{\mathrm{Ant}}(\psi)}. \tag{4.2}$$

Finally Eqs. 1.12 and 1.13 can be rewritten to

$$|h(\psi)| = |s_{\mathrm{TX}}||h_{\mathrm{fw}}||S_{\mathrm{Abs}}(\psi) - S_{\mathrm{Ref}}(\psi)||h_{\mathrm{bw}}| \text{ and} \tag{4.3}$$

$$\varphi_{h(\psi)} = \varphi_{h_{\mathrm{fw}}} + \varphi_{(S_{\mathrm{Abs}}(\psi) - S_{\mathrm{Ref}}(\psi))} + \varphi_{h_{\mathrm{bw}}}. \tag{4.4}$$

It can be observed that, if the transfer functions h_{fw} and h_{bw} are constant and independent of ψ, the dependency of $h(\psi)$ on ψ can be traced back to solely come from $Z_{\mathrm{Ant}}(\psi)$. In this case, the knowledge of $Z_{\mathrm{Ant}}(\psi)$ might be sufficient to correctly relate $h(\psi)$ to the sensing state ψ, i.e.,

$$h(\psi) = f(Z_{\mathrm{Ant}}(\psi)). \tag{4.5}$$

The sole knowledge about $Z_{\mathrm{Ant}}(\psi)$ would not be sufficient in case of sensing state dependent transfer functions $h_{\mathrm{fw}}(\psi)$ and $h_{\mathrm{bw}}(\psi)$.
In the following, a sensing system is investigated by means of the differential scattered field approach, allowing a more detailed study of the system. Furthermore, three different sensing models are derived, based on this approach.

Differential Scattered Field Analysis

In a far field and free space scenario, the load (Z) dependent scattered field $\vec{E}_{\mathrm{Scat}}(Z)$ of a receiving antenna can be described as the sum of a load independent component, the structural mode scattering, and a load dependent component, the antenna mode scattering [63]. Using the absorbing impedance Z_{Abs} of a UHF RFID chip as the load, the scattered field at a defined observation point is [64]

$$\vec{E}_{\mathrm{Scat}}(Z_{\mathrm{Abs}}) = \vec{E}_{\mathrm{Scat}}(Z_{\mathrm{Ant}}^*) - S_{\mathrm{Abs}} \frac{I_0 Z_{\mathrm{Ant}}}{2R_{\mathrm{Ant}}} \frac{\vec{E}_{\mathrm{Ant}}}{I_{\mathrm{Ant}}}, \tag{4.6}$$

where the structural mode component is the field scattered in case of a conjugate matched load $\vec{E}_{\mathrm{Scat}}(Z^*_{\mathrm{Ant}})$. The antenna mode component depends on the reflection coefficient in absorbing mode S_{Abs}, the antenna impedance Z_{Ant} and resistance R_{Ant}, the antenna current in case of a short circuit load I_0, and the antenna transmitting parameters $\vec{E}_{\mathrm{Ant}}$ and I_{Ant}. $\vec{E}_{\mathrm{Ant}}$ is the transmitted field at the observation point caused by the driving current I_{Ant}. When the tag changes from the absorbing mode to the reflecting mode, the scattered field changes to

$$\vec{E}_{\mathrm{Scat}}(Z_{\mathrm{Ref}}) = \vec{E}_{\mathrm{Scat}}(Z^*_{\mathrm{Ant}}) - S_{\mathrm{Ref}} \frac{I_0 Z_{\mathrm{Ant}}}{2R_{\mathrm{Ant}}} \frac{\vec{E}_{\mathrm{Ant}}}{I_{\mathrm{Ant}}}. \tag{4.7}$$

The differential scattered field $\Delta\vec{E}_{\mathrm{Scat}}$ can now be found by the difference between the two scattered fields as

$$\Delta\vec{E}_{\mathrm{Scat}} = \vec{E}_{\mathrm{Scat}}(Z_{\mathrm{Ref}}) - \vec{E}_{\mathrm{Scat}}(Z_{\mathrm{Abs}}) = (S_{\mathrm{Abs}} - S_{\mathrm{Ref}}) \frac{I_0 Z_{\mathrm{Ant}}}{2R_{\mathrm{Ant}}} \frac{\vec{E}_{\mathrm{Ant}}}{I_{\mathrm{Ant}}}. \tag{4.8}$$

It can be seen that $\Delta\vec{E}_{\mathrm{Scat}}$ is proportional to the difference between the two reflection coefficients in the absorbing and reflecting mode, which are functions of Z_{Ant} and Z_{Abs} or Z_{Ant} and Z_{Ref}, respectively. It should be noted that the other parameters in Eqn. 4.8 solely depend on the tag antenna characteristics. Fig. 4.2 shows the receiving antenna equivalent circuit at the reader receiver. The scattered field of the tag induces an open circuit voltage V_{oc}, which depends on the vector effective antenna lengths $\vec{\ell}_{\mathrm{e},r}$ in the direction of the tag, of [65]

$$V_{\mathrm{oc}} = \vec{\ell}_{\mathrm{e,r}} \vec{E}_{\mathrm{inc}}, \tag{4.9}$$

where $\vec{E}_{\mathrm{Inc}}$ is the incident field that is either $\vec{E}_{\mathrm{Scat}}(Z_{\mathrm{Abs}})$ or $\vec{E}_{\mathrm{Scat}}(Z_{\mathrm{Ref}})$. The voltage V_{L} on the receiver input impedance Z_{L} can then be calculated to

$$V_{\mathrm{L}} = V_{\mathrm{oc}} \frac{Z_{\mathrm{L}}}{Z_{\mathrm{Ant,R}} + Z_{\mathrm{L}}}, \tag{4.10}$$

where $Z_{\mathrm{Ant,R}}$ is the impedance of the reader RX antenna. Let V_{abs} be the voltage on Z_{L} when the tag is in the absorbing mode and V_{ref} be the voltage on Z_{L} when the tag is in the reflecting mode, then the tag signal h_{RF} can be calculated as the difference between these two voltages to

$$h_{\mathrm{RF}} = V_{\mathrm{ref}} - V_{\mathrm{abs}} = \frac{Z_{\mathrm{L}}}{Z_{\mathrm{Ant,R}} + Z_{\mathrm{L}}} \vec{\ell}_{\mathrm{e,r}} \Delta\vec{E}_{\mathrm{Scat}}. \tag{4.11}$$

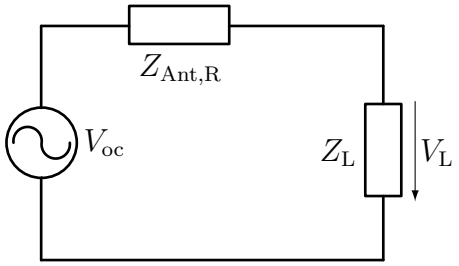

Figure 4.2: Reader receiving antenna equivalent circuit: A voltage V_{oc} is induced by the scatterd field received at the reader receiver antenna. The voltage V_{L} at the receiver input depends on the impedances $Z_{\mathrm{Ant,R}}$ and Z_{L}.

Furthermore, V_{abs} causes the baseband voltage state $S^{(A)}$ in the baseband signal constellation of Fig. 1.2, while V_{ref} causes $S^{(B)}$, leading to the baseband representation of the tag signal h of

$$h = S^{(B)} - S^{(A)}. \tag{4.12}$$

From Eqn. 4.11, it can be seen that the received tag signal at the reader is related to the differential scattered field of the tag. Thus, the investigation of the differential scattered field may be sufficient for the interpretation of the tag signal, when the receiver parameters are constant.
For further considerations in the next sections, $\Delta\vec{E}_{\mathrm{Scat}}$ will be represented in a different way. With [65]

$$I_0 Z_{\mathrm{Ant}} = V_{\mathrm{oc}} \tag{4.13}$$

and

$$\vec{E}_{\mathrm{Ant}} = -j\eta_0 \frac{I_{\mathrm{Ant}}}{2\lambda r} \vec{\ell}_{\mathrm{e,t}} e^{-j\beta_w r}, \tag{4.14}$$

the differential field can be represented by

$$\Delta\vec{E}_{\mathrm{Scat}} = -j(S_{\mathrm{Ref}} - S_{\mathrm{Abs}}) \frac{\vec{\ell}_{\mathrm{e,r}} \vec{E}_{\mathrm{inc}}}{2R_{\mathrm{Ant}}} \frac{\eta_0 \vec{\ell}_{\mathrm{e,t}}}{2\lambda r} e^{-j\beta_w r}, \tag{4.15}$$

where $\vec{\ell}_{\mathrm{e,r}}$ and $\vec{\ell}_{\mathrm{e,t}}$ are the vector effective length in the direction of the reader TX antenna and RX antenna, respectively, η_0 is the free space impedance, λ is

the wavelength, $\beta_{\mathrm{w}} = 2\pi/\lambda$ is the wavenumber and r is the distance between the tag and the observation point. In case of a monostatic reader, i.e., $\vec{\ell}_{\mathrm{e,r}} = \vec{\ell}_{\mathrm{e,t}}$, and assuming that there is no polarization mismatch between the incident field and the tag antenna, i.e., $\vec{\ell}_{\mathrm{e,r}}$ and $\vec{E}_{\mathrm{inc}}$ are parallel, $\Delta\vec{E}_{\mathrm{Scat}}$ becomes

$$\Delta\vec{E}_{\mathrm{Scat}} = -j(S_{\mathrm{Ref}} - S_{\mathrm{Abs}})\frac{|\vec{\ell}_{\mathrm{e,r}}|^2\vec{E}_{\mathrm{inc}}}{2R_{\mathrm{Ant}}}\frac{\eta_0}{2\pi r}e^{-j\beta_w r}. \tag{4.16}$$

$|\vec{\ell}_{\mathrm{e,r}}|^2$ can be related to the tag antenna gain G_{Tag} by [63]

$$|\vec{\ell}_{\mathrm{e,r}}|^2 = \frac{G_{\mathrm{Tag}}\lambda^2 R_{\mathrm{Ant}}}{\pi\eta_0}, \tag{4.17}$$

which now leads to the following representation of $\Delta\vec{E}_{\mathrm{Scat}}$,

$$\Delta\vec{E}_{\mathrm{Scat}} = -j(S_{\mathrm{Ref}} - S_{\mathrm{Abs}})\frac{G_{\mathrm{Tag}}\lambda\vec{E}_{\mathrm{inc}}}{4\pi r}e^{-j\beta_w r}. \tag{4.18}$$

If one uses $\Delta\vec{E}_{\mathrm{Scat}}$ to calculate the radar cross section (RCS) of a scattering antenna, as known from the radar technology, one gets [63]

$$4\pi r^2\frac{|\Delta\vec{E}_{\mathrm{Scat}}|^2}{|\vec{E}_{\mathrm{inc}}|^2} = |S_{\mathrm{Ref}} - S_{\mathrm{Abs}}|^2\frac{G^2\lambda^2}{4\pi}, \tag{4.19}$$

which agrees with the differential RCS defined in [10].

4.1.2 Distance Independent Sensing

Let ψ be the sensing state of interest, then the goal is that the sensing state dependent tag signal $h(\psi)$ follows a defined pattern that can be uniquely interpreted by the reader.
Figure 4.3 shows two exemplary detected tag signals $h_1(\psi)$ and $h_2(\psi)$ when the sensing state changes from ψ_{start} to ψ_{stop}. The appearance of $h_1(\psi)$ and $h_2(\psi)$ is simulated with Matlab, based on sensing model 1, which is introduced later. The knowledge of this sensing model is not jet necessary to demonstrate the idea of distance independence. Lets again assume that ψ is the filling level of an infusion bag with ψ_{start} and ψ_{stop} being the full and empty states,

respectively. The difference between $h_1(\psi)$ and $h_2(\psi)$ is the distance between the sensor tag (infusion bag) and the reader. In both cases, three extreme values, indicated by k_1, k_2 and k_3, can be clearly detected, although $h_1(\psi)$ is considerably smaller than $h_2(\psi)$, allowing a distance independent sensing. This exemplary tag signal pattern allows the differentiation in four discrete sensing states (two bit resolution). Lets assume that the infusion bag is full and the filling level decreases continuously and consecutively passes the extreme values, then, if:

- k_1 is not yet detected, the infusion bag is "almost full",
- k_1 is detected, the infusion bag is "more than half full",
- k_2 is detected, the infusion bag is "less than half full",
- k_3 is detected, the infusion bag is "almost empty".

According to Eqn. 4.11, the sensing state dependent tag signal $h(\psi)$ is

$$h(\psi) = \frac{Z_{\mathrm{L}}}{Z_{\mathrm{Ant,R}} + Z_{\mathrm{L}}} \vec{\ell}_{\mathrm{e,r}} \Delta \vec{E}_{\mathrm{Scat}}(\psi), \tag{4.20}$$

where it is assumed that only $\Delta \vec{E}_{\mathrm{Scat}}$ is affected by ψ, while the parameters of the receiver stay constant. For simplicity, it is assumed that $\Delta \vec{E}_{\mathrm{Scat}}(\psi)$ is linearly polarized with a unity vector of e_l and Eqn. 4.20 can be simplified to

$$h(\psi) = \frac{Z_{\mathrm{L}}}{Z_{\mathrm{Ant,R}} + Z_{\mathrm{L}}} \ell_{\mathrm{e,r,l}} \Delta E_{\mathrm{Scat,l}}(\psi), \tag{4.21}$$

where $\ell_{\mathrm{e,r,l}}$ is the component of $\vec{\ell}_{\mathrm{e,r}}$ in the direction of e_l and $\Delta E_{\mathrm{Scat,l}}(\psi)$ is the linear component of $\Delta \vec{E}_{\mathrm{Scat}}(\psi)$. From this representation one can easily see that the pattern of the tag signal $h(\psi)$ is proportional to the pattern of the scattered differential field $\Delta \vec{E}_{\mathrm{Scat}}(\psi)$ multiplied by a factor that is determined by the reader RX antenna. For the determination of the tag signal pattern received at the reader it is clear that $\Delta \vec{E}_{\mathrm{Scat}}(\psi)$ has to be investigated. Different models of $\Delta \vec{E}_{\mathrm{Scat}}(\psi)$ are set up and discussed in the following, which can be used for different scenarios.

Sensing model 1 (G_{Tag}, $\vec{E}_{\mathrm{inc}}$, $\vec{\ell}_{\mathrm{e,r}}$ constant versus ψ): Sensing model 1 is based on Eqn. 4.18, where it is assumed that G_{Tag} and $\vec{E}_{\mathrm{inc}}$ are independent of

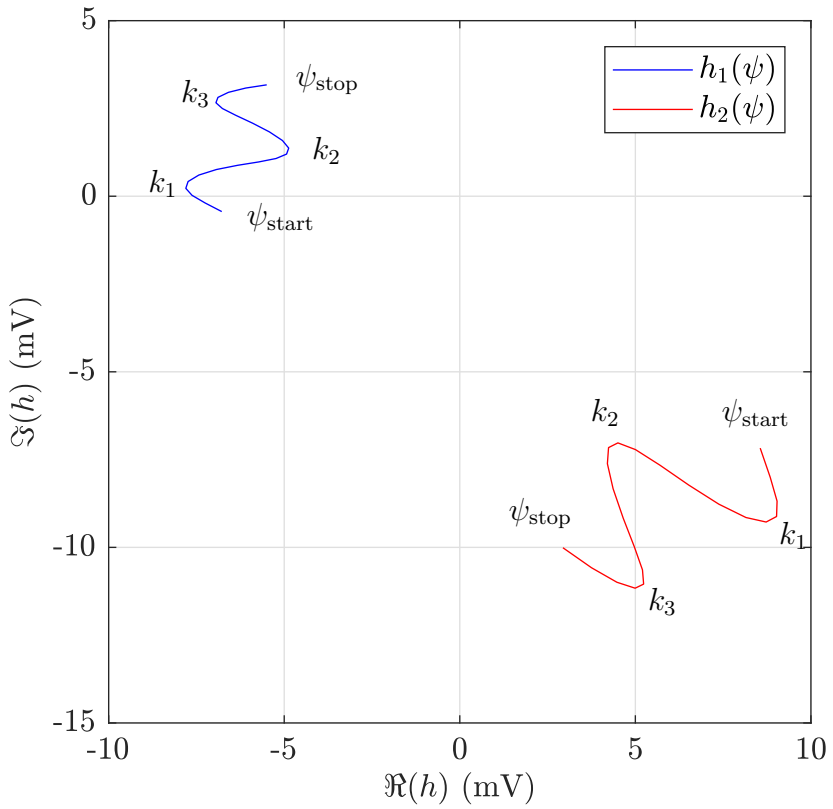

Figure 4.3: Ideal sensor tag signal constellation: Two exemplary detected tag signals $h_1(\psi)$ and $h_2(\psi)$ for different reader/tag distances versus sensing state that changes from ψ_{start} to ψ_{stop}. $h_1(\psi)$ and $h_2(\psi)$ are scaled and rotated with respect to each other, but the signal pattern stays the same.

ψ, which leads to

$$\Delta\vec{E}_{\mathrm{Scat}}(\psi) = -j(S_{\mathrm{Ref}}(\psi) - S_{\mathrm{Abs}}(\psi))\frac{G_{\mathrm{Tag}}\lambda\vec{E}_{\mathrm{inc}}}{4\pi r}e^{-j\beta_w r}. \tag{4.22}$$

It can be seen that the pattern of $h(\psi)$ solely depends on the pattern of $S_{\mathrm{Ref}}(\psi) - S_{\mathrm{Abs}}(\psi)$, i.e., $h(\psi) = f(Z_{\mathrm{Ant}}(\psi))$. $R_{\mathrm{Ant}}(\psi)$, which is the real part of $Z_{\mathrm{Ant}}(\psi)$, is related to the tag antenna gain G_{Tag}, as can be seen in Eqn. 4.17. Furthermore, this means that $R_{\mathrm{Ant}}(\psi)$ has to be kept constant versus ψ, i.e., $R_{\mathrm{Ant}}(\psi) = R_{\mathrm{Ant}}$. Ultimately, the sensor antenna has to be designed in a way that $Z_{\mathrm{Ant}}(\psi) = R_{\mathrm{Ant}} + jX_{\mathrm{Ant}}(\psi)$, i.e., only $X_{\mathrm{Ant}}(\psi)$ changes versus ψ, which strongly limits the possible patterns. This model has been used in [66] for stable and distance independent remote monitoring of infusion bags, without considering the mentioned constraint.

Sensing model 2 ($\vec{E}_{\mathrm{inc}}$, $\vec{\ell}_{\mathrm{e,r}}$ constant versus ψ): Sensing model 2 is based on Eqn. 4.16 and accounts for a sensing state dependent $R_{\mathrm{Ant}}(\psi)$, i.e., a change of the antenna gain G_{Tag} versus ψ. The model of $\Delta\vec{E}_{\mathrm{Scat}}(\psi)$ can be formulated to

$$\Delta\vec{E}_{\mathrm{Scat}}(\psi) = -j(S_{\mathrm{Ref}}(\psi) - S_{\mathrm{Abs}}(\psi))\frac{|\vec{\ell}_{\mathrm{e,r}}|^2\vec{E}_{\mathrm{inc}}}{2R_{\mathrm{Ant}}(\psi)}\frac{\eta_0}{2\pi r}e^{-j\beta_w r}. \tag{4.23}$$

It can be seen that the tag signal pattern can be controlled by $(S_{\mathrm{Ref}}(\psi) - S_{\mathrm{Abs}}(\psi))/R_{\mathrm{Ant}}(\psi)$ and is not restricted by the need of a constant R_{Ant}. This relation between the sensing state and the received tag signal has also been found by e.g. [67].
When comparing the two models of Eqn. 4.22 and Eqn. 4.23, it should be noticed that $\vec{\ell}_{\mathrm{e,r}}$ is assumed to be independent of R_{Ant}. This assumption comes from Eqn. 4.9 and the fact that the open circuit voltage V_{oc} (see Fig. 1.3) and the incident field $\vec{E}_{\mathrm{inc}}$ are independent of R_{Ant}.
An expansion of Eqn. 4.23 to the bistatic reader case and the permission of a polarization mismatch (see Eqn. 4.15) does not influence the received tag signal pattern and $\Delta\vec{E}_{\mathrm{Scat}}(\psi)$ is

$$\Delta\vec{E}_{\mathrm{Scat}}(\psi) = -j(S_{\mathrm{Ref}}(\psi) - S_{\mathrm{Abs}}(\psi))\frac{\vec{\ell}_{\mathrm{e,r}}\vec{E}_{\mathrm{inc}}}{2R_{\mathrm{Ant}}(\psi)}\frac{\eta_0\vec{\ell}_{\mathrm{e,t}}}{2\lambda r}e^{-j\beta_w r}. \tag{4.24}$$

It can be concluded that sensing model 2, as in the case of sensing model 1, only requires the knowledge of $Z_{\mathrm{Ant}}(\psi)$ to estimate the tag signal pattern $h(\psi)$, i.e., $h(\psi) = f(Z_{\mathrm{Ant}}(\psi))$.

Sensing model 3: Sensing model 1 and sensing model 2 assume that the current sensing state does not influence the propagation of the electric field, which is not the case in general. If one considers the influence of the field propagation, a driving current I_{Ant} causes a sensing state dependent field $\vec{E}_{\mathrm{Ant}}(\psi)$. Additionally, it can be assumed that the incident field $\vec{E}_{\mathrm{inc}}$ changes with the sensing state, which causes a sensing state dependent open circuit voltage $V_{\mathrm{oc}}(\psi) = I_0(\psi)Z_{\mathrm{Ant}}(\psi)$ at the sensor tag antenna. For the consideration of this influence, Eqn. 4.8 has been used as the basis relationship, leading to

$$\Delta\vec{E}_{\mathrm{Scat}}(\psi) = (S_{\mathrm{Abs}}(\psi) - S_{\mathrm{Ref}}(\psi))\frac{I_0(\psi)Z_{\mathrm{Ant}}(\psi)}{2R_{\mathrm{Ant}}(\psi)}\frac{\vec{E}_{\mathrm{Ant}}(\psi)}{I_{\mathrm{Ant}}}. \tag{4.25}$$

It can be seen that $\Delta\vec{E}_{\mathrm{Scat}}(\psi)$ cannot be described by the knowledge of $Z_{\mathrm{Ant}}(\psi)$ anymore, but requires the additional knowledge of the short circuit current $I_0(\psi)$ and the transmission properties $\vec{E}_{\mathrm{Ant}}(\psi)/I_{\mathrm{Ant}}$. It has to be noticed that $I_0(\psi)$ does not only scale with R_{Ant}, as it would be in the case of a constant V_{oc}. $I_0(\psi)$ and $\vec{E}_{\mathrm{Ant}}(\psi)/I_{\mathrm{Ant}}$ obviously change with the distance, however, the model assumes that relative changes of these parameters with respect to ψ stay the same. This would lead to similar tag signal patterns independent of the distance.
If the influence of the current sensing state on the propagation of the differential scattered field has to be considered, the design of a proper sensor gets even more complex.

4.1.3 Stable Sensing

As initially mentioned, a special attention is paid to achieve a stable communication within the whole sensing range. It is vital for a stable communication that a sufficient amount of power is available for chip operation and that a sufficient amount of signal power is backscattered to the reader. This can be achieved by a careful consideration of tag performance parameters, like the

power transmission coefficient τ and the modulation efficiency η (see Sec. 1.1.3). In case of sensing applications, these performance parameters are functions of the sensing state ψ:

$$\tau(\psi) = 1 - |S_{\text{Abs}}(\psi)|^2 \text{ and} \tag{4.26}$$

$$\eta(\psi) = \frac{1}{4}|S_{\text{Abs}}(\psi) - S_{\text{Ref}}(\psi)|^2. \tag{4.27}$$

Stable sensing is now reached by restricting $\tau(\psi)$ and $\eta(\psi)$ to a certain range of values. In particular in the case of passive sensor tags, it is important to ensure high $\tau(\psi)$ values and a restriction of $\tau(\psi) \geq 0.9$ might be desirable. This means that at least 90% of the available power is transferred to the chip within the whole sensing range. Figure 4.4 shows an exemplary sensor tag response diagram. It can be seen that all $S_{\text{Abs}}(\psi)$ values are within a circle, which represents the $\tau(\psi) = 0.9$ border. These restriction on $\tau(\psi)$ guarantees at the same time a high modulation efficiency of $\eta(\psi) > \frac{1}{4}0.46$, which means that $\eta(\psi)$ is at least 46% of an ideally amplitude modulated tag signal. The $S_{\text{Abs}}(\psi)$ and $S_{\text{Ref}}(\psi)$ values in Fig. 4.4 even achieve $\eta(\psi) > \frac{1}{4}0.64$.
It can bee seen that the pattern of $S_{\text{Abs}}(\psi)$ is very similar to the tag signal pattern presented in Fig. 4.3. And indeed, the sensor tag response diagram of Fig. 4.4 causes tag signal patterns shown in Fig. 4.3, if using sensing model 1 and assuming a constant sensor tag antenna gain. If using sensing model 2, the sensor tag response diagram can be easily modified with respect to $R_{\text{Ant}}(\psi)$, to achieve the desired tag signal pattern. In case of sensing model 3, the tag signal pattern cannot be directly related to the reflection coefficients and $R_{\text{Ant}}(\psi)$ anymore.

4.2 Sensor Tag Prototype

This section presents a prototype of a sensor tag, following the presented concept of tag signal pattern detection at the reader. The sensing application is the remote monitoring of the water filling level ψ, which is similar to the remote monitoring of infusion bags. Such a scenario requires the use of sensing model 3, as the water has a significant influence on the field propagation. The sensor

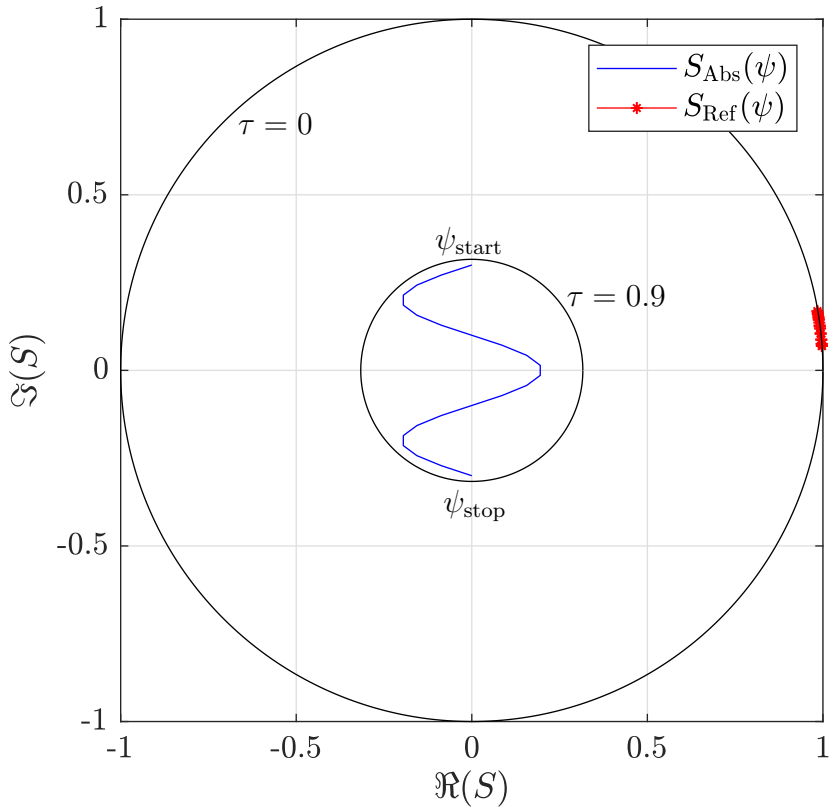

Figure 4.4: Ideal sensor tag response diagram: $S_{\mathrm{Abs}}(\psi)$ is restricted to be within a circle where $\tau(\psi) \geq 0.9$. This also means that $\eta(\psi) > \frac{1}{4}0.46$, assuming $|S_{\mathrm{Ref}}(\psi)| = 1$. Thus, the communication performance parameters of the sensor tag are kept high within the whole sensing range.

antenna is simulated in CST Microwave Studio and the differential scattered field is calculated in Matlab. The produced sensor tag prototype has been tested in an anechoic chamber. Furthermore, a modified off-the-shelf metal tag has been used as water level sensor tag and has been measured in the anechoic chamber, as well as in a multipath laboratory environment.

4.2.1 Simulations

Setup

The simulations for the sensor tag prototype were done in CST Microwave Studio. Figure 4.5 shows the final design dimensions of the sensor antenna for the sensor tag prototype. The T-matched dipole is made of copper with a thickness of 17.5 μm and is mounted on FR4 (relative permittivity $\epsilon_r = 4.3$) substrate with a thickness of 1.55 mm. The chip connecting pads have been designed for assembling an NXP UCODE 7 chip [68]. The specified chip absorbing impedance of the UCODE 7 chip at 915 MHz is $Z_{\text{Abs}} = 12.8\ \Omega - \text{j}248\ \Omega$, while the chip reflecting impedance is assumed to be $Z_{\text{Ref}} = 2\ \Omega - \text{j}0.1\ \Omega$. If not stated otherwise, simulation results are presented for an operating frequency of 915 MHz.

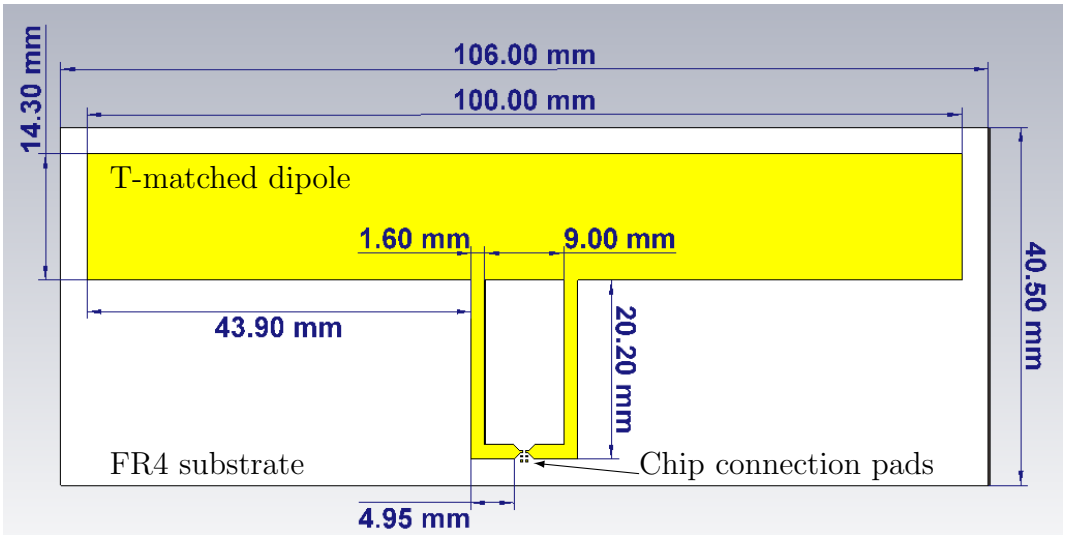

Figure 4.5: Sensor tag prototype design: Final dimensions of the T-matched dipole that is made of copper with a thickness of 17.5 μm. The antenna is fixed on FR4 (relative permittivity $\epsilon_r = 4.3$) substrate with a thickness of 1.55 mm. The chip connecting pads are designed for assembling an NXP UCODE 7 chip.

The sensing scenario is shown in Fig. 4.6. The sensor tag antenna is attached vertically on a 0.5 mm thick plastic canister with $\epsilon_r = 2.26$, which separates the tag from the water with $\epsilon_r = 78$. The sensor tag antenna is vertically tilted

by 8 degrees, where the bottom near part touches the plastic. This tilting is done to prevent a too large variation of the antenna input impedance within the sensing range. The sensing range is from $\psi_{\text{start}} = 0$ mm to $\psi_{\text{stop}} = 100$ mm, where ψ_{start} is at the height of the lower end of the antenna (copper), as can be seen in Fig. 4.6.

Results

The simulation procedure was divided into two parts in order to get all necessary information for the use of sensing model 3. This incorporates all necessary information for the use of sensing model 1 and 2, if applicable. In a first step, the antenna was stimulated at the upper two chip connection pads (see Fig. 4.5) and the antenna input impedance Z_{Ant} has been recorded for a water level sweep from ψ_{start} to ψ_{stop} in 10 mm steps. Furthermore, the driving current I_{Ant} of the discrete simulation port and the electric field $\vec{E}_{\text{Ant}}$ have been monitored. More precisely, the vertical part (parallel to the plastic layer) of $\vec{E}_{\text{Ant}}$, $E_{\text{Ant,v}}$, has been monitored at a distance of 610 mm in front of the sensor.
In a second step, the antenna was shorted at the upper two chip connection pads with a very low discrete resistor element for the simulation of the short circuit antenna current I_0. Furthermore, the same antenna was copied and mirrored (without a tilt) and used as a field source 500 mm away from the sensor, which can be seen in Fig. 4.7. During a water level sweep from ψ_{start} to ψ_{stop}, I_0 at the discrete resistor element has been monitored. At this point, it should be mentioned that the measurement of I_0 at an other distance between source and sensor does not influence the pattern of the differential scattered field.
The mentioned two steps provide all necessary information for the application of the three sensing models. The simulation results are in the following again split into a distance independent sensing part and a stable sensing part.

Distance independent sensing: As already mentioned above, in order to ensure a distance independent sensing, the antenna has to be designed in a way that distinctive tag signal patterns can be detected at the reader. Fig. 4.8 shows the differential scattered field $\Delta\vec{E}_{\text{Scat}}(\psi)$ that has been calculated with Matlab from the CST simulation results by means of sensing model 3.

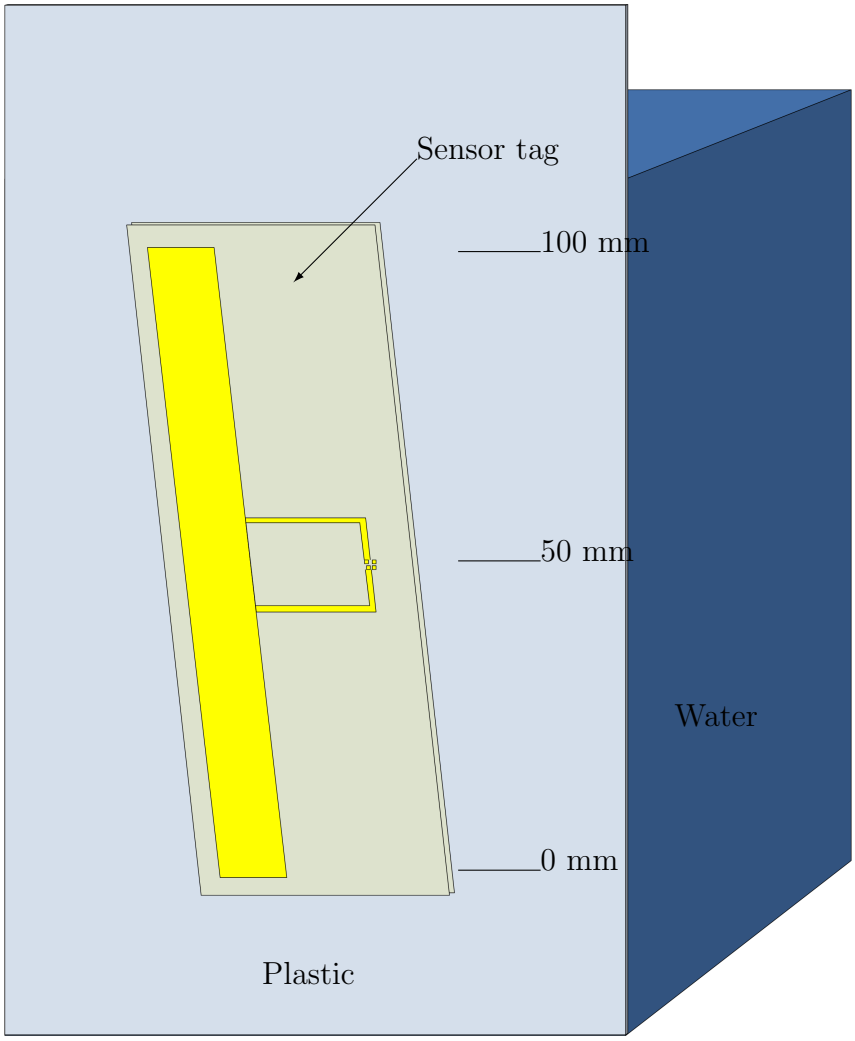

Figure 4.6: Sensing scenario: The sensor tag antenna is attached vertically on a 0.5 mm thick plastic with $\epsilon_r = 2.26$. The sensor tag antenna is vertically tilted by 8 degrees to prevent a too large variation of the antenna input impedance, where the bottom near part touches the plastic. The water ($\epsilon_r = 78$) level is changed from $\psi_{start} = 0$ mm to $\psi_{stop} = 100$ mm. $Z_{Ant}(\psi)$, $I_{Ant}(\psi)$ and $\vec{E}_{Ant}(\psi)$ are recorded in each of these simulation steps.

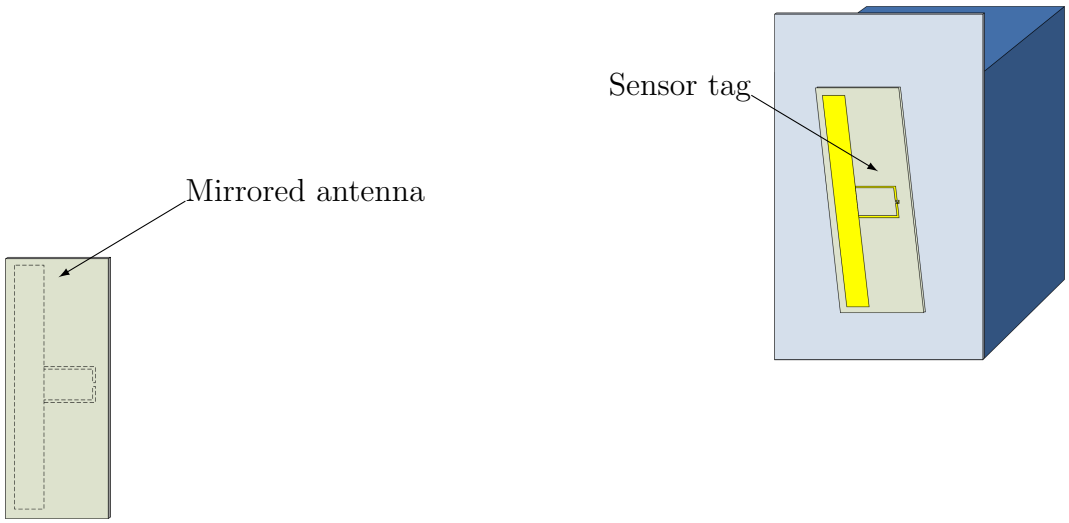

Figure 4.7: Simulation setup: The short circuit antenna current $I_0(\psi)$ is recorded at the short circuited sensor tag antenna chip connection pads. The electric field is produced by the mirrored antenna.

$\Delta\vec{E}_{\mathrm{Scat}}(\psi)$ is calculated by means of the vertical part of $\vec{E}_{\mathrm{Ant}}(\psi)$ ($E_{\mathrm{Ant,v}}(\psi)$) and is thus also vertical, i.e., $\Delta\vec{E}_{\mathrm{Scat}}(\psi) = \Delta E_{\mathrm{Scat,v}}(\psi)$.
The trend of $\Delta\vec{E}_{\mathrm{Scat}}(\psi)$ in Fig. 4.8 shows a very distinctive pattern between 0 mm and about 40 mm. According to Eqn. 4.21, the tag signal pattern of $h(\psi)$ is $\Delta\vec{E}_{\mathrm{Scat}}(\psi)$ scaled by the receiving antenna parameters. A detection and interpretation of $h(\psi)$ between 0 mm and about 40 mm leads to a binary sensor. Lets more concretely assume that the canister is full and ψ continuously decreases. If the mentioned distinctive pattern is now detected at the reader, it means that the filling level is around 0 mm. In this case, the binary sensing state changes from "not almost empty" to "almost empty".

Stable sensing: $S_{\mathrm{Abs}}(\psi)$ and $S_{\mathrm{Ref}}(\psi)$ have been calculated according to Eqn. 4.1 and Eqn. 4.2, respectively. The corresponding sensor tag response can be seen in Fig. 4.9, showing that $S_{\mathrm{Abs}}(\psi)$ is within the $\tau = 0.9$ circle for all sensing states. Thus a stable power transfer to the tag chip within the full sensing range is guaranteed. Detailed values of τ can be seen in Tab. 4.1.
Table 4.1 also lists the modulation efficiency $\eta(\psi)$ of the sensor tag normalized by $\alpha = \frac{1}{4}$. This allows the direct comparison of the sensor tag to an ideal am-

Table 4.1: Simulated stability of sensor tag: $\tau(\psi)$ and $\eta(\psi)/\alpha$ are listed, where $\alpha = \frac{1}{4}$. This allows a direct comparison of the stability with an ideal amplitude modulated tag, where $\tau = 1$ and $\eta(\psi)/\alpha = 1$.

ψ (mm)	$\tau(\psi)$	$\eta(\psi)/\alpha$
0	0.98	0.94
10	0.91	1.05
20	0.92	1.12
30	0.95	1.19
40	0.98	1.2
50	0.98	1.22
60	0.96	1.42
70	0.94	1.45
80	0.94	1.46
90	0.93	1.52
100	0.92	1.55

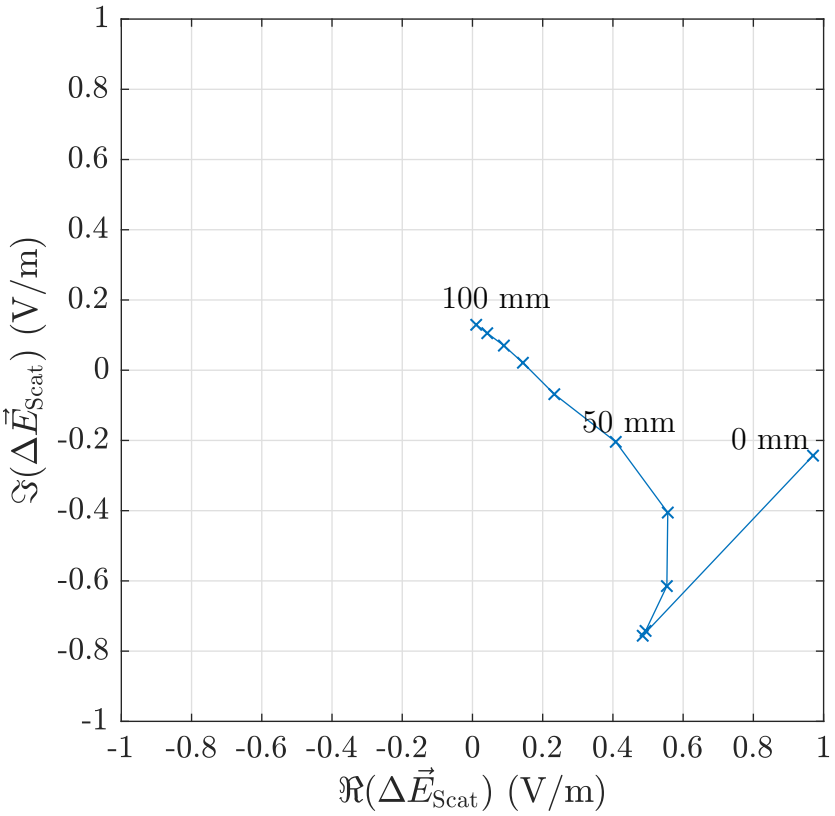

Figure 4.8: Simulated differential scattered field: $\Delta\vec{E}_{\mathrm{Scat}}(\psi)$ shows a very distinctive pattern between 0 mm and about 40 mm. Such patterns are targeted to allow a good sensing state detection at the reader. $\Delta\vec{E}_{\mathrm{Scat}}(\psi)$ is calculated with Matlab from the CST simulation results by means of sensing model 3.

plitude modulated tag. It can be seen that for almost all sensing states $\eta(\psi)/\alpha$ is greater than 1 and thus better than η/α of an ideal amplitude modulated tag. In summary, it can be said that the performance of the sensor tag is stable within the whole sensing range. Thus, a permanent communication between the reader and the sensor tag can be guaranteed with a high probability.

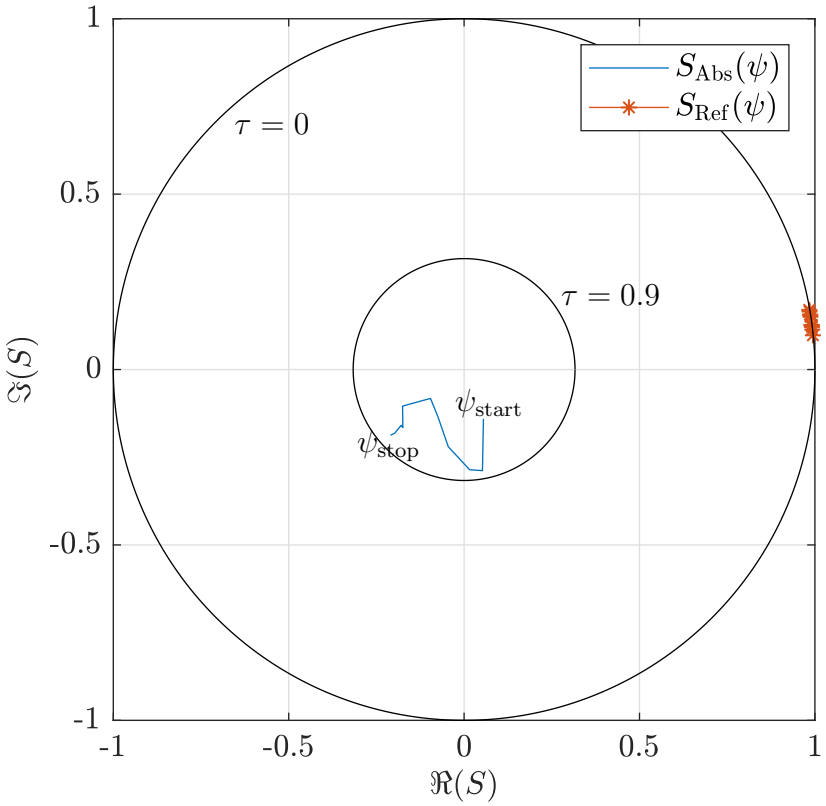

Figure 4.9: Simulated sensor tag response diagram: $S_{\mathrm{Abs}}(\psi)$ is within the $\tau = 0.9$ circle for all sensing states and a stable sensing is assured.

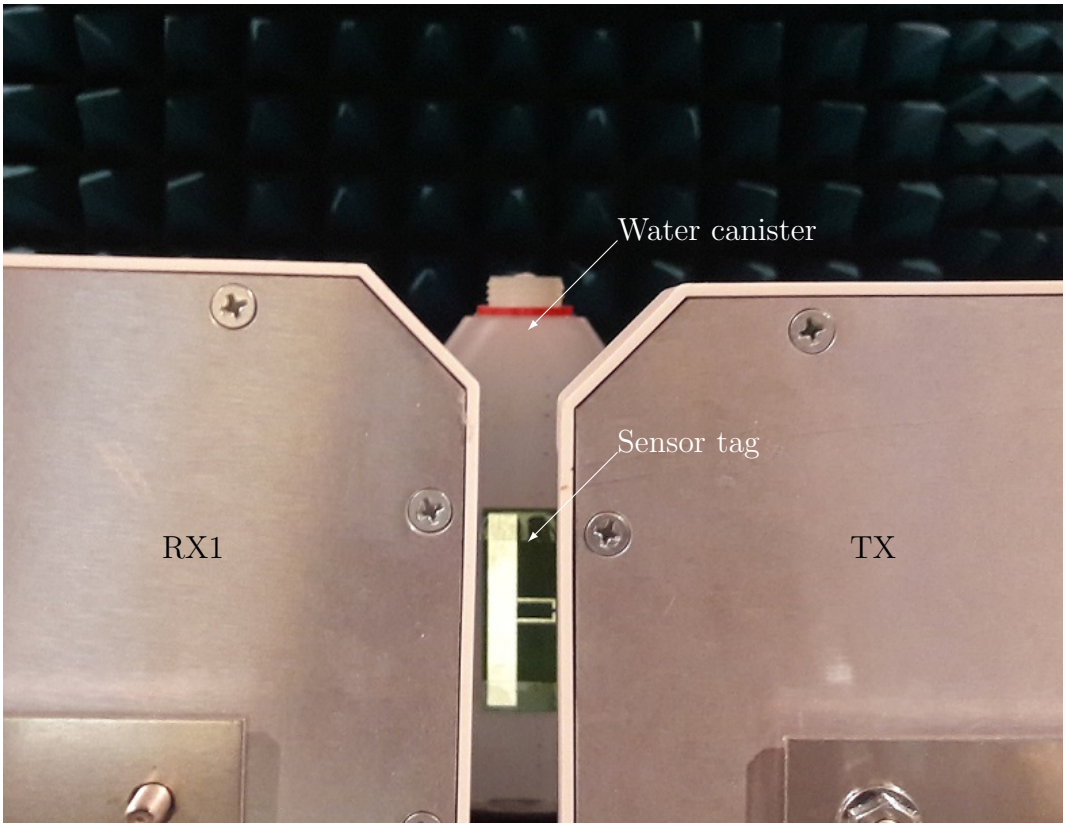

Figure 4.10: Sensor system measurements in the anechoic chamber: The produced sensor tag prototype is mounted with a tilt on the water canister. The canister is positioned in front of the reader antennas TX and RX1.

4.2.2 Measurements

A sensor tag prototype has been produced with antenna dimensions according to Fig. 4.5 and an assembled NXP UCODE 7 chip. A first verification measurement has been done in the anechoic chamber. The measurement setup can be seen in Fig. 4.10. The sensor tag is mounted on the water canister with a tilt as described above in the simulation model. The measurements have been done with the RPRP, using the TX and RX1 antennas and an operating frequency of 897 MHz. Note that this operating frequency is not the same as used for the simulations above. This frequency shift accounts for a slightly different behavior of the produced sensor tag as expected from the simulations. This

different behavior is either caused by differences between the simulated and the actual antenna impedance, by deviations from the assumed chip impedances, or a combination of both. An adjustment of the operating frequency has the effect that the actual $S_{\mathrm{Abs}}(\psi)$ values are shifted towards the origin of the tag response diagram, as it is the case for the simulated values of $S_{\mathrm{Abs}}(\psi)$ (see Fig. 4.9). The slightly different behavior has been recognized in an earlier experiment. In particular, I measured the minimum power necessary to turn on the sensor tag (without the cansister) versus frequency with the RPRP, as e.g., described in [69]. These measurements show that the read range is maximized for an operating frequency of 897 MHz. Furthermore, this means that the power transfer to the chip (τ) is maximized at this frequency. However, based on the simulations, this frequency was expected to be around 915 MHz.
The tag signal was recorded at two different distances between the reader antennas and the tag, 510 mm and 610 mm, while the water level in the canister has been changed from 0 mm to 100 mm in 10 mm steps. The output power of the RPRP was adjusted for each measurement point to minimize nonlinear effects caused by the chip [4]. However, the different output power is considered in the representation of the tag signals. The two tag signals $h_1(\psi)$ and $h_2(\psi)$ recorded at 510 mm and 610 mm, respectively, are shown in Fig. 4.11. Ideally, $h_2(\psi)$ should be a scaled and rotated version of $h_1(\psi)$, which is observable with only small deviations. It can also be observed that the measured pattern is similar to the expected pattern shown in Fig. 4.8. These results suggest that sensing model, simulations and measurements are valid.

Further Measurements

Finally, a modified off-the-shelf metal tag has been used as a water filling level sensor tag, to further strenghten the sensing concept. The same metal tag [62] is used as used for the tracking system. However, the backside of the tag, which includes a metal shield, is removed, in order to increase the influence of the water on the tag. As there are no details about the used antenna, i.e., $Z_{\mathrm{Ant}}(\psi)$, only investigations with respect to the distance independence of the sensor system are done. In a first measurement campaign, the sensing system with the off-the-shelf sensor was investigated in the anechoic chamber. Figure 4.12 shows the measurement setup, where the sensor tag is mounted vertically at the water canister. The backscattered tag signal has been captured between 0

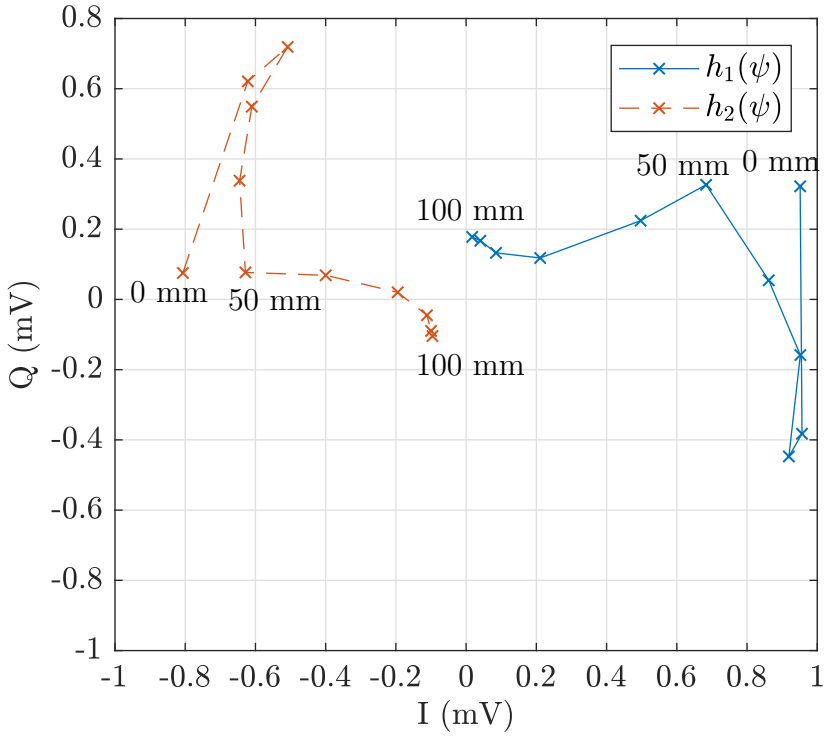

Figure 4.11: Measured sensor tag signal constellation: $h_1(\psi)$ and $h_2(\psi)$ are measured at a distance of 510 mm and 610 mm, respectively. $h_1(\psi)$ and $h_2(\psi)$ are scaled and rotated with respect to each other. The pattern of the two signals is similar to the simulated differential scattered field shown in Fig. 4.8.

mm and 210 mm in 10 mm steps at three different distances, 1.05 m, 1.35 m and 1.65 m.
Figure 4.13 shows the tag signal constellation for all three distances, with the corresponding tag signals $h_1(\psi)$ (1.05 m), $h_2(\psi)$ (1.35 m) and $h_3(\psi)$ (1.65 m). It can be seen that the three tag signal patterns are very similar. As expected, the three signal patterns are scaled and rotated with respect to each other, but the patterns are comparable. These tag signal patterns were measured at a fixed RPRP output power of about 26 dBm without considering nonlinear effects of the tag chip. An additional tag signal, h_4 has been measured at 1.05 m with a reduced output power of 22 dBm, trying to operate the chip in a more linear region. It can be seen that the tag signal patterns of $h_3(\psi)$ and $h_4(\psi)$ differ in the sensing region towards 0 mm water filling level, although the patterns are still comparable. However, the tag signal patterns of $h_1(\psi)$ and $h_4(\psi)$, which show the largest distance difference, got more similar with the reduced non linear chip effects. In conclusion it can be said that a distance independent sensing is possible, even in case of non linear chip effects, but also that these effects have to be considered in future research.
In a further step, the behavior of the sensor tag in a multipath environment is investigated. Figure 4.14 shows the laboratory in which the measurements have been conducted. For the measurements in the laboratory, a different reader antenna setup was used, compared to the measurements in the anechoic chamber. This was done in order to also get measurement data for further investigations with respect to simultaneous tag tracking and sensing. However, only the sensing relevant investigations are presented here. The tag signal has again been captured between 0 mm and 210 mm in 10 mm steps at two different positions with the coordinates (0 m, 1 m) and (0.7 m, 1 m), respectively. Figure 4.15 shows the captured tag signal constellation, where $h_1(\psi)$ and $h_2(\psi)$ are the tag signals from the first position, received at RX1 and RX2, respectively. $h_3(\psi)$ and $h_4(\psi)$ are the tag signals received from the second position. The received tag signals are influenced by several effects, as multipath propagation, nonlinearity of the tag chip and so forth, which change from position to position. However it is still possible to recognize distinctive and comparable tag signal patterns for all four tag signals. In general, it might also be seen that the resolution of the sensing states is limited, e.g., to a two bit resolution (see Fig. 4.3) or a three bit resolution.

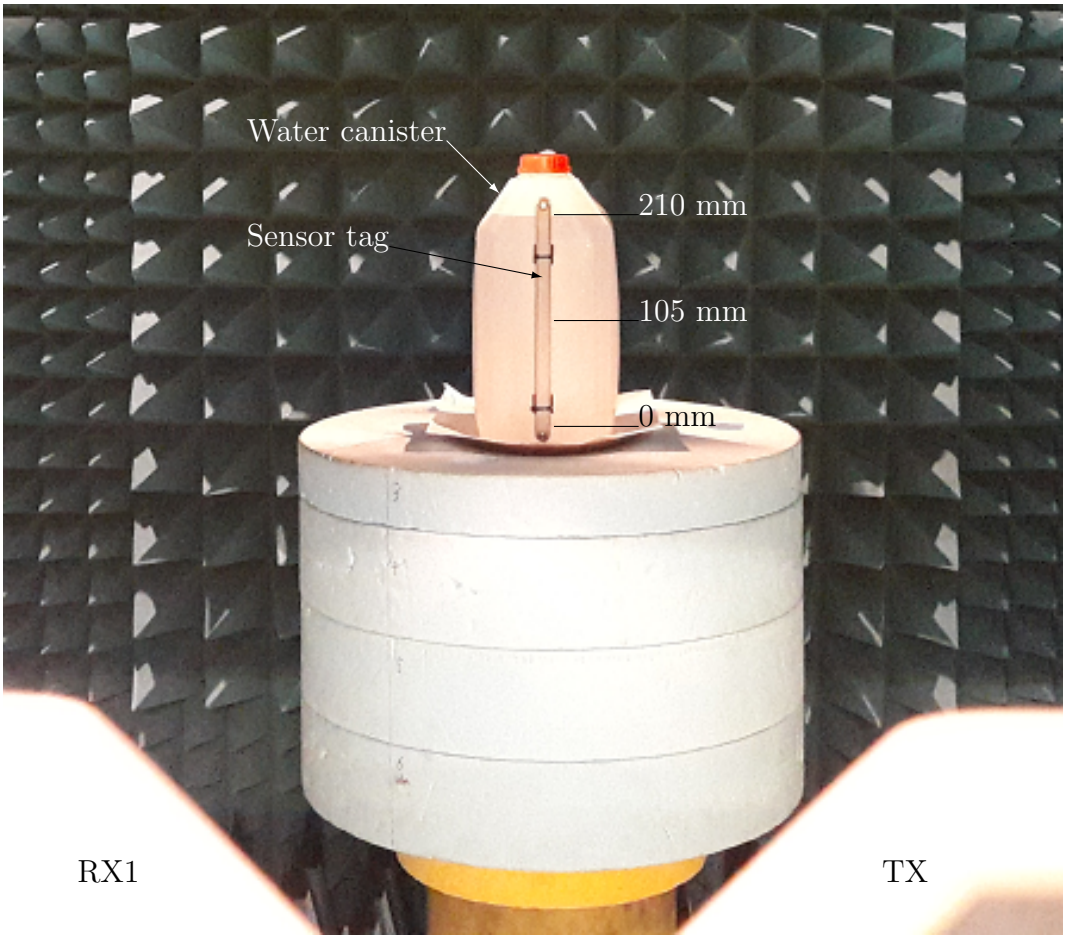

Figure 4.12: Sensor system measurements in the anechoic chamber (modified off-the-shelf metal tag): The modified off-the-shelf metal tag is mounted on the water canister. The canister is centered in front of the reader antennas TX and RX1.

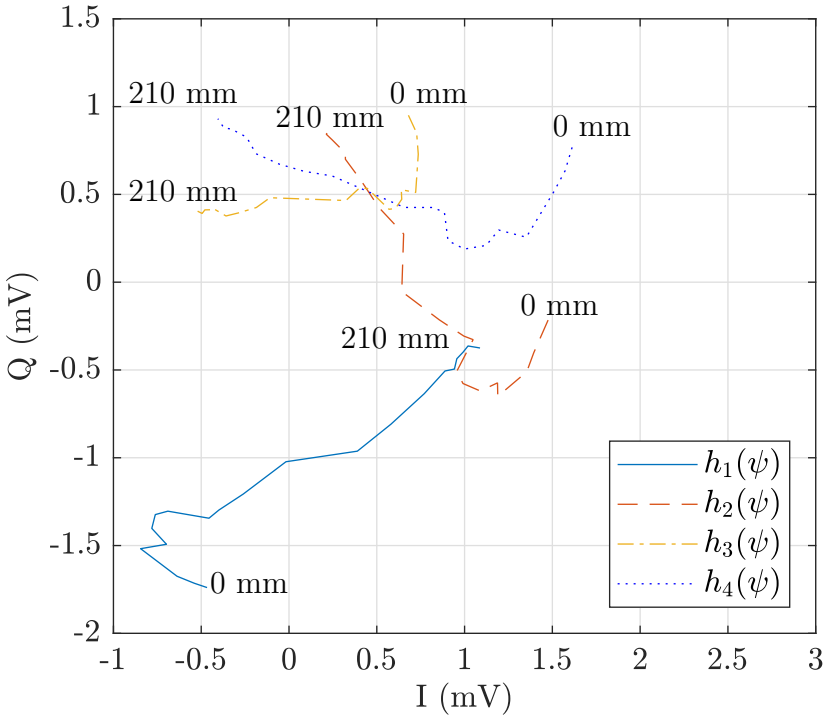

Figure 4.13: Measured sensor tag signal constellation (modified off-the-shelf metal tag): $h_1(\psi)$, $h_2(\psi)$ and $h_3(\psi)$ are measured at a distance of 1.05 m, 1.35 m and 1.65 m respectively. The patterns of $h_1(\psi)$, $h_2(\psi)$ and $h_3(\psi)$ are similar but nonlinear effects of the tag can be observed. $h_4(\psi)$ is measured at 1.05 m, but with reduced reader transmit power. The patterns of $h_3(\psi)$ and $h_4(\psi)$ show the greatest similarity.

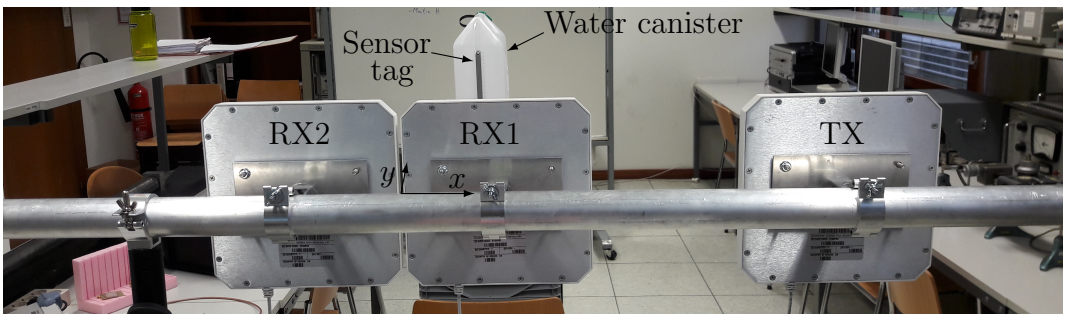

Figure 4.14: Sensor system measurements in the laboratory (modified off-the-shelf metal tag): The reader antenna setup is similar to the one used for tag tracking. The measurements have been conducted at two different parallel (same y coordinate) positions: (0 m, 1 m) and (0.7 m, 1 m).

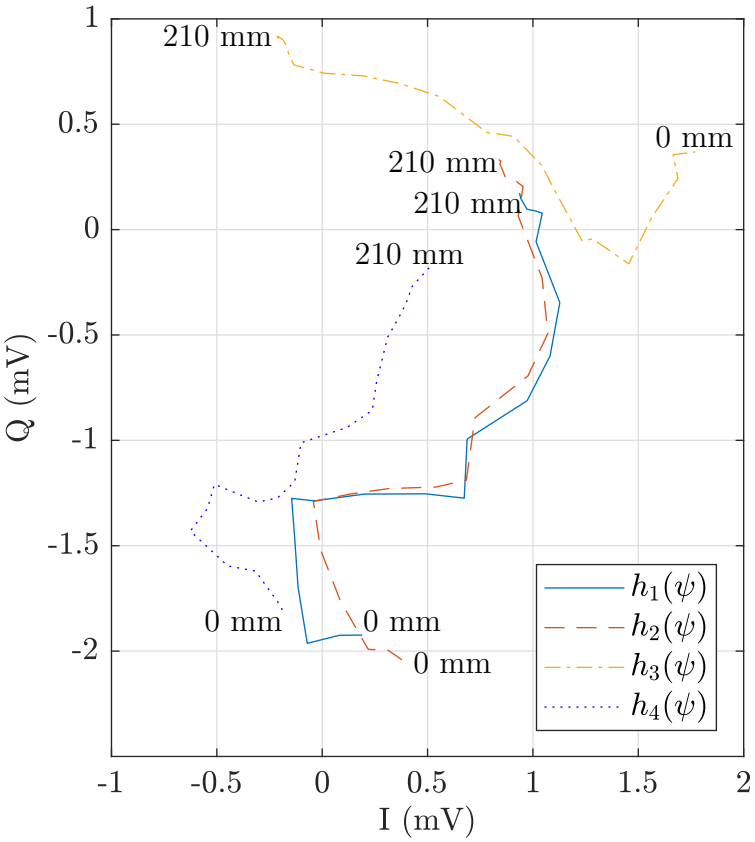

Figure 4.15: Measured sensor tag signal constellation in a multipath propagation environment (modified off-the-shelf metal tag): $h_1(\psi)$ and $h_2(\psi)$ are measured at the first position (0 m, 1 m) at both receiving antennas RX1 and RX2, respectively. $h_3(\psi)$ and $h_4(\psi)$ are measured at the second position (0.7 m, 1 m), again at both receiving antennas. Different positions mean different multipath channels and different effects of tag nonlinearities, but still similar patterns can be observed.

4.3 Summary

This chapter presents a novel sensor tag system that is based on the passive UHF RFID technology. The sensor systems allows the detection of discrete sensing states based on the detection of defined tag signal patterns at the reader receiver. These tag signal patterns get rotated and scaled with the distance between the reader and the sensor tag, but do not change the shape, which is exploited for the distance independent operation. Thus, there is no need for reference tags or custom-built chips, as presented in related work. Also, three different sensing models are presented, whose usability depend on the complexity of the sensing environment.
Furthermore, the design and realization of the sensor tags consider a strict adherence of tag performance parameters to ensure a stable communication during the sensing process. This is reached by keeping the power transfer towards the sensor tag chip, as well as the backscattered tag signal power sufficiently high.
A sensor tag prototype has been realized that follows the most general presented sensing model, which has been shown by measurements in an anechoic chamber. Furthermore, a modified off-the-shelf metal tag has been used as sensor tag. Measurements in the anechoic chamber and a laboratory environment show the distance independence of the system and a robustness in multipath propagation environments.

5 Conclusions

This thesis presents a novel tracking system and a novel sensing system that are based on the UHF RFID technology. The ultimate vision is the combination of both individual systems into a system that enables the tracking of low-cost sensors in multipath propagation environments with room level dimensions. Tracking of infusion bags in hospital rooms, while sensing the filling level of them, is an application example of the system. The operation in multipath propagation environments typically impairs the power transfer to the sensors and distorts the detected sensor signals. This thesis solves several problems that arise from using the narrowband UHF RFID technology for tracking and sensing in typical application environments.
An RPRP has been developed in the early state of the work in order to enable the rapid prototyping and testing of novel tracking and sensing systems. The performance requirements on the RPRP are deduced from channel measurements in a harsh multipath propagation environment, acting as a worst case scenario. The two novel UHF RFID based systems have been developed and tested with the RPRP and are summarized and discussed in the following.

Tracking System

This chapter presents a novel 2D tracking system based on a SIMO antenna configuration. One TX and two RX antennas are horizontally separated with certain distances to each other at the same height, facing in the same direction. The special antenna setup allows an estimation of a position update based on geometrical system properties and tag signal phase measurements.
Measurements and theoretical investigations show that the tracking system is very robust in multipath propagation environments with room level dimensions. The tracking system is compared to a 2D localization system that has been developed based on the combination of known DoA and range estimations. The

theoretical influence of a phase error due to multipath propagation is three times larger in the 2D localization system. The clear performance advantage of the novel tracking system is also shown by measurements in an anechoic chamber. Furthermore, the tracking system provides the analytically calculated position update within only one communication cycle between the reader and the tag and is thus suitable for the tracking of fast changing tag positions.
The tracking system performs very good in multipath propagation environments when the starting position is known. The best performance might be reached for applications with defined starting positions and the tracking of the y coordinate with fixed x coordinates, as the y coordinate can be estimated very accurately. In applications, where the starting position is not defined and thus unknown, the trajectory of the starting position can be estimated by the DoA and a rough range might be estimated by the localization system. A more precise starting position might be "learned" by using the knowledge about room dimensions and conditions. For example, if the tag is estimated to be in a side wall of the room, it can be assumed that the starting position was inaccurate. After sufficient time and tag movement, the accuracy of the starting position might be enhanced by the accumulated foreknowledge.

Sensor System

This chapter presents a sensor tag system that is based on the passive UHF RFID technology. The sensor systems allows the detection of discrete sensing states based on the detection of defined tag signal patterns at the reader receiver. These tag signal patterns get rotated and scaled with the distance between the reader and the sensor tag, but do not change the shape. Thus a distance independent sensing is provided by the sensor system. Three different sensing models are presented, whose usage depend on the complexity of the sensing application. Furthermore, the design and realization of the sensor tags consider a strict adherence of tag performance parameters to ensure a stable communication during the sensing process. This is reached by keeping the power transfer towards the sensor tag chip and the backscattered tag signal power sufficiently high. A stable and distance independent sensor system that uses sensor tags, consisting of a single sensor antenna and a single off-the-shelf chip, is novel compared to related work.
A sensor tag prototype is realized that follows the most general presented

sensing model, which has been shown by measurements in an anechoic chamber. Furthermore, a modified off-the-shelf metal tag has been used as sensor tag. Measurements in the anechoic chamber and in a laboratory environment show the distance independence of the system and a robustness in multipath propagation environments.
The concept of stable and distance independent sensing has been verified by the realization and the measurement of a sensor tag prototype. Future work will include further measurements at different distances and positions in different scenarios to further strengthen the concept and to make more detailed investigations. The number of detectable discrete sensing states is restricted, but a concrete specification of the maximum value requires the realization of new prototypes. The identification of further applications is also planed in future work.

Appendix A

Own Publications

L. Görtschacher, J. Grosinger, B. Auinger, D. Amschl, P. Priller, U. Muehlmann, and W. Bösch, "SIMO RFID System Performance in an Engine Test Bed." In: *Proc. IEEE International EURASIP Workshop on RFID Technology (EURFID)*, 2015.

L. Görtschacher, J. Grosinger, H.N. Khan, B. Auinger, D. Amschl, P. Priller, U. Muehlmann, and W. Bösch, "SIMO UHF RFID Reader Using Sensor Fusion for Tag Localization in a Selected Environment." In: *e & i Elektrotechnik und Informationstechnik*, 2016.

L. Görtschacher, J. Grosinger, H.N. Khan, D. Amschl, P. Priller, U. Muehlmann, and W. Bösch, "SDR Based RFID Reader for Passive Tag Localization Using Phase Difference of Arrival Techniques." In: *Proc. IEEE MTT-S International Microwave Symposium (IMS)*, 2016.

J. Grosinger, **L. Görtschacher**, and W. Bösch, "Sensor Add-On for Batteryless UHF RFID Tags Enabling a Low Cost IoT Infrastructure." In: *Proc. IEEE MTT-S International Microwave Symposium (IMS)*, 2016.

J. Grosinger, **L. Görtschacher**, and W. Bösch, "Passive RFID Sensor Tag Concept and Prototype Exploiting a Full Control of Amplitude and Phase of the Tag Signal." In: *IEEE Transactions on Microwave Theory and Techniques*, 2016.

H. N. Khan, J. Grosinger, **L. Görtschacher**, D. Amschl, P. Priller, U. Muehlmann, and W. Bösch, "Statistical Analysis of the Power Delay Profile of a SIMO UHF Backscatter RFID Channel in an Engine Test Bed." In: *Proc. IEEE Loughborough Antennas Propagation Conference (LAPC)*, 2016.

L. Görtschacher, J. Grosinger, H.N. Khan, and W. Bösch, "Fast Two Dimensional Position Update System for UHF RFID Tag Tracking." In: *Proc. IEEE MTT-S International Microwave Symposium (IMS)*, 2017.

F. Berra, **L. Görtschacher**, A. Costanzo, and J. Grosinger, "Space Mapping Design Method for an Antenna Transducer of a Bend Sensor RFID Tag." In: *Proc. IEEE 47th European Microwave Conference (EuMC)*, 2017.

L. Görtschacher, W. Bösch, and J. Grosinger, "UHF RFID Sensor Tag Antenna Concept for Stable and Distance Independent Remote Monitoring." In: *Proc. IEEE International Microwave Biomedical Conference (IMBioC)*, 2018.

List of Figures

Acronyms

2D	two dimensional.
BW	bandwidth.
CDF	cumulative distribution function.
CW	continuous wave.
DC	direct current.
DoA	direction of arrival.
EIRP	effective isotropic radiated power.
ERP	effective radiated power.
ETSI	European telecommunications standards institute.
FCC	federal communications commission.
FD-PDoA	frequency domain phase difference of arrival.
FoM	figure of merit.
HF	high frequency.
I	Inphase.
ID	identification number.
IHF	Institute of Microwave and Photonic Engineering.

ISAR	inverse synthetic aperture radar.
LF	low frequency.
LNA	low noise amplifier.
LO	local oscillator.
MIMO	multiple input multiple output.
NF	noise figure.
PA	power amplifier.
PDoA	phase difference of arrival.
PoA	phase of arrival.
Q	Quadrature.
RCS	radar cross section.
RF	radio frequency.
RFID	radio frequency identification.
RMS	root mean square.
RPRP	rapid prototyping reader platform.
RSSI	received signal strength indicator.
SAR	synthetic aperture radar.
SD-PDoA	spatial domain phase difference of arrival.
SDR	software defined radio.
SIMO	single input multiple output.
SNR	signal to noise ratio.
TD-PDoA	time domain phase difference of arrival.
UHF	ultra high frequency.
USRP	universal software peripheral.

VNA vector network analyzer.

Latin Symbols

C	Circumference.
G_{RX}	Reader RX antenna gain.
G_{TX}	Reader TX antenna gain.
G_{Tag}	Tag antenna gain.
G_{bw}	Backward link channel gain.
G_{fw}	Forward link channel gain.
I_0	Antenna short circuit current.
I_{Ant}	Antenna driving current.
L_{bw}	Backward link path loss.
L_{fw}	Forward link path loss.
L	Baseband leakage signal.
P_{RX}	Received tag signal power.
$P_{\mathrm{TX,max}}$	Maximum reader transmit power.
P_{TX}	Reader transmit power.
P_{Tag}	Available power at tag antenna terminals.
P_{act}	Actual positions.
P_{bw}	Backward link outage probability.
P_{chip}	Available chip power.
P_{fw}	Forward link outage probability.
P_{track}	Tracked positions.
R_{Ant}	Antenna resistance.
R_{b}	Estimated bistatic range.
R	Estimated monostatic range.
$S^{(A)}$	Baseband signal in tag absorbing mode.
$S^{(B)}$	Baseband signal in tag reflecting mode.
S_{Abs}	Absorbing mode reflection coefficient.

S_{Ref}	Reflecting mode reflection coefficient.
S_{ij}	Transmission coefficient.
T_0	Operating temperature.
T_{RX}	Reader receiver sensitivity.
T_{bw}	Backward link threshold.
T_{chip}	Chip sensitivity.
$T_{\mathrm{fw,semi}}$	Forward link threshold of semi passive chip.
T_{fw}	Forward link threshold.
V_{L}	Voltage at receiver input.
V_{abs}	Voltage at receiver input in absorbing mode.
V_{oc}	Open circuit voltage.
V_{ref}	Voltage at receiver input in reflecting mode.
V	Voltage.
Z_{Abs}	Chip absorbing impedance.
Z_{Ant}	Antenna impedance.
Z_{L}	Receiver input impedance.
Z_{Ref}	Chip reflecting impedance.
$\Delta\vec{E}_{\mathrm{Scat}}$	Differential scattered electric field.
$\vec{E}_{\mathrm{Ant}}$	Transmitted electric field.
$\vec{E}_{\mathrm{Inc}}$	Incident electric field.
$\vec{E}_{\mathrm{Scat}}$	Scattered electric field.
$\vec{\ell}_{\mathrm{e}}$	Vector effective antenna length.
c	Speed of light.
d_{RX1}	Distance between RX1 and tag.
d_{RX2}	Distance between RX2 and tag.
$d_{\mathrm{TX,RX1}}$	Horizontal distance between TX and RX1 antennas.
$d_{\mathrm{TX,RX2}}$	Horizontal distance between TX and RX2 antennas.
d_{TX}	Distance between TX and tag.
d	Horizontal distance between RX1 and RX2.
f	Frequency.
$h(t)$	Baseband tag signal vs. time.

h_{RF}	RF tag signal.
h_{bw}	Backward link transfer function.
h_{fw}	Forward link transfer function.
$h_{\mathrm{recon}}(t)$	Reconstructed baseband tag signal vs. time.
h	Baseband tag signal.
k	Bolzmann constant.
p_{bw}	Backward link polarization mismatch.
p_{fw}	Forward link polarization mismatch.
$r(t)$	Receiver baseband signal vs. time.
$r_{\mathrm{I}}(t)$	Receiver baseband signal vs. time, I component.
$r_{\mathrm{Q}}(t)$	Receiver baseband signal vs. time, Q component.
t	Time.
x	x coordinate.
y	y coordinate.

Greek Symbols

$\Delta\varphi$	Phase difference.
Δf	Frequency difference.
Θ	Direction of arrival.
α	Tag modulation constant.
β_{w}	Wavenumber.
β	Geometric angle.
η_0	Free space impedance.
η	Modulation efficiency.
λ	Wavelength.
ψ	Analog sensing state.
τ	Power transmission coefficient.
φ_{h}	Baseband tag signal phase.

Bibliography

[1] H. Stockman. "Communication by Means of Reflected Power." In: *Proceedings of the IRE* (1948).

[2] K. Finkenzeller. *RFID Handbook: Fundamentals and Applications in Contactless Smart Cards, Radio Frequency Identification and Near-Field Communication, third edition*. John Wiley & Sons, Ltd, 2010.

[3] D. M. Dobkin. *The RF in RFID: UHF RFID in Practice*. Newnes, 2012.

[4] J. Grosinger. "Backscatter Radio Frequency Systems and Devices for Novel Wireless Sensing Applications." PhD thesis. Vienna University of Technology, 2012.

[5] A. Boaventura et al. "Perfect Isolation: Dealing with Self-Jamming in Passive RFID Systems." In: *IEEE Microwave Magazine* (2016).

[6] P. V. Nikitin and K. V. S. Rao. "Antennas and Propagation in UHF RFID Systems." In: *Proc. IEEE International Conference on RFID*. 2008.

[7] J. D. Griffin and G. D. Durgin. "Complete Link Budgets for Backscatter-Radio and RFID Systems." In: *IEEE Antennas and Propagation Magazine* (2009).

[8] J. Grosinger. "Feasibility of Backscatter RFID Systems on the Human Body." In: *EURASIP Journal on Embedded Systems* (2013).

[9] A. F. Molisch. *Wireless Communications*. John Wiley & Sons, 2012.

[10] P. V. Nikitin, K. V. S. Rao, and R. D. Martinez. "Differential RCS of RFID Tag." In: *Electronics Letters* (2007).

[11] B. Rembold. "Optimum Modulation Efficiency and Sideband Backscatter Power Response of RFID-Tags." In: *Frequenz* (2009).

[12] C. Angerer. "Design and Exploration of Radio Frequency Identification Systems by Rapid Prototyping." PhD thesis. Vienna University of Technology, 2010.

[13] J.-P. Curty et al. *Design and Optimization of Passive UHF RFID Systems*. Springer Science & Business Media, 2006.

[14] B. S. Ciftler, A. Kadri, and I. Guvenc. "IoT Localization for Bistatic Passive UHF RFID Systems with 3-D Radiation Pattern." In: *IEEE Internet of Things Journal* (2017).

[15] J. Zhang et al. "BFVP: A Probabilistic UHF RFID Tag Localization Algorithm Using Bayesian Filter and a Variable Power RFID Model." In: *IEEE Transactions on Industrial Electronics* (2018).

[16] F. Martinelli. "A Robot Localization System Combining RSSI and Phase Shift in UHF-RFID Signals." In: *IEEE Transactions on Control Systems Technology* (2015).

[17] S. Park and H. Lee. "Self-Recognition of Vehicle Position Using UHF Passive RFID Tags." In: *IEEE Transactions on Industrial Electronics* (2013).

[18] M. Scherhaufl, M. Pichler, and A. Stelzer. "UHF RFID Localization Based on Evaluation of Backscattered Tag Signals." In: *IEEE Transactions on Instrumentation and Measurement* (2015).

[19] S. Shao and R. J. Burkholder. "Item-Level RFID Tag Location Sensing Utilizing Reader Antenna Spatial Diversity." In: *IEEE Sensors Journal* (2013).

[20] Y. Zhao et al. "Similarity Analysis-Based Indoor Localization Algorithm with Backscatter Information of Passive UHF RFID Tags." In: *IEEE Sensors Journal* (2017).

[21] A. Athalye et al. "Novel Semi-Passive RFID System for Indoor Localization." In: *IEEE Sensors Journal* (2013).

[22] E. DiGiampaolo and F. Martinelli. "A Passive UHF-RFID System for the Localization of an Indoor Autonomous Vehicle." In: *IEEE Transactions on Industrial Electronics* (2012).

[23] Z. Zhang et al. "Item-Level Indoor Localization with Passive UHF RFID Based on Tag Interaction Analysis." In: *IEEE Transactions on Industrial Electronics* (2014).

[24] H. Ma et al. “The Optimization for Hyperbolic Positioning of UHF Passive RFID Tags.” In: *IEEE Transactions on Automation Science and Engineering* (2017).

[25] S. Sarkka et al. “Phase-Based UHF RFID Tracking with Nonlinear Kalman Filtering and Smoothing.” In: *IEEE Sensors Journal* (2012).

[26] P. V. Nikitin et al. “Phase Based Spatial Identification of UHF RFID Tags.” In: *Proc. IEEE International Conference on RFID*. 2010.

[27] C. Angerer, R. Langwieser, and M. Rupp. “Direction of Arrival Estimation by Phased Arrays in RFID.” In: *Proc. EURASIP Workshop on RFID Technology*. 2010.

[28] V. Viikari, P. Pursula, and K. Jaakkola. “Ranging of UHF RFID Tag Using Stepped Frequency Read-Out.” In: *IEEE Sensors Journal* (2010).

[29] R. Miesen, F. Kirsch, and M. Vossiek. “UHF RFID Localization Based on Synthetic Apertures.” In: *IEEE Transactions on Automation Science and Engineering* (2013).

[30] A. Buffi, M. R. Pino, and P. Nepa. “Experimental Validation of a SAR-Based RFID Localization Technique Exploiting an Automated Handling System.” In: *IEEE Antennas and Wireless Propagation Letters* (2017).

[31] A. Buffi, P. Nepa, and F. Lombardini. “A Phase-Based Technique for Localization of UHF-RFID Tags Moving on a Conveyor Belt: Performance Analysis and Test-Case Measurements.” In: *IEEE Sensors Journal* (2015).

[32] R. Bhattacharyya, C. Floerkemeier, and S. Sarma. “Low-Cost, Ubiquitous RFID-Tag-Antenna-Based Sensing.” In: *Proceedings of the IEEE* (2010).

[33] J. Grosinger, L. Gortschacher, and W. Bosch. “Passive RFID Sensor Tag Concept and Prototype Exploiting a Full Control of Amplitude and Phase of the Tag Signal.” In: *IEEE Transactions on Microwave Theory and Techniques* (2016).

[34] C. Occhiuzzi, S. Caizzone, and G. Marrocco. “Passive UHF RFID Antennas for Sensing Applications: Principles, Methods, and Classifcations.” In: *IEEE Antennas and Propagation Magazine* (2013).

[35] A. A. Babar et al. “Passive UHF RFID Tag for Heat Sensing Applications.” In: *IEEE Transactions on Antennas and Propagation* (2012).

[36] F. Yang et al. “Reconfigurable Sensing Antenna: A Slotted Patch Design With Temperature Sensation.” In: *IEEE Antennas and Wireless Propagation Letters* (2012).

[37] K. Zannas et al. “On the Cooperative Exploitation of Antenna Sensitivity and Auto-Tuning Capability of UHF RFID Chip. Application to Temperature Sensing.” In: *Proc. IEEE International Microwave Symposium*. 2018.

[38] M. C. Caccami, S. Manzari, and G. Marrocco. “Phase-Oriented Sensing by Means of Loaded UHF RFID Tags.” In: *IEEE Transactions on Antennas and Propagation* (2015).

[39] D. Shuaib et al. “The Possibilities of Embroidered Passive UHF RFID Textile Tags as Wearable Moisture Sensors.” In: *Proc. IEEE 5th International Conference on Serious Games and Applications for Health (SeGAH)*. 2017.

[40] R. Goncalves et al. “RFID-Based Wireless Passive Sensors Utilizing Cork Materials.” In: *IEEE Sensors Journal* (2015).

[41] S. Manzari and G. Marrocco. “Modeling and Applications of a Chemical-Loaded UHF RFID Sensing Antenna With Tuning Capability.” In: *IEEE Transactions on Antennas and Propagation* (2014).

[42] C. Paggi, C. Occhiuzzi, and G. Marrocco. “Sub-Millimeter Displacement Sensing by Passive UHF RFID Antennas.” In: *IEEE Transactions on Antennas and Propagation* (2014).

[43] R. Krigslund et al. “A Novel Technology for Motion Capture Using Passive UHF RFID Tags.” In: *IEEE Transactions on Bio-Medical Engineering* (2013).

[44] R. Krigslund, P. Popovski, and G. F. Pedersen. “Orientation Sensing Using Multiple Passive RFID Tags.” In: *IEEE Antennas and Wireless Propagation Letters* (2012).

[45] X. Chen, L. Ukkonen, and T. Bjorninen. “Passive E-Textile UHF RFID-Based Wireless Strain Sensors With Integrated References.” In: *IEEE Sensors Journal* (2016).

[46] A. A. Kutty et al. “A Novel Carbon Nanotube Loaded Passive UHF RFID Sensor Tag with Built-in Reference for Wireless Gas Sensing.” In: *Proc. IEEE MTT-S International Microwave Symposium (IMS)*. 2016.

[47] C. Occhiuzzi et al. “RFID Passive Gas Sensor Integrating Carbon Nanotubes.” In: *IEEE Transactions on Microwave Theory and Techniques* (2011).

[48] J. Zhang and G. Y. Tian. “UHF RFID Tag Antenna-Based Sensing for Corrosion Detection & Characterization Using Principal Component Analysis.” In: *IEEE Transactions on Antennas and Propagation* (2016).

[49] S. Kim et al. “Low-Cost Inkjet-Printed Fully Passive RFID Tags for Calibration-Free Capacitive/Haptic Sensor Applications.” In: *IEEE Sensors Journal* (2015).

[50] S. D. Nguyen et al. “Approach for Quality Detection of Food by RFID-Based Wireless Sensor Tag.” In: *Electronics Letters* (2013).

[51] G. Marrocco. “RFID Grids: Part I—Electromagnetic Theory.” In: *IEEE Transactions on Antennas and Propagation* (2011).

[52] S. Caizzone, E. D. Giampaolo, and G. Marrocco. “Setup-Independent Phase-Based Sensing by UHF RFID.” In: *IEEE Antennas and Wireless Propagation Letters* (2017).

[53] S. Capdevila et al. “Multi-Loaded Modulated Scatterer Technique for Sensing Applications.” In: *IEEE Transactions on Instrumentation and Measurement* (2013).

[54] GS1. *EPC Radio-Frequency Identity Protocols Generation-2 UHF RFID*. Nov. 2013. URL: `https://www.gs1.org/sites/default/files/docs/epc/uhfc1g2_2_0_0_standard_20131101.pdf` (visited on 06/08/2018).

[55] H. N. Khan et al. “Measurement Based Indoor SIMO RFID Simulator for Tag Positioning.” In: *Proc. International EURASIP Workshop on RFID Technology (EURFID)*. 2015.

[56] H. N. Khan et al. “Statistical Analysis of the Power Delay Profile of a SIMO UHF Backscatter RFID Channel in an Engine Test Bed.” In: *Proc. Loughborough Antennas Propagation Conference (LAPC)*. 2016.

[57] Motorola. *RFID Antenna Family*. Apr. 2015. URL: `http://www.barcodesinc.com/pdf/Motorola/an-series.pdf` (visited on 06/08/2018).

[58] Zebra. *FX9500 Fixed RFID Reader*. 2017. URL: https://www.zebra.com/content/dam/zebra_new_ia/en-us/solutions-verticals/product/RFID/Reader/FX9500%20Fixed%20RFID%20Reader/spec-sheets/fx9500-spec-sheet-en-us.pdf (visited on 06/08/2018).

[59] NXP Semiconductors. *SL3S1203_1213*. Mar. 2014. URL: https://www.nxp.com/docs/en/data-sheet/SL3S1203_1213.pdf (visited on 06/08/2018).

[60] Intelleflex. *The Intelleflex XC3 Technology Platform*. 2010. URL: https://connectedworld.com/wp-content/uploads/2014/07/Whitepaper_Intelleflex_TheIntelleflexXC3.pdf (visited on 06/12/2018).

[61] Mini Circuits. *ZHL-1000-3W+*. URL: https://ww2.minicircuits.com/pdfs/ZHL-1000-3W+.pdf (visited on 09/11/2018).

[62] Sokymat. *InLine UHF Tag Ucode EPC Gen2 869 MHz*. Mar. 2016. URL: http://www.rfid-webshop.com/shop/download/tags/UHF868_915MHz/Sokymat/I&L/UHF/TAGnology_InLine%20UHF%20Tag%20EPC%20Gen2%20869%20MHz%20%20-%20V1%20-%2013426.pdf (visited on 08/27/2018).

[63] R. B. Green. "The General Theory of Antenna Scattering." PhD thesis. The Ohio State University, 1963.

[64] R. C. Hansen. "Relationships Between Antennas as Scatterers and as Radiators." In: *Proceedings of the IEEE* (1989).

[65] C. A. Balanis. *Antenna Theory: Analysis and Design*. John Wiley & Sons, 2016.

[66] L. Görtschacher, W. Bösch, and J. Grosinger. "UHF RFID Sensor Tag Antenna Concept for Stable and Distance Independent Remote Monitoring." In: *Proc. IEEE MTT-S International Microwave Biomedical conference*. 2018.

[67] S. Capdevila et al. "Passive RFID Based Sensing." In: *Proc. IEEE International Conference on RFID-Technologies and Applications*. 2011.

[68] Motorola. *SL3S1204 UCODE 7*. Mar. 2017. URL: https://www.nxp.com/docs/en/data-sheet/SL3S1204.pdf (visited on 08/08/2018).

[69] P. Nikitin and K. Rao. "Theory and Measurement of Backscattering from RFID Tags." In: *IEEE Antennas and Propagation Magazine* (2006).